Mathematical Modeling and Analysis of Solid Oxide Fuel Cells and a Dye Sensitized Solar Cell

A Thesis

Submitted to the Faculty

of

Drexel University

By

Mona Bavarian

In Partial Fulfillment of the

Requirements for the

Degree

Of

Doctor of Philosophy

June 2012

DEDICATION

To my parents, Siamak and loved ones

ACKNOWLEDGEMENTS

First, I would like to thank someone special, whom without his help this project was not in existence, my truly real mentor who taught me not only how to do a Ph.D. but how to be a better person for the society. Thank you Professor Soroush for all the good you implanted in me.

I am grateful to my doctoral committee members, Professors Jason Baxter, Jay B. Benziger, Yannis Kevrekidis, and Kenneth K.S. Lau for their support, guidance, time and always raising very interesting questions! Their valuable feedbacks were very beneficial from the start of this project till now.

I had a great opportunity to collaborate with Professor Kenneth K.S. Lau and Siamak Nejati in the DSSC project. I am very thankful to them for sharing their data with me as well as their interesting and constructive discussions.

I want to thank my current lab mates, Patrick Corcoran and Taha Mohseni for always being nice to me and helping me in different aspects of life. I also want to thank the past members of process systems engineering group, Dr. Sriraj Srinvasan, Morgan Almanza and Jorge Garriga. It was pleasant to hear Gorge discussing the poincare' conjecture and differential geometry on a daily basis as if he sees himself tied to it.

I would also like to thank my family and friends, who are always supportive and caring, Amin, An, Babak, Behnam, Behzad , Bijan, Dariush, Donia, Elnaz, Golshan, Kurosh, Farzin, Golnaz, Lawrence, Mahnaz, Marzie, Mojgan, Monir, Mohsen, Nafiseh, Neda, Payam, Sabrina, Solmaz, Shahla and Sylvie. I also want to thank my dearest grandmothers, Hamideh and Nosrat for all their prayers and support.

I like to thank my sisters, Sara and Maryam and my brother Mohammad for their love, advice and kindness and making me laugh all the time.

Special thanks to my dear Siamak who is always encouraging. Whenever we discuss he was always open to hear my opinion and critically discuss the problems. I am sure it was always a fruitful discussion as I could tell that from his Duchenne smile. I am very thankful and happy for all his understanding, continued love, and support.

Last but not the least; I would love to thank my parents. They have been always a great source of love, kindness and encouragement. During these years far from them, talking with them was always very calming and encouraging.

TABLE OF CONTENTS

LIST OF TABLES……………………………………………………………**x**

LIST OF FIGURES…………………………………………………………..…**xi**

ABSTRACT…………………………………………………………………..**xvii**

1 CHAPTER 1: SOLID OXIDE FUEL CELLS BACKGROUND AND LITERATURE REVIEW 1

1.1 Introduction 1

1.2 Mathematical Modeling 2

1.2.1 General Features 5

1.2.2 Phenomena/Processes to Be Accounted for 6

1.2.3 Lumped-Parameter Mathematical Modeling 8

1.2.4 Spatially-Distributed Mathematical Modeling 10

1.3 Steady State Behavior 27

1.3.1 Steady State Multiplicity 28

1.4 Dynamic Behavior 34

1.4.1 Multi-Time-Scale Nature 35

1.5 Concluding Remarks 38

2 CHAPTER 2: STEADY STATE MULTIPLICITY AND DYNAMIC BEHAVIOR IN AN OXYGEN-ION CONDUCTING SOFC 40

2.1 Introduction 40

2.2 Review: Motivation 42

2.3 Mathematical Modeling 48

2.3.1 Electrochemical Modeling 51

2.3.2 Model Equations for Subsystem 1 53
2.3.3 Model Equations for Subsystem 2 54
2.3.4 Model Equations for Subsystem 3 55
2.3.5 Model Equations for Subsystem 4 56
2.3.6 Model Equations for Subsystem 5.. 57
2.4 Numerical Method 58
2.5 Steady State Analysis 59
2.5.1 Constant Ohmic Load Operation 60
2.5.2 Potentiostatic Operation 71
2.5.3 Galvanostatic Operation 73
2.6 Dynamic Behavior 74
2.7 Conclusions 78
3 CHAPTER 3: MATHEMATICAL MODELING AND STEADY-STATE ANALYSIS OF A PROTON- CONDUCTING SOLID OXIDE FUEL CELL ..80
3.1 Introduction 80
3.2 Model Development 82
3.2.1 Electrochemical Model 84
3.2.2 Energy Conservation 86
3.2.3 Mass Conservation 87
3.3 Model Validation 91
3.4 Steady-state Multiplicity 92
3.4.1 Electrolyte-Supported Cell 95
3.4.1.1 Constant Ohmic Load Operation 95
3.4.1.2 Potentiostatic Operation 100

3.4.1.3 Galvanostatic Operation……………………………………..102

3.4.2 Anode-Supported Cell 103

3.5 Concluding Remarks 105

4 CHAPTER 4: MODELING AND BIFURCATION ANALYSIS OF A CO-IONIC-CONDUCTING SOLID OXIDE FUEL CELL 108

4.1 Introduction..108

4.2 Model Development 112

4.2.1 Electrochemical Submodel...113

4.2.2 Heat Transfer Sub-model 118

4.2.3 Mass Transfer Sub-model 119

4.3 Simulation Method 123

4.4 Parameter Estimation and Model Validation...125

4.5 Steady State Behavior..126

4.6 Concluding Remarks 134

5 CHAPTER 5: DYE SENSITIZED SOLAR CELL BACKGROUND AND LITERATURE REVIEW...137

5.1 Introduction..137

5.2 DSSC Working Principle...137

5.3 Theoretical and Experimental Considerations in a DSSC.......................141

5.3.1 Light to Electron Conversion 141

5.3.2 Electron Transport in the Semiconducting Oxide 142

5.3.3 Electrolyte 143

5.4 Characterization Techniques..144

5.4.1 IV, IPCE and APCE...145

5.4.2 Frequency Resolved Methods 146
5.4.2.1 Electrochemical Impedance Spectroscopy……………………..146
5.4.2.2 Light Modulation Methods……………………………………147
5.5 Conclusions 147

6 CHAPTER 6: MACROSCOPIC MODELING AND ANALYSIS OF DYE SENSITIZED SOLAR CELLS 149

6.1 Introduction 149
6.2 Literature Review on modeling of DSSCs 150
6.3 Model Development 153
6.3.1 Electrons Recombination 154
6.3.2 Electrons Generation..157
6.3.3 Ionic Species Generation and Consumption Rates..........................157
6.3.4 Electrons and Ionic Species Transport..158
6.3.5 Electrical Characteristics and the Energetics of the DSSC..............158
6.4 Steady State model 161
6.4.1 Boundary Conditions 164
6.4.2 IV Curve Generation..165
6.4.3 Simulation Results: Model I and Model II.....................................165
6.4.4 Champion DSSC: 11.1 % Conversion...169
6.4.4.1 Parameter Estimation…………………………………………...170
6.4.4.2 Scenario I……………………………………………………….170
6.4.4.3 Scenario II………………………………………………………171
6.4.4.4 Scenario III……………………………………………………..171

6.4.4.5 Scenario IV……………………………………………………..172

6.5 Sensitivity Analysis 173

6.6 Effect of Recombination Rate Constant and Conduction Band Movement ………………………………………………………………………...173

6.7 Quasi-solid State Electrolyte DSSC 175

6.7.1 Surface Modification and Band Edge Movement 177

6.8 Transient Model 178

6.9 Concluding Remarks 181

7 CHAPTER 7: CONCLUSIONS AND RECOMMENDED FUTURE WORK 182

7.1 Summary and Conclusions 182

7.2 Recommended Future Work 184

LIST OF REFERENCES……………………………………………………186

VITA…………………………………………………………………………..204

LIST OF TABLES

Table 1-1 Studies on SOFC Modeling. 3

Table 1-2. Studies on Steady Sate Multiplicity in PEMFC and SOFCs. 27

Table 1-3. Time Scales of a Planar SOFC.[69] 35

Table 2-1. Parameter Values of the Detailed Model. 49

Table 2-2. Specific heat capacities of the gas components[78]. 51

Table 3-1. Parameter values in Eq. 3.21. 89

Table 3-2. Parameter values of the model. 90

Table 4-1. Fuel cell model parameter values...121

Table 6-1. Input parameters of the model[162]. 166

Table 6-2. Estimated parameters employing a second order electron recombination kinetic EQ. 6.7. 170

Table 6-3. Estimated parameters employing a second order electron recombination kinetic EQ. 6.14. 171

Table 6-4. Estimated parameters employing a first order electron recombination kinetic EQ. 6.14. 172

Table 6-5. Estimated parameters employing a first order electron recombination kinetic EQ. 6.15. 172

Table 6-6. Model parameters sensitivity analysis. 173

Table 6-7. Estimated parameters of polymer incorporated DSSC based on a first order electron recombination kinetic EQ. 6.15. 176

LIST OF FIGURES

Figure 2.1. Steady-state heat generation (Q_P) and heat removal (Q_R) versus solid temperature at an external load resistance of 0.0065 Ω, based on the simple model in[56]. 45

Figure 2.2. Bifurcation diagram (solid temperature versus load resistance), based on the simple model in[56]........ 45

Figure 2.3. Bifurcation analysis (solid temperature versus cell voltage), based on the simple model in[56]. 46

Figure 2.4. Planar SOFC divided into five subsystems. 49

Figure 2.5. Steady-state heat generation (Q_P) and heat removal (Q_R) versus solid temperature at an external load resistance of 0.0065 Ω, based on the more detailed model. 61

Figure 2.6. Steady state behavior under inlet gas channel temperatures of 980 K, based on the more detailed model: (a) Steady-state heat generation (Q_P) and heat removal (Q_R) versus solid temperature at an external load resistance of 0.0112 Ω; (b) steady state analysis of the detailed model (solid temperature versus load resistance). 62

Figure 2.7. Steady state behavior under inlet gas channel temperatures of 950 K, based on the more detailed model: (a) Steady-state heat generation (Q_P) and heat removal (Q_R) versus solid temperature at an external load resistance of 0.0112 Ω; (b) Bifurcation analysis of the detailed model (solid temperature versus load resistance). 64

Figure 2.8. Variations in cathode and anode gas inlet temperature, based on the more detailed model: (a) cathode gas inlet temperature versus solid temperature; (b) anode gas inlet temperature versus solid temperature. 65

Figure 2.9. Variations in mole fraction of reactants and product species at the triple phase boundary zone, based on the more detailed model. 67

Figure 2.10. Multiplicity region for different heat convection coefficients in the constant ohmic load operation, based on the more detailed model. 67

Figure 2.11. Solid temperature versus load resistance as inlet gas temperatures vary, based on the more detailed model. 68

Figure 2.12. Solid temperature versus load resistance for different fuel and air velocities, based on the more detailed model (A: $v_{\text{air}}^{\text{cat}}$ =157.96 m.s^{-1}, $v_{\text{fuel}}^{\text{an}}$ = 5.76 m.s^{-1} B: $v_{\text{air}}^{\text{cat}}$ =78.98 m.s^{-1}, $v_{\text{fuel}}^{\text{an}}$ = 2.88 m.s^{-1} ;C: $v_{\text{air}}^{\text{cat}}$ =39.49 m.s^{-1}, $v_{\text{fuel}}^{\text{an}}$ = 1.44 m.s^{-1}).69

Figure 2.13. Solid temperature versus load resistance as inlet fuel flow rate varies, based on the more detailed model...70

Figure 2.14. Solid temperature versus load resistance as inlet air flow rate varies, based on the more detailed model...70

Figure 2.15. Bifurcation analysis potentiostatic control (solid temperature versus cell voltage), based on the more detailed model...72

Figure 2.16. Multiplicity region for different heat convection coefficient values in the potentiostatic mode, based on the more detailed model. 73

Figure 2.17. Solid temperature versus current under galvanostic operation mode, based on the more detailed model...74

Figure 2.18. Dynamic response of the SOFC to a step change in the load resistance from 0.014 to 0.01 Ω, based on the more detailed model. 76

Figure 2.19. Dynamic response of the SOFC to a step change in the load resistance from 10 to 5 Ω, based on the more detailed model. 77

Figure 2.20. Variations in the ohmic overpotential in response to a step change in the ohmic load resistance, a) 0.014 to 0.01 Ω, and b) 10 to 5 Ω. 77

Figure 3.1. Planar SOFC divided into five subsystems. 84

Figure 3.2. The IV curve at 1073 K: experimental data [91] and the model predictions. 92

Figure 3.3. Steady state behavior under inlet gas channel temperatures of 750 K: Steady-state heat generation (Q_P) and heat removal ($Q_{R,25}$, $Q_{R,75}$) versus the solid temperature at an external load resistance of 0.47 Ω, at two different values of the heat convection coefficient, (a) 25 and (b) 75 W/m^{2}K 93

Figure 3.4. Steady-state heat generation (Q_P) and heat removal (Q_R) versus the solid temperature at an external load resistance of 5 Ω and a heat convection coefficient of 25 W/m^{2}K. 94

Figure 3.5. Bifurcation diagrams under constant ohmic load: species mole fractions ($\boldsymbol{y_{O_2}}$, $\boldsymbol{y_{H_2}}$, and $\boldsymbol{y_{H_2O}}$) in the gas channels, the outlet gas temperatures (Tan, Tcath) and the solid temperature (Ts) versus load resistance. 96

Figure 3.6. Bifurcation curve of the solid temperature versus the load power density. 97

Figure 3.7. Multiplicity region for different heat convection coefficients in the constant ohmic load operation. 98

Figure 3.8. Solid temperature versus load resistance as the inlet gas temperatures vary. 99

Figure 3.9. Solid temperature versus load resistance as the inlet fuel and air flow rates vary. 99

Figure 3.10. Bifurcation analysis under potentiostatic mode: species mole fractions (y_{O_2}, y_{H_2}, and y_{H_2O}) in the gas channels, the outlet gas temperatures (T_{an}, T_{cath}) and the solid temperature (T_s) versus cell voltage. 100

Figure 3.11. Multiplicity region for different heat convection coefficient values in the potentiostatic mode..........101

Figure 3.12. Solid temperature versus the inlet gas temperatures at different values of cell voltage. 102

Figure 3.13. Species mole fractions (y_{O_2}, y_{H_2}, and y_{H_2O}) in gas channels, the outlet gas temperatures (T_{an}, T_{cath}) and the solid temperature (T_s) versus cell current under galvanostatic operation mode..........104

Figure 3.14. Solid temperature versus load resistance. (a) electrolyte-supported cell, (b) anode-supported cell. 105

Figure 4.1. Component conductivities in $BaCe_{1-x}Sm_xO_{3-\alpha}$[106]..........110

Figure 4.2. Planar SOFC divided into five subsystems. 112

Figure 4.3. Triple phase boundary in a co-ionic conducting SOFC. 114

Figure 4.4. Equivalent circuit of the fuel cell. 115

Figure 4.5. The I-V curve of the fuel cell at 1273 K (circles = experimental data[106], solid line = model prediction). 126

Figure 4.6. Steady-state heat removal and heat generation under two different external load resistances, (a) 2.6 Ω and (b) 5 Ω. 127

Figure 4.7. Bifurcation diagram (fixed ohmic load mode of operation). 128

Figure 4.8. Bifurcation analysis under fixed ohmic load: species mole fractions (y_{O_2}, y_{H_2} , $y_{H_2O,cath}$ and $y_{H_2O,an}$) in the gas channels. 129

Figure 4.9. The bifurcation manifold of the cusp catastrophe: T_S versus R_{load} and the inlet gas temperatures 129

Figure 4.10. Multiplicity region in the fixed ohmic load mode. 130

Figure 4.11. Solid temperature versus load power density. 131

Figure 4.12. Solid temperature versus the load resistance and equal inlet fuel and air flow rates. 131

Figure 4.13. Bifurcation diagrams: solid temperature versus equal inlet fuel and air flow rates under four different operation modes of fixed ohmic load, galvanostatic, potentiostatic and fixed load power density. 132

Figure 4.14. Bifurcation diagram: solid temperature versus cell voltage. 133

Figure 4.15. Solid temperature versus cell current. 133

Figure 5.1. Schematic of a DSSC. 138

Figure 5.2. Diagram of the operation mechanism and different processes time constants[126]. 140

Figure 6.1. Equivalent circuit of the DSSC.[162] 161

Figure 6.2. Schematic of a DSSC. 162

Figure 6.3. Model I simulation results: distribution of electron current density, electron density, electric field, deviation of iodide species from equilibrium,

deviation of triiodide species from equilibrium, and deviation of lithium ions from equilibrium under short circuit (SC) and open circuit (OC) conditions.............167

Figure 6.4. Model II simulation results: distribution of electron density, electron current density, triiodide and iodide deviations from equilibrium. 168

Figure 6.5. Effect of changes in recombination rate constant on the cell IV curve. The black curve shows the IV curve found by parameter estimation (basis). The colored curves show the IV curve while the recombination rate constants increase compared to the basis. 174

Figure 6.6. Effect of changes in the conduction band position on the cell IV curve. The black curve shows the IV curve found by parameter estimation (basis). The colored curves show the IV curve while the conduction band shifts to lower values of negative potential. 175

Figure 6.7. IV curve of the cell a) in the case of using liquid electrolyte (blue) b) in the case of the cell fabricated with polymer electrolyte (black). 177

Figure 6.8. Distribution of electron density, iodide and triiodide species from dark equilibrium to open circuit condition. 179

Figure 6.9. Distribution of electron density, iodide and triiodide species from dark equilibrium to short circuit condition. 180

ABSTARCT

Mathematical Modeling and Analysis of Solid Oxide Fuel Cells and a Dye Sensitized Solar Cell

Mona Bavarian
Advisor: Masoud Soroush, Ph.D.

As the fuel cell and solar cell technologies have advanced significantly in the past decade, the need for a better understanding of the steady-state and dynamic behaviors of the cells has increased. Since many processes occurring in the cells are highly nonlinear, systematic analyses are required to unveil the nonlinear effects of operating conditions on the cell performance. The focus of this work is on Solid Oxide Fuel Cells (SOFCs) and dye sensitized solar cells (DSSCs), both of which are of high importance in the renewable energy technology arena. DSSCs currently have achieved energy conversion efficiencies of 12%. The design and operation of the cells can greatly benefit from a better fundamental quantitative understanding of the physical and electrochemical processes involved in the cells.

In this work, the presence of multiple steady states for three different types of SOFCs, oxygen-ion (conventional)-, proton-, and co-ionic (oxygen ion and proton)-conducting SOFCs, are investigated. An objective of this study is to investigate the effect of process parameter values on the steady-state multiplicity and the location of steady state(s). The existence of multiple steady states in the system is investigated in terms of the air and fuel inlet temperatures, the convection heat transfer coefficient, and the external load resistance. The range of operating conditions for which steady-state multiplicity exists is determined.

A macroscopic first-principles mathematical model of a DSSC is developed by accounting for four different recombination kinetic laws. The equations of continuity and transport for all the species in the cell including electrons and redox couple are considered. The model is used to estimate the key parameters in the DSSC operation including recombination rate constant, effective electron diffusion coefficient, the conduction band energy, and the exchange current density. The presence of electric field and the effect of migration on transport are theoretically investigated. In the case of quasi solid state electrolyte DSSC incorporating polymer electrolyte, it can be hypothesized that the conduction band edge movement arouses due to the possible surface changes which consequently increases the photovoltage of the cell.

1 Chapter 1: Solid Oxide Fuel Cells Background and Literature Review

1.1 Introduction

The need for benign, pollution-free, energy-efficient, quiet electricity generators has attracted many researchers to fuel cell power systems. These energy devices have the potential to be used in stationary and mobile applications[1]and replace combustion engines in vehicles[2]. A fuel cell is an energy conversion device that produces electricity directly from the chemical energy of a fuel. Fuel cells are classified on the basis of the electrolyte used in the system. The two most common and promising fuel cells are SOFCS and the polyelectrolyte membrane fuel cell (PEMFC). The focus of this study is on SOFCs. The primary components of a fuel cell are an ion conducting electrolyte, an anode, and a cathode.

Materials for a typical SOFC are generally oxide-ion conducting yttria-stabilized zirconia (YSZ) for the electrolyte, strontium-doped lanthanum manganite (LSM) for the cathode, nickel/YSZ for the anode, and doped lanthanum chromite or high-temperature metals for the interconnect[1, 3-4]. A SOFC usually operates at a temperature range of 800 to 1200°C. At these high operating temperatures, oxygen ions (with a negative charge) migrate through the electrolyte. When a fuel gas containing hydrogen flows over the anode, negatively charged oxygen ions move across the electrolyte to oxidize the fuel. The oxygen is supplied, usually from air, at the cathode. Electrons generated at the anode move through an external load to the cathode, completing the circuit and supplying electric power. These fuel cells have a generating efficiency up to about 60 percent. Their most common application is in large, stationary power plants. Their high operation temperatures allows for "co-generation"; that is, using waste heat to generate steam for a variety of applications such as space heating, industrial processing, and steam turbines to make more electricity.

The history of SOFC goes back to 1930s, when Swiss scientist Baur and his colleague Preis used zirconia stabilized with 15 wt% yttria as an electrolyte for a tubular fuel cell[4]. SOFC has an older history than PEMFC, which emerged about 30 years after the invention of SOFC. Since that time, a great number of experimental and modeling studies have been carried out to explore the performance, problems and efficiency of fuel cells, with the ultimate goal of extensive commercialization of these energy devices.

1.2 Mathematical Modeling

Mathematical modeling is an indispensible tool for studying static and dynamic behavior of fuel cells, designing the cells, evaluating control strategies and designing experiments; it helps reduce the number of experimental tests required to study the cells systematically. Simulation studies can determine the effects of various operating conditions, different stack design, cell temperature distribution, thermal stresses and so. Having mentioned them, however, simulation results should be validated by experimental results from laboratory tests in order to ensure their credibility.

In a fuel cell system many processes including momentum, heat, and mass transport along with electrochemical reactions occur. The physics of these processes should be analyzed carefully to describe them in the form of mathematical equations.

The resulting dynamic fuel cell mathematical models are in the form of large sets of differential and algebraic equations that are highly nonlinear, complex and stiff. One of the challenges in fuel cell modeling is the use of reliable numerical integration methods to solve these governing stiff equations. In the next section, we will discuss the numerical methods which can be used for these problems. Lists of papers on SOFC are given in Table 1-1.

Table 1-1 Studies on SOFC Modeling.

Macro/Micro Dimensions	Design	Steady states/transient	Accounted for	Reference
0D	-	transient	Mass balance and ohmic losses	5
0D	Tubular	Transient	Electrochemical, and thermal transport phenomena	6
0D	-	Transient	Temperature and chemical species dynamics and voltage losses due to ohmic, activation and concentration polarization	7
0D		Transient	Electrochemical processes, heat transfer and mass balances	8
0D	Tubular	Transient	mass balance and electrochemical processes	9
0D	Tubular	Transient	Diffusion processes, heat, mass and momentum transfer, electrochemical processes, anode and cathode activation polarizations	10
1D	Tubular	Steady states/Transient	Heat transfer, species transport, and electrochemical processes	3
2D	Monolithic	Steady state	Mass, energy and electron balance, electrochemical processes	11
2D	Monolithic	Steady state	Heat and mass transfer and electrochemical processes	12
1D	Tubular	Steady state	Mass balance, heat transfer, electrochemical processes and reforming and shift reactions	13
3D	Planar	Transient	Mass balance, heat transfer, internal methane steam reforming, and different flow manifolding	14
1D	Planar	Steady state	Momentum transfer	15
3D	Tubular	Steady state	Electrochemical and thermal	16

			processes, mass and energy balances and radiation heat transfer	
3D	Planar/Tubular	Steady state	Mass and heat transfer, charge conservation and electrochemical processes	[17]
2D	Planar	Steady state	Mass balance, heat transfer, and electrochemical processes	[18]
2D	Planar	Steady state	Momentum transfer	[19]
3D	Planar	Steady state	Mass and momentum transfer and concentration polarization	[20]
1D	Planar	Steady state	Electrochemical processes, mass transfer, internal steam reforming and shift reactions	[21]
2D	Planar	Steady state	Mass, charge and heat balances and electrochemical processes	[22]
3D	Planar	Steady state	Mass, energy, electrical charge balances and internal reforming and water shift reactions	[23]
1D	Tubular	Steady state	Mass and energy balance, Internal reforming and shift reactions and electrochemical processes	[24]
3D	Planar	Steady state	Mass, heat and momentum transfer and electrochemical processes	[25]
1D/0D	Tubular	Transient	Heat transfer, mass balance and electrochemical processes	[26]
2D	Planar	Steady state	Heat, mass and momentum transfer and electrochemical processes	[27]
1D	Tubular	Steady state/Transient	Heat and mass transfer, electrochemical processes and equivalent circuit model	[28]
3D/1D	Planar	Steady states/Transient	Electrochemical processes and mass and energy balances	[29]
2D	Tubular	Steady state	Momentum, heat and mass transfer, internal reforming and shift reactions, electrochemical processes	[30]
2D	Planar	Steady state	Mass transport, energy balance, electrochemical processes and reforming and shift reactions	[31]
1D	Tubular	Steady state	Heat and momentum transfer, electrochemical processes and reforming and shift reactions	[32]
1D	Planar	Steady state/Transient	Mass transfer, energy balances and electrochemical processes	[33-34]
2D	Tubular	Steady state	Mass, momentum and heat transfer and electrochemical processes	[35]
1D	Tubular	Transient	Mass transfer, equivalent circuit model and electrochemical processes	[36]
1D	Planar	Steady states/Transient	Mass, energy and momentum balances, and electrochemical kinetics	[37]

2D	Tubular	Transient	Electrochemical reactions , mass and energy balances	38
2D	Tubular	Steady states	Momentum, mass and charge transport and electrochemical processes	39
1D	Tubular	Transient	Heat, mass and momentum transfer and internal reforming/shift reactions	40
1D	Tubular	Steady state/Transient	Electrochemical processes and voltage losses	41
1D	Planar	Transient	All transport and polarization phenomena	42
1D	Tubular	Steady state/Transient	Electrochemical processes, voltage losses, and heat transfer by conduction, convection and radiation	43
1D	Circular-planar	Steady state	Electrochemical, thermal, and mass balances	44
2D	Planar	Steady state/Transient	Electrochemical model, mass and heat transfer	45
1D	Planar/Tubular	Steady state	Mass and charge transfer	46
1D	Planar	Steady state	Electrochemical processes along with voltage losses caused by ohmic and activation overpotential, mass transport in the porous electrode media	47
1D	Tubular	Steady state/Transient	Diffusion, inherent impedance, heat transfer and internal reforming/shifting reaction	48
2D	Planar	Steady state	Transport phenomena of gas species with electrochemical processes	49
3D	Tubular	Steady state	Fluid flow and thermal transport including radiation heat transfer	50
2D	Tubular	Steady state/Transient	Mass transfer and electrochemical processes	51

1.2.1 General Features

The fuel cell system can be modeled considering time-dependent (temporal) effects and spatial changes. With respect to spatial changes, the problem can be 0-D (lumped model), 1-D, 2-D, or 3-D, depending on the number of spatial independent variables of the resulting model (differential equations). Throughout this paper, a model with j spatial independent variables will be referred to as a j-D model, where j=0, 1, 2, 3. With respect to temporal changes, the system can be studied at steady-state or transient conditions. In fact, the objective of the study leads the model developer to make a set of appropriate assumptions and arrive at a simple model. The general approach in modeling starts by dividing the system into subsystems or control volumes. For each control volume, appropriate conservation equations such as mass, charge, momentum and energy, are written. The next step is to write down constitutive equations such as the Fick's law for diffusion and the Fourier's law for heat transfer by conduction. Finally, the boundary and initial conditions are provided for each subsystem.

Once the complete mathematical model has been developed, one needs to solve the governing equations. A numerical method is usually used. Finite difference, finite element, and finite volume are the methods commonly used in these problems. Commercial computational fluid dynamics packages are also options to run the simulation.

Solid oxide fuel cells can be categorized with respect to cell and stack design, type of support, flow configuration, temperature level, and fuel reforming type [52]. The cell design in a SOFC can be planar, tubular or monolithic. Both, microscopic and macroscopic modeling approaches can be found in the literature. The focus of the microscopic models is more on the performance of electrodes and electrolytes and ultimately in building better electrodes and electrolytes for fuel cells; in the macroscopic point of view, optimization and the overall performance of the system is the target[52-53].

1.2.2 **Phenomena/Processes to Be Accounted for**

Fuel cell technology is a multi-disciplinary area. Materials science, electrochemical and transport phenomena are all involved in a fuel cell. Mass, momentum, species, charge and energy conservation principles provide the fundamental governing equations, as listed in Table 1-1. The reaction kinetics appear as source or sink terms in these equations. The continuity equation is the governing equation for mass conservation. Navier-Stokes equations should be solved for momentum transfer to obtain velocity profiles. To obtain the temperature profile, energy balance equations should be considered. Solving simultaneously mass, energy and momentum balances accompanied by electrochemical models relating the fuel and air gas streams composition and temperatures with the voltage and current density provide one with temperature, velocity, and chemical species distributions as well as fuel cell performance quantification.

The cell outlet voltage is calculated on the basis of the Nernst potential minus several losses. The thermodynamic or Nernst potential is the maximum voltage, which occurs at zero current. The actual output potential is lower than the Nernst potential because of several potential drops/losses. There are three types of potential losses, each resulting from a different dominant resistance[54]. The voltage drop across a particular "circuit element" is referred to as the polarization. The three losses (polarizations) are activation polarization, the ohmic polarization, and concentration polarization.

At low current density (typically less than 20 mA/cm^2), the cell outlet voltage shows an initial rapid decrease with increasing current and then levels out. This rapid drop in voltage is referred to as activation polarization. This voltage drop corresponds to the activation energy barrier for the chemical reactions occurring at the electrocatalyst surface. The Butler-Volmer equation is used to describe the activation polarization.

After overcoming the activation barrier for chemical reactions, the voltage drop increases linearly with increased current density. This linear voltage-drop increase is referred to as ohmic polarization. This voltage loss is primarily associated with the ohmic resistance to oxygen ion /proton flow across the electrolyte.

Concentration polarization is caused by resistances to reactant mass transport via diffusion from the gas flow channels through the porous gas electrodes to the electrode/electrolyte interface. This phenomenon decreases the partial pressures of reactants at the reaction sites, while causing higher partial pressures for the products there.

1.2.3 Lumped-Parameter Mathematical Modeling

The simplest approach to dynamic modeling fuel cells is to ignore spatial changes and to consider changes with time only. A great number of studies considering lumped-parameter models for the systems can be found in the literature. In this section, we review some of these studies (Table 1-1).

There have been many studies on lump-parameter modeling of SOFCs. In one such study by Padulles et al.[5], a model for an SOFC-based power plant was developed to be used in a power system simulation package. Assumptions that were made included: gases in the system were ideal; the pressure along the channels was constant; only ohmic loss was present at moderate cell currents, and the cell temperature was constant. Operating regions of the plant were determined using voltage-current and power-current plots. In the same year, to simulate the transient operation of a tubular SOFC, Hall and Colclaser[6] developed a model that accounted for electrochemical, thermal, and mass transport phenomena in the cell. The transient response of the cell to load changes was investigated. For example, terminal-voltage transient response of the cell showed an overshoot before settling down to a new steady state. The effect of load changes on the cell temperature was also studied. To study dynamics and stability of an SOFC, Sedghisigarchi and Feliachi[7] developed a nonlinear dynamic model that accounted for temperature dynamics and output voltage losses. The cell outlet voltage response to changes in the load and the fuel flow rate was simulated to study the dynamic behavior of the SOFC in the presence of fast and slow perturbations. Their simulation results showed that the stack temperature strongly affects the outlet voltage. They also found that for very fast load variations, temperature and species-concentration dynamics can be ignored, but that over short time horizons these dynamics should be accounted for. Lu et al.[8] developed a model of a standalone vehicular SOFC auxiliary power unit (APU). The SOFC APU model had three components: a controller model, a power electronic circuit model, and an SOFC plant model; the latter consisted of an SOFC stack module, two heat exchanger modules, and a combustor module. They also developed nonlinear dynamic models for SOFC stacks, the heat exchangers and the combustors. The SOFC APU model coupled with a controller and a power circuit model was capable of predicting the dynamics of all SOFC APU components, as well as the transient response of the SOFC APU to external loading changes.

In 2009, a model of an SOFC was developed by Gebregergis et al.[9], who took into consideration the effects of reactant and product concentrations, polarizations (losses), and internal resistances. Partial pressures of species were represented by an equivalent RC circuit in the lumped-parameter model. Predictions by this model were compared with predictions by a detailed spatially-distributed model and with laboratory experiments. The steady-state simulation results were in good agreement with the experimental data. They reported that the capacitance in the simplified equivalent RC circuit can be adjusted to match the exact dynamic response of the physical fuel cell. In the same year, Hajimolana and Soroush[10]developed a dynamic compartmental model for a tubular SOFC. The model accounted for diffusion processes, inherent impedance, transport (heat and mass transfer) processes, electrochemical processes, anode and cathode activation polarizations, and internal reforming/shifting reactions. Dynamic outlet voltage, current and fuel-cell-tube temperature responses of the cell to step changes in external load resistance and conditions of feed streams were simulated. They found that the temperature and pressure of the inlet air stream and the temperature of the inlet fuel stream have the strongest impacts on the dynamics of the fuel cell system.

1.2.4 **Spatially-Distributed Mathematical Modeling**

Fuel cell systems are inherently spatially distributed systems. In view of this, many efforts have been made to develop 1-D, 2-D, and 3-D models of fuel cells. In this paper, we try to review many of these modeling studies for SOFCs. Both, transient and steady state performance studies can be found among these.

One of the pioneering works in SOFC modeling is that of Vayenas et al.[11], who modeled a cross-flow monolithic fuel cell. They assumed that there is no net heat flux in one direction, and thus their model is a two-dimensional one. They solved the two-dimensional model equations numerically and calculated the distributions of concentrations, temperature, and current density. In addition, they reported results on thermodynamic energy conversion efficiency, and volumetric power density. In 1991, Ahmed et al.[12] developed a mathematical model to simulate the electrochemistry and thermal hydraulics in a cross-flow monolithic SOFC. The cell was discretized into many nodes. For each node, steady-state heat and mass transfer equations were written. The model predicted temperature, fuel and oxidant compositions and partial pressures for the entire cell. Energy efficiency, fuel utilization, and power density were calculated. The effects of changes in operating conditions and design parameters on the above-mentioned variables were studied. Simulation results showed that partial pressure of hydrogen decreased along the fuel flow direction, while it stayed constant in the air flow direction. The Nernst potential decreased significantly at the fuel inlet end, while it dropped gradually towards the fuel outlet end due to the dependence of the Nernst potential on hydrogen partial pressure. A one-dimensional tubular SOFC model was developed by Hirano et al.[13]. The model included an inner reforming process. The fuel in the anode side included CH_4, CO_2, CO, H_2O and H_2. The temperature distribution was assumed to be one-dimensional (temperature varied along the length of the cell tube only), and heat transfer by radiation was not taken into account. The model predicted the cell current-density, gas density, bulk temperature, and species concentrations distributions. In 1994, Achenbach[14] developed a dynamic, 3-D mathematical model of a planar SOFC. Heat transfer by conduction, convection and radiation was taken into account. Species mass balances for the fuel and air channels were written. Effects of multi-component diffusion and diffusion in the porous electrode were neglected. Internal methane-steam reforming and recycling of the anode gas were considered. The effects of different flow configurations (co-, counter-, and cross-flow) were investigated, and the response of the cell voltage to load changes was studied. In the same year, Costamagna et al.[15] introduced a fluid dynamic computational model to study the mass flow distribution in the fuel cell stacks. The reliability of the theoretical predictions was validated using experimental data. They measured pressure and velocity distributions at various Reynolds numbers and for different geometrical shapes of the manifolds, and observed good agreement between the experimental and numerical results.

In 1995, a 3-D mathematical model of a tubular solid oxide fuel cell was developed by Bessette et al.[16]. All electrochemical and thermal factors including all necessary modes of heat transfer were accounted for in the model. All parameters values used in the model were obtained from independently measured electrochemical and thermophysical properties. The model was validated with single-cell test data from Westinghouse; the model electrochemical and thermal predictions were within five percent. In 1996, Ferguson et al.[17] presented a 3-D mathematical model of an SOFC. Radiative heat transfer was not considered in the model. A finite difference method was used to solve the model equations numerically. Local distributions of temperature, electrical potential and concentrations of the chemical species for various geometries (tubular, planar, and cylindrical SOFCs) were calculated. The model predictions were in good agreement with experimental data. Using the model, optimum values for cell-design parameters such as cathode thickness and rib width were determined. In 1996, Costamagna[18] presented a 2-D model for a rectangular planar SOFC with an integrated air pre-heater. Cold ambient air was pre-heated with the hot outlet air stream of the cell counter-currently in a heat exchanger. The fuel (pure hydrogen) in the anode side and the pre-heated air stream in the cathode side flowed co-currently. It was concluded that this fuel cell design reduces the cost of an external air pre-heater, because it requires lower air flow rates and lower inlet temperatures. Local quantities such as current density, gas and solid temperatures were reported, and cell performance characteristics were predicted. A parametric study of the effects of oxygen utilization and heat-transfer conditions in the pre-heater, on the local temperature distribution of the solid structure was also conducted. Boersma and Sammes[19] developed a 2-D model for an SOFC stack to calculate flow and pressure distributions in the stack. The cell stack was modeled as a set of series and parallel connections of hydraulic resistances. The feed and waste gases were assumed to flow in opposite directions. The numerical results showed that in the design of internal-manifold SOFC stacks, more attention should be paid to the distribution of the cathode gas than to the distribution of the anode gas.

In 1999, Yakabe et al.[20] presented a 3-D mathematical model of an anode-supported planar SOFC. A single-unit with double channels and a counter-flow pattern was considered. The gas flow in the porous anode was modeled by Darcy's law, and the transport of reactant species to the electrolyte interface by multi-components diffusion. The flow distribution and the distributions of the chemical species were calculated using the finite volume method. The simulation results showed that at high fuel utilization the shift reaction effectively decreases the concentration polarization. To study the transport of gases inside SOFC anodes, Lehnert et al.[21] modeled gas transport in SOFC anodes. They developed a one-dimensional model accounting for diffusion, permeation, and the kinetics of the reforming reaction and the electrochemistry. The transport of gases in the porous electrodes was modeled on the basis of the mean transport pore model. The permeation molar flux density was expressed by Darcy's law. This study revealed that (i) internal steam reforming in SOFC cells causes inhomogeneous temperature distributions due to the fast reforming reaction kinetics, and (ii) the inhomogeneous temperature distributions results in thermally induced stresses, which can cause mechanical failure of the material. Sensitivity analysis was performed to study the influence of structural parameters of the anode Ni/YSZ porous cermet, a composite material composed of ceramic (cer) and metallic (met) materials, on the methane conversion rate. The results showed that among the structural parameters of the cermet, the ratio of porosity to tortuosity has the most influential role in methane conversion. It was also concluded that lowering this ratio decreases the overall methane conversion. Iwata et al.[22] developed a mathematical model for a planar SOFC accounting for mass, charge and heat balances along the flow direction. They considered a quasi-two dimensional (x-y) model for co- and counter-current flow patterns and a three dimensional (x-y-z) model for cross flow pattern in their simulations. The plug flow assumption was made for all gas streams. The flows of fuel and air were along the x direction in the case of co- and counter-flows, and the flow of air was in the *z* direction for the cross-flow case. The potential distribution was along two directions for the co- and counter-flow cell, and along three directions for the cross-flow cell. In the gas channel, mass transfer by diffusion was neglected and only mass transfer by convection was considered. The mass transfer in the porous electrodes was modeled through the Stefan–Maxwell equation. Simulation results showed that the electrolyte temperature increased along the flow direction in the co-current case, and the electrolyte temperature profile had a peak near the fuel inlet in the counter-current case. They also studied the effects of the gas re-circulation ratio, operating pressure and physical properties on the current and temperature distributions. In a second study by Yakabe et al.[23], a 3-D mathematical model for a planar SOFC was presented. The model accounted for the internal or external steam-reforming, the gas-shift reaction, and the diffusion of the gaseous species in the porous electrodes. Concentrations of the chemical species, temperature distribution and potential distribution for co-flow and counter-flow patterns were calculated using a finite element method. The effects of the cell size, the operating voltage and the thermal conductivity of the cell components on the cell performance were also studied. Stress distributions resulting from the simulated temperature distributions in the electrolyte and the inter-connector were obtained. The simulation results showed that the internal reforming caused a steep drop of fuel temperature near the inlet, leading to large tensile stresses in the electrolytes. The co-flow pattern alleviated the problem of the steep temperature gradients, and hence diminished the internal stresses.

Aguiar et al.[24] presented an indirect internal reforming SOFC model consisting of two coupled models: one for the steam reforming reactor and one for the solid oxide fuel cell. In their annular design the fuel cell was constructed around a tubular reformer. The steam reforming reactor was modeled as a conventional heterogeneous, two-dimensional reactor, accounting for intra-particle mass gradients and inter-particle thermal gradients. They presented a one-dimensional steady-state mathematical model for the SOFC part. Radiative heat transfer between the SOFC solid structure and the reformer wall was taken into account, but pressure drop along the cell channel was ignored. Their simulation results showed that the use of typical metal-based steam-reforming catalysts (e.g., Ni) results in full methane consumption and undesirable local cooling in the first one-third of the reformer. Decreasing the activity of the catalyst led to smoother temperature profiles, but in practice it can result in some methane slippage to the SOFC fuel channel. Parameter sensitivity analysis was also performed. Decreasing the fuel inlet temperature was shown to give a smoother temperature profile at the reformer entrance, which can lead to an undesirable temperature rise along the tube. By reducing the current density or raising the operating pressure, the system efficiency increased and the overall temperature rise across the cell dropped. Furthermore, an increase in the pressure reduces the temperature drop caused by the reforming reactions. The original counter-flow (counter-flow of the air and fuel streams in the fuel cell) configuration was compared with one having co-flow. It was observed that for the former configuration the temperature increases along the air flow direction, with a peak at the outlet, while for the latter one the temperature profile has a peak near the fuel outlet.

Recknagle et al.[25] presented a 3-D mathematical model of a planar SOFC with different flow configurations (co-, counter-, and cross-flow). The model had the capability to predict the flow and distribution of anode and cathode gases, temperature and current distributions, and fuel utilization. A computational fluid dynamics package was used to solve the partial differential equations while imposing ‘cyclic’ boundary conditions at the top and bottom of the model domains. The lateral walls were assumed adiabatic. Simulation results showed that fuel utilization was similar for the three flow configurations at a given average cell temperature, but temperature distributions were different depending on the design geometry and the flow configuration. The co-flow case showed the most uniform temperature distribution and the smallest thermal gradients, both thermo-structural advantages over the other flow cases. Haynes[26] simulated a tubular SOFC, to predict the operating conditions under which changes in the load demand can be accommodated safely without constraining the cell stack's response. Electrochemical phenomena as well as thermal transport phenomena were accounted for. It was found that thermal response is orders of magnitude slower than the electrical response; therefore, the two phenomena may be considered as decoupled. The results showed that at higher operating voltages, changes in cell stack load can be accommodated better. Another operating condition considered in this study was fuel utilization. The analysis revealed that depletion issues, such as concentration polarization, hinder power generation at larger fuel utilizations. Thus, lower fuel utilization and higher operating voltage are key operating conditions in accommodating higher load demands.

Beale et al.[27] modeled a single cell as well as a stack of planar SOFC using three different approaches: (a) a detailed numerical model (DNM) of flow, heat and mass transfer and electrochemistry, (b) a flow-based method based on a distributed resistance analogy (DRA), and (c) a presumed-flow method (PFM). They neglected heat transfer by radiation. For the single cell, the simulation results showed that (a) all of these methods provide adequately accurate predictions in planar SOFCs and (b) the DNM is the most accurate method. For large stacks of fuel cells, the DNM approach requires extensive computation time. Ota et al.[28] developed a 1-D model which predicted current and temperature distributions in a single tubular SOFC. Equations describing an equivalent circuit as well as heat and mass transfers were included. Heat transfer by radiation was considered between cell and air feed tube, but it was neglected between cells. The transient response of the cell to step changes in the external load was simulated. The high speed of the response suggested the suitability of the fuel cell for transportation application. Petruzi et al.[29] developed a 3-D global model for an SOFC. They obtained temporal and spatial profiles of temperatures, current and power densities, and chemical species concentrations for the entire system. Concentration polarization due to mass transfer resistance was neglected. Four stages of operations, heat-up, start-up, steady-state, and cool-down, were considered in their simulation studies. The simulation results showed that the air mass flow is an appropriate manipulated variable for regulating heat-up, start-up and steady-state operations. An axially-symmetrical 2-D model of a tubular SOFC was developed by Li and Chyu[30]. Momentum, energy, and species transport were considered in the model. The reforming and shift reactions along with the electrochemical reaction were accounted for. The three layers of anode, electrolyte and cathode were represented by a network circuit, allowing for evaluating the cell current (charge transfer rate). The simulation results demonstrated (a) the existence of a hot spot near the closed end of the cell tube at low operating current density and (b) the movement of the hot spot towards the open end of the cell as the current density increased. Also, at higher current densities the temperature distribution profile was more uniform. A large variation in the oxygen concentration profile was observed, and accordingly the molar fraction of oxygen in the air channel (bulk) was very different from that of oxygen in the cathode/air interface. In the fuel channel, unlike the air channel, the species mole fraction profile between the bulk flow and the anode/fuel interface was practically flat.

Ackmann et al.[31] also developed a 2-D model for a planar SOFC. The electrochemical reactions, the reforming and shift reactions, the heat-transfer and the mass transfer processes were included in the model. Mass transport of gases in porous electrodes was described using the mean transport pore model. The structure of the porous medium was assumed isotropic based on this model. Three structural parameters, the ratio of porosity (ε) to tortuosity (τ), the mean value of the pore radii, and the mean value of squared pore radii were shown to strongly influence the cell performance. Heat transfer by convection was neglected in the anode side after calculating the Pe'clet number and determining that the dominant mode of heat transfer was conduction. Temperature and concentration profiles in the porous electrodes of the SOFC were calculated. The results showed that the temperature profile in the cathode part was more homogeneous. In the anode side, the temperature gradient was steeper, and a maximum temperature was observed. Campanari and Iora[32] developed a finite volume model of an SOFC. Cell internal temperature and flow composition profiles, fuel and oxidant utilization, cell power output, and cell voltage were predicted by this model. Heat transfer by radiation between the solid cell structure and the gas flow was neglected due to the dominant effect of convective heat transfer. A sensitivity analysis was conducted to examine the effects of key model parameters on the cell performance. The model was validated with experimental data, confirming the accuracy of the model in predicting the SOFC behavior. Aguiar et al.[33] developed a model for an anode-supported, intermediate-temperature, direct internal reforming planar SOFC in co-flow and counter-flow configurations. They included mass and energy balances, and an electrochemical model that draws a correlation between the fuel and air gas composition and temperature to voltage and current density. Effects of changes in inlet temperature, fuel utilization, and average current density on the steady-state performance of the SOFC were analyzed. Steep temperature gradients and uneven current density distributions were observed in the case of the counter-flow operation. In another publication[34], the same group studied the dynamic response of the cell using the same model. The open and closed-loop transient responses of the SOFC to load step-changes were analyzed. The results showed that the cell temperature increased along the direction of fuel and air flows, with the maximum temperature occurring at the outlet. Open-loop dynamic simulations showed that the cell potential response to step changes in the load had an overshoot or an undershoot before reaching a new steady state.

Li and Suzuki[35] proposed a quasi-2-D model for a single tubular SOFC. Momentum, heat, and mass transfer were considered as axisymmetric. The model incorporated the air and fuel flow velocity fields, ohmic and thermodynamic heat generations, convective heat-transfer, mass transfer of chemical species, and the electrochemical processes. Heat transfer by radiation was not considered in this study. The model overpredicted the cell terminal voltage at low electric current densities. The justification for this over-prediction is that at low current densities the cell temperature is low, making the reaction sluggish (creating high activation potential). The high activation polarization was not accounted for in the model. The authors suggested considering more accurate correlations for the activation and concentration polarizations in their future studies.

Xue et al.[3] developed a dynamic model of a single tubular SOFC using the control volume (CV) approach. The model accounted for the effects of conduction, convection, radiation, species transport, and electrochemical reactions. The authors analyzed the spatial distributions of a series of state variables under both steady-state and transient conditions and assessed the system dynamic behavior. The existence of non-uniform current and Nernst potential distributions along the longitudinal direction was observed. This was attributed to non-uniform fuel and gas partial pressures along the flow direction, and the temperature distributions in the anode and cathode channels and the cell tube. As a result of the nonuniform distribution of the Nernst potential along the longitudinal direction, the external load voltage played an important role in the cell performance. The model predictions were compared with experimental data, such as the polarization curve and power density, to validate the model. A nonlinear dynamic model of an SOFC accounting for the diffusion processes and the cell impedance was derived by Qi et al.[36]. A new equivalent circuit for the cell was proposed. Dynamic responses of voltage, current, and gas consumption rates to load and partial pressure changes were simulated. The results indicated that reactant diffusion processes from the bulk gas flows to the triple phase boundaries play an important role in the dynamic behavior of the SOFCs. It was found that influences of pressure disturbances in the gas bulk flows on the voltage and current were relatively small. Unlike the gas stream pressures, the temperature had a strong effect on the behavior of the fuel cell. The strong effect is due to the dependence of the conductivity of the electrolyte, electrodes and connectors, the Gibbs free energy and the Nernst voltage on temperature. Iora et al. [37]compared two models of an anode-supported intermediate-temperature direct internal reforming SOFC to each other. In the previously-reviewed model[33], thermodynamic, physical, and flow properties were assumed to be constant and equal to their inlet values. To analyze the effect of this assumption, Iora et al.[37] developed another SOFC model that accounted for variations in the gas properties in the fuel and air channels. The detailed model could calculate the gas velocities, physical properties, and pressure distribution along the gas channels. Both steady state and dynamic simulations were carried out. In the steady-state case, it was found that the overall effect of the constant property assumption on the cell performance was weak; the cell efficiency was different by less than 1%. In the transient study, the results obtained for the cell outlet voltage and the fuel exit temperature profiles showed steady-state errors lying between the predictions of the two models. The magnitudes of the steady-state errors were larger at higher current densities. It was concluded that the detailed model should be used for high current density cases.

Mueller et al.[38] developed a 2-D dynamic model for an SOFC. This SOFC model was integrated with simulation modules for a reformer, a combustion chamber, and a heat dissipater to form a system model that can simulate an integrated 25 kW SOFC system. They discretized each of the major component models in the primary flow direction. The simulation results showed a good agreement with the real-time data from the actual system. Voltage response to changes in hydrogen concentration was investigated, and the results demonstrated the importance of maintaining fuel utilization during transient operation. For an SOFC operating with a syngas fuel, Suwanwarangkul et al.[39] derived a 2-D isothermal model that accounted for momentum, mass and charge transport coupled with electrochemical and chemical reactions. The model was validated with experimental data for various syngas compositions. At 800°C the model predictions diverged from experimental data. Suwanwarangkul et al.[39] studied this phenomenon by analyzing the SEM image of the anode surface after each experiment. The analysis showed carbon deposition on the anode surface, and that the Ni catalyst delaminated from the anode during the cell operation. On the other hand, at higher temperatures like 900°C, no carbon deposition was observed. They also analyzed carbon formation from the thermodynamic point of view. The analysis showed that the operating pressure, temperature, and inlet H2 and CO compositions are important factors. The main problem in operation with syngas at intermediate temperature and high pressure was carbon formation. The authors proposed that this problem might be overcome by adding H2O or CO2 into the syngas fuel. In the same year, Qi et al.[40] proposed a dynamic model to simulate the mass/energy/ momentum transport dynamics including the internal reforming/shifting reactions for a finite volume of cell in the form of a nonlinear state-space model. Effects of diffusion, intrinsic impedance, fluid dynamics, heat exchange and direct internal reforming/shifting reactions were taken into account. Simulation results showed that fuel flow, inlet pressure and inlet temperature play important roles in the dynamic performance of the SOFC. It was also shown that the cathode side air inlet temperature has the strongest effect on the SOFC performance, and that the dominant (slow) fuel cell dynamics is dictated by the cell temperature due to its large heat capacity.

The dynamic 1-D tubular SOFC stack model developed by Jiang et al.[41] accounted for the electrochemical and thermal processes, the voltage losses, and the temperature dynamics. The cell was divided into several elements along the flow direction by the finite volume method, and for each element the governing equations were solved. The modeling of an external reformer was also included in this study. An equivalent circuit was presented to assess the effects of the current pathway length on the ohmic loss of the tubular SOFC. It was found that (a) a higher operating pressure improved the cell performance, and (b) higher operating temperatures decreased both the Nernst potential and the irreversible losses, resulting in an initial increase and a subsequent decrease in the cell efficiency. The accuracy and reliability of the model was validated with experimental data from the literature.

Attempts have also been made to develop SOFC models for real-time applications. An example of such a study is by Cheddie et al.[42], who developed a 1-D dynamic model of a planar SOFC. The model took into account all transport and polarization phenomena. It was simplified to allow computational times in the order of milliseconds. Because of the much faster dynamics of the electrochemical process, the quasi-steady-state assumption was made for the faster dynamics. Predictions of this model were compared to predictions of a full-order model using a finite element mesh with iterative solvers. The model predicted that using a smaller number of channels with larger cross-sectional areas significantly reduces the pressure drop, and hence increases the net power produced by the cell.

To analyze the effect of the length of a tubular SOFC on the steady state and transient performance of the cell, Jia et al.[43] developed a model that accounted for electrochemical and thermal effects. Nernst potential and ohmic, activation and concentration polarizations were considered in the model. Heat transfer by conduction, convection and radiation between the cell and the air feed tube was incorporated in the heat conservation equations. Effect of various operating parameters, such as temperature and gas concentrations, were analyzed in this study. The results demonstrated that increasing the tube length leads to an increase in the overall cell tube temperature but affects the cell output voltage and power density very slightly. Bedogni et al.[44] studied a circular-planar type intermediate temperature SOFC both experimentally and theoretically. They developed a 1-D model to simulate the SOFC by a finite-volume approach. The model was capable of predicting cell internal temperature and flow composition profiles, fuel and oxidant utilization, cell power output, cell outlet voltage, and cell current output. The cell losses were evaluated by means of a total resistance approach. Experiments were carried out for several single cells fuelled with hydrogen. The model was validated using experimental voltage–current data. A comparison of experimental and modeling results demonstrated the capability of the model for predicting single cell behavior; the model could reproduce the operation with natural gas or partially reformed syngas fuel. Li et al.[45] presented a 2-D mathematical model of a direct internal reforming SOFC. The reforming reaction kinetics, mass and heat transfer were taken into account. The dynamic model was simulated by applying step changes in fuel flow rate, air flow rate, and stack voltage. The temperature distribution, current density distribution and gas species molar fraction distributions were presented. The results showed that the dynamic responses were different at each point in the stack, and a moderate increase in the fuel flow rate could improve the fuel cell performance. A decrease in the air flow rate increased the stack temperature and the fuel and oxygen utilizations as well. It was concluded that the fuel and air flow rates should be used to balance the performance improvement with temperature optimization in practical applications.

Bao and Cai[46] developed a 1-D, isothermal mechanistic model for the anode of an anode-supported SOFC. Two approximate analytical solutions considering both mass and charge transport were developed. They divided the anode into an inactive and an active zone. The regular perturbation method was applied to estimate the distribution of the fuel concentration and overpotential. Both approximate solutions were in agreement with the numerical solution in the case of medium and low electric load. To study a methane-fed SOFC using a proton conducting electrolyte and an oxygen-ion conducting electrolyte, Ni et al.[47] developed a fuel cell model that considered both the internal methane steam reforming and the gas shift reactions. All voltage losses including activation, ohmic and concentration overpotentials were accounted for in the model. The results obtained by this study showed that the actual performance of the methane-fed proton conducting SOFC was lower than the anion conducting SOFC due to higher ohmic overpotential of the former. In a dynamic 1-D modeling study, Qi et al.[48] considered a tubular SOFC. Diffusion, inherent impedance, primary flow, heat transfer, and the internal reforming and shifting reactions were taken into account. The resultant model included a set of partial differential equations dependent on both time and axial position. An approximate analytical solution for the reacting gas-flow problem was proposed to convert the distributed model into a control relevant nonlinear state space model. The proposed approach reduced the computational cost and thus eased dynamic simulations. Dynamic responses of a set of variables to step changes in the external current and the fuel and air inlet stream conditions were studied. Jeon[49] developed a 2-D model of intermediate-temperature anode-supported SOFCs. Conservation of electrons and ions, conservation of momentum, conservation of mass, and conservation of energy as well as electrochemical characteristics and micro-structural properties were taken into account. It was found that the cell potential increases with temperature at higher temperatures. However, the potential increase was insignificant at very high temperatures due to decrease in the effective diffusivity in the anode functional layer. The simulation results revealed that the performance and the distributions of current density, overpotentials and mole fractions of gas species were strongly dependent on temperature. To analyze the performance of an SOFC, Goldin et al.[50] built on a 3-D mathematical model that accounted for fluid flow, heat and mass transport, porous-media transport, elementary catalytic chemistry within the electrode structures and electrochemical charge transfer. Simulation results demonstrated that at low inlet flow rates significant compositional variations in the gas compartments are observed. By increasing the flow rates, the fuel cell operates such that the gas composition is minimally depleted. An isothermal dynamic model of an anode-supported tubular counter-flow SOFC was developed by Bhattacharyya et al.[51]. They considered the species conservation in the gas flow channels, mass transport dynamics inside the porous electrodes, and the electrochemical reactions along with loss mechanisms. Step changes in voltages and flow rates were made to explore the system response. The simulation results were found to be in good agreement with experimental data.

1.3 Steady State Behavior

The steady-state behavior of fuel cells has been studied by many groups. There have been a number of studies on the steady-state behavior of SOFCs[55-56]. In comparison to SOFCs, more studies on the steady-state behavior PEMFCs with hydrogen as a fuel and direct methanol fuel cells (DMFCs) have been reported[57-64]. For both fuel cell types, steady-state multiplicity has been observed and reported. Here, we review some of the theoretical and experimental studies, listed in Table 1-2, that have pointed to the existence of steady state multiplicity in the fuel cells.

Table 1-2. Studies on Steady Sate Multiplicity in PEMFC and SOFCs.

Fuel cell type	Number of steady-states	Stated cause of steady state multiplicity	Theoretical/experimental method	Reference
SOFC	One, three, or five	Temperature dependence of electrolyte conductivity	Theoretical/0D and 1D distributed	56
PEMFC	One or three	Positive feedback between the water produced by the reaction and the transport of	Experimental/fixing the load resistance and cell temperature	57

		protons in the membrane		
PEMFC	One, three or five	Coupling of mechanical properties of the membrane, functions of temperature and water contents, to its chemical and transport properties	Experimental/ steady state and dynamic responses to changes in temperature, flow rates, and external load resistance	[58]
PEMFC	One or two	Positive feedback between the membrane resistance and water production	Theoretical/dynamic responses to changes in load	[59]
PEMFC	One or two	Dependence of membrane conductivity on cell potential which is due to potential-assisted surface migration of protons from one sulfonate group to the other on the surface of very narrow pores in the hydrated PEM membrane	Experimental/various external resistive loads	[60]
PEMFC	One or two	Dependence of conductivity on potential	Experimental and Theoretical/mathematical model accounting for exponential dependence of membrane conductivity on potential	[62]
PEMFC	One, three or five	Autocatalytic nature of the interplay between water and the reaction rate	Theoretical/Bifurcation techniques	[63]
PEMFC	One or two	Feedback mechanism involving the nonlinear coupling between liquid water accumulation and oxygen depletion	Theoretical/effect of cathode catalyst layer(accounts for the full coupling of random porous morphology, transport properties, and electrochemical conversion)	[65]
PEMFC	One or two	Lateral flux of water in the plane of the ionomer membrane	Theoretical/accounted for lateral diffusion of water	[66]
PEMFC	One, two or three	Relative humidity and water transport	Theoretical/bifurcation analysis	[67]

1.3.1 **Steady State Multiplicity**

The earliest theoretical study on high temperature SOFCs that indicated the existence of multiple steady states dates back to 1983. In their work, Debenedetti et al.[55] presented a mathematical model that included material and energy balances.

They assumed that both the anode and cathode were well mixed and there was no temperature gradient within the chambers. The model was solved numerically to predict the steady-state behavior of the system. The results obtained revealed some striking similarities between fuel cells and chemical stirred tank reactors (CSTRs), including ignition-extinction phenomena and steady-state multiplicity. The dimensionless heat removal (linear) and heat generation (S-shaped curve) were plotted in the same diagram as a function of dimensionless temperature (T/T_{feed}). It was shown that the fuel cell may have one or three steady states. When there are three steady states, the middle steady-state is unstable, while the other two are stable. Mangold et al.[56] also investigated steady-state multiplicity in a SOFC. They proposed two models for the SOFC, a lumped model and a spatially distributed 1-D model. Three modes of operation (potentiostatic, galvanostatic and constant load) were considered in their simulations. The temperature dependence of the electrolyte conductivity was taken into account by an Arrhenius relation. In the lumped model, the heat generation term and heat removal term were plotted in the same graph to find the intersection points corresponding to steady states. In the case of galvanostatic operation, one intersection point was found, which implies the presence of one single steady state in the system. They mentioned that the constant current fixes the reaction rates of the cell and accordingly inhibits the nonlinear effects of reaction kinetics. In the case of potentiostatic and constant load operation, up to three steady states can be found. As in the exothermic reactors, the heat production curve is sigmoidal for the potentiostatic operation, which is in agreement with Debenedetti et al.'s results[55]. In the case of the spatially distributed model, bifurcation analysis elucidated the presence of up to five steady states in the potentiostatic operation due to the additional spatial degrees of freedom. Three regions of five steady states (three stable, two unstable), three steady states (two stable, one unstable), and one single stable steady state were observed in this case. In the galvanostatic operation, unlike in the lumped model, up to three steady states can coexist in the system. The reason is that the constant current constrains the total heat generation not the heat distribution. One can conclude that the temperature dependence of the electrolyte conductivity plays a key role in the occurrence of multiple steady states. The electrolyte conductivity increases with increasing temperature, and it results in the formation of hot spots and channels of high current density in the system[56].

Multiplicity can also occur in PEMFCs as in SOFCs. Moxley et al.[57] were first to discover and report steady state multiplicity in a PEMFC. They also developed a differential reactor functioning as a stirred tank reactor (STR) PEMFC to study fuel cell dynamics. Steady state multiplicity in the PEMFC was explained to be caused by water balance in the cell. Water is produced by electro-reduction reaction at the cathode side, while being removed from the membrane by convective flow of gases through the cell. At steady state conditions, the rate of water removal is equal to water production. Similar to SOFCs and auto-thermal reactors, where heat removal and generation were drawn to find the intersection points, steady states can be found by graphically drawing of water removal and water generation terms as function of water activity in a PEMFC. Depending on the load resistance and temperature, one or three steady states were reported[57-58]. At a high resistance and high temperature, there is a single intersection point corresponding to the extinguished steady state. Three steady states can exist in the case of moderate load resistance and low temperature. The three steady states are the ignited, or high current steady state, the extinguished or low current steady state, and the intermediate steady state. The first two steady states are stable, but the third one is unstable. Positive fluctuations in the system from the intermediate steady state can cause the system to move towards the ignited state, and negative fluctuations can lead system towards to the extinguished state. The multiple steady-states phenomenon originates from the effects of membrane hydration on proton conductivity. The dependence of proton conductivity on water activity is autocatalytic. More water generation provides more hydration in the polyelectrolyte membrane, and accordingly increases proton conductivity. On the other hand, an increase in proton conductivity accelerates the rate of migration of protons to the cathode side and consequently increases the rate of oxygen electroreduction and produces more water for membrane hydration. Thus, the positive feedback between proton migration and water production provides the conditions for steady state multiplicity. In another study by Benziger's group[58], they presented experimental and theoretical results for temperatures above $70^{o}C$ where up to 5 steady states (three stable) can coexist in the case of intermediate load resistance. They proposed that the existence of three stable steady states is due to coupling of mechanical stress relaxation and swelling with chemical and transport effects. Stress relaxation of the swollen membrane causes the jumps in the membrane resistance, and finally creates two stable ignited steady states. Thus, one can conclude that the water activity is not only a function of water production but can also be a function of mechanical properties of the membrane[58]. The problem of varying membrane water content in many PEMFCs has been avoided using a humidified feed[59].

Katsaounis et al.[60] reported steady state multiplicities in a H_2-fed PEMFC with a Pt cathode and a Pt-Ru or C-based anode. They presented a current-voltage (IV) curve, which shows the existence of two cell potential values for each current value, and a maximum current. This behavior is analogous to the results by Mench et al.[61] for direct methanol fuel cells (DMFC). Mench et al.[61] attributed the occurrence of bistability in DMFCs to water flooding in the cathode, and they dismissed the ohmic, activation and diffusion overpotentials as a cause for the bistability. The overpotentials increase with the cell current and thus cannot cause the downward bending in the IV curve. In order to explain this phenomenon physically, they pointed out that proton conductivity contains both the effect of water content in the membrane and the cell potential[60, 62]. The exponential potential dependent part of Nafion conductivity is caused by the potential-assisted surface migration of protons from one sulfonate group to another in the ionic part of ionomer[60]. On this basis, they defined a nonlinear resistance overpotential, different from the linear ohmic overpotential, as the underlying reason of the positive slope in the IV curve and of the resulting bistability in the system. Chia et al.[63-64] expanded their original STR-PEM fuel cell model by including mass transport in the gas diffusion layer (GDL) to capture flooding effects in the cathode side of a fuel cell[63]. The cathode GDL flooding blocks the mass transfer of oxygen to the cathode catalyst surface, as the water liquid accumulates in the pores of the cathode catalyst layer; hence the magnitude of the current drop increases due to an increase in the mass transfer resistance. Bifurcation results from their new model showed a better agreement with experimental results compared to their first model[64]. Furthermore, they considered multiple STR tanks in series to simulate the integral reactor. Using this method, they studied the effects of flow patterns on the cell dynamics. Furthermore, they showed that the flow patterns can be used to determine whether or not the fuel cell can sustain a sufficient level of water to ensure ignition[64]. By using arrays of several tanks in series, they were able to detect regions of higher-current, corresponding to wet spots in the fuel cell array.

Liu and Eikerling[65] considered a model accounting for reactant transport, electrochemical reaction, and water management in a PEMFC. Effects of random porous morphology, transport properties and electrochemical conversion in the cathode catalyst layer were also account for. The authors related steady-state multiplicity in the PEMFC to porous structure and liquid water formation in the cathode catalyst layer. They also showed that liquid water accumulation in pores, oxygen transport, and local rates of current generation play important roles in the occurrence of bistability. As liquid water accumulates in the pores, diffusion of oxygen to active catalyst sites is restricted, leading to non-uniformity in the reaction rate distribution, and inactivity of the main part of the cathode catalyst layer. This sequence of events results in the occurrence of steady-state multiplicity.

Nazarov et al.[66] developed a mathematical model accounting for mass transfer through the plane of membrane (in-plane diffusion) and also in the direction along the membrane plane (lateral diffusion). They proposed the possibility that the experimentally observed high and low currents may correspond not to spatially uniform states of the membrane, but rather to a transition from full ignited state to a partially ignited state, in which some regions are ignited and some are extinguished. By comparing numerical and experimental results, Benziger et al.[58] found out that the in-plane diffusivity in Nafion plays a key role in the duration of the transient behavior and dictates the velocity of the ignition wave. However, the lateral flux of water in the plane of membrane has an important impact on the cell behavior when the cell is very dry and when liquid water forms in the cell. In the both cases, the membrane is significantly sensitive to the hydration level.

From the studies reviewed here, one can conclude that the problem of multiplicity including hot spots in SOFCs and wet spots in PEMFCs should be considered critically. Temperature control is very important in the operation of high temperature SOFCs. Also, the ignition phenomenon is crucial in start-up and control of PEM fuel cells. The physical mechanisms and time scales of these dynamics should be studied comprehensively in order to control fuel cells effectively[63].

1.4 Dynamic Behavior

Study of the dynamic behavior of a fuel cell allows one to learn about the transient behavior of the cell under different conditions[68] and determine dynamic characteristics of the cell, such as apparent dominant time constants, stability of each steady state, and the multi-time-scale nature of the system. It has been reported that a fuel cell system may not provide the required power during the peak demand period or transient conditions[68]. Study of the responses of the system to changes in the external load and various operating conditions will help one design the required power plant. In some cases, the fuel cell should be combined with an energy storage device as a back-up to supply the power required under transient load conditions. One needs to understand the dynamic behavior of fuel cell systems well in order to be able to design an effective controller.

Spontaneous oscillations and chaotic behavior may also be observed in electrochemical systems. Several publications have reported that steady-state instability is caused by negative differential resistance of the process; that is, decrease in the electrical resistance as the current increase. The current and potential can oscillate in potentiostatic and galvanostatic operations, respectively. The system can switch from operating at a stable steady state to operating at a stable limit cycle (oscillatory response) as operating parameters are varied. Therefore, it is quite crucial to study the dynamic behavior of fuel cells to determine regions in which they have oscillatory and/or chaotic behavior and to operate the systems at a desired steady state.

1.4.1 **Multi-Time-Scale Nature**

Fuel cells are inherently multi-time-scales systems. Table 1-3[69] lists estimates of various time scales existing in SOFC systems; the characteristic transient time scales of a planar SOFC can span over nine orders of magnitude. A number of studies[10, 58, 70-73] have investigated the multi-time-scale nature of fuel cells. A summary of these studies is presented in this section.

Table 1-3. Time Scales of a Planar SOFC.[69]

Timescale Name	Timescale(s)
Cell charging Time	10^{-5}
Cathode-gas Electrode Mass Diffusion Time	10^{-5}
Anode-gas Electrode Mass Diffusion Time	10^{-3}
Cathode Electrode Thermal Diffusion Time	10^{-3}
Convective Transport Time	10^{-1}
Cell Reactant Consumption Time	10^{0}
Anode Electrode Thermal Diffusion Time	10^{0}

Anode-gas Streamwise Mass Diffusion Time	10^1
Anode-gas Streamwise Thermal Diffusion Time	10^1
Cathode-gas Streamwise Thermal Diffusion Time	10^1
Cathode-gas Streamwise Mass Diffusion Time	10^2
Cell Heating Time	10^3
Anode Electrode streamwise Thermal Diffusion Time	10^3
Cathode Electrode Streamwise Thermal Diffusion Time	10^4

Benziger et al.[58, 70] found multiple time scales in the dynamic response of a stirred tank reactor (STR) polymer electrolyte membrane (PEM) fuel cell that was operated over the temperature range of 35–105^{o}C. Their results showed the existence of dynamic processes in the PEM fuel cell operation that have at least three distinct time scales: processes that have a response time of less than 1 s, processes that have a response time of about 100 s, and processes that have a response time of greater than 1000 s. They tied the fast response to the current following the load at nearly constant membrane water content, the 100 s response to the adjustment of membrane water content by diffusion, and the slow response to water absorption or desorption from the membrane and mechanical relaxation processes of the membrane.

Various processes with different response times contribute to the dynamics of a PEMFC. Zenith and Skogestad[71] identified a very wide range of the time constants for the fuel cells. The existence of the significantly different time constants gives rise to the combined system dynamics that have multi time scales. The time constant range is from 1ms to 10,000s, with the fastest dynamics being that of a converter and the slowest dynamics being that of the thermal (heat transfer) process. In their study of the voltage response of a PEMFC to a step change in the cooling water temperature, Didierjean et al.[72] identified two time constants that characterize mass transfer in the membrane by water diffusion and by electro-osmosis. The Pe'clet number allowed the comparison of the magnitude of these two transport mechanisms. The fuel cell voltage response to a temperature step change occurred in two stages. The first stage corresponded to the thermal process and the second one to water transport in the membrane.

Hajimolana and Soroush[10] developed a dynamic model for a small tubular SOFC. Their simulation studies revealed the multi time scale nature of the system, as some of the cell output responses exhibited consecutive apparent dominant time constants, ranging from ~0.2 ms to ~40 s. In their study of the dynamic response of an SOFC, Bhattacharyya and Rengaswamy[73] observed three characteristic time constants. The first one was on the order of milliseconds, which is usually neglected in practical applications. The second time constant was on the order of seconds, arising mainly because of the mass-transport dynamics. The third one was on the order of minutes or hours and was dependent on the thermal characteristics of the system.

Accounting for all complexities and details in fuel cell modeling leads to the development of a model that is not computationally efficient. While the multi-time-scale nature of fuel cells makes simulation of a complete fuel cell model harder (make the governing equations very stiff), it can be used to simplify the complete models (conduct model reduction). Processes with time scales outside of the time scale of the modeler's interest can be identified and for these processes, one can make the steady-state or quasi-steady-state assumption, depending on the relative size of the time scale of the process to the time scale of interest. The resulting model will have a lower order, as the assumptions allow one to convert many of the model differential equations to algebraic equations. For processes with time scales/constants significantly smaller than the time scale of interest, quasi-steady-state sub-models are derived, and for processes with time scales/constants significantly greater than the time scale of interest, “steady state” sub-models. For example, if the time scale of interest is smaller than those of the transport processes, then these processes are considered to be at steady state. Alternatively, if the time scale of interest is that of heat transfer processes to describe the cell temperature, the model can be reduced by making the quasi-steady-state assumption for processes governing the mass and charge transfers. As can be seen in Table 2-3, the time constants related to temperature dynamics are greater than those of mass and charge balances.

1.5 Concluding Remarks

The previous sections presented a review of recent publications on mathematical modeling, steady-state and dynamic behavior of solid oxide fuel cells. Mathematical models can help one examine the effects of different parameters, new materials and different designs on the cell performance and cost; they have applications in design, optimization, monitoring and control of the cells. The type and the level of details included in a mathematical model depend on what the application of the model is. For real-time applications, the model equations should be solvable in real-time, which at the present time, limits drastically the set of models that can be used for real-time applications. In fuel cell modeling, the art is not to include every complexity but to include enough details to predict the variables of interest accurately enough. Accounting for every complexity in fuel cell modeling leads to the development of very complex, multi-scale, multi-dimensional models, which may be hard to solve even with the present computers and numerical methods. One effective way of deriving simpler fuel cell models is first to identify the time scale of interest (time scale over which the resulting model should predict accurately) and then to make (a) the quasi-steady state assumption for processes that have time constants much smaller than the time scale and (b) the steady state assumption for processes that have time constants much larger than the time scale. Overall, many studies on SOFC modeling have been conducted, while less model validation has been reported.

The problem of steady state multiplicity including hot spots in SOFCs and hysteresis behavior should be considered critically in the operation of the cells. In SOFCs, the temperature dependence of the electrolyte conductivity plays a key role in the occurrence of multiple steady states. To further investigate the effect of multiplicity, extensive experimental and theoretical studies should be conducted for fuel cell modules and stacks.

2 Chapter 2: Steady State Multiplicity and Dynamic Behavior in an Oxygen-Ion Conducting SOFC

2.1 Introduction

As discussed in the previous chapter, a number of *theoretical* and *experimental* studies of PEMFCs have revealed that the fuel cells can exhibit steady-state multiplicity [57-58, 60, 66, 74]. However, so far, there have been only two *theoretical* studies[55-56] showing that SOFCs can have multiple steady states. As no *experimental* evidence has been reported yet, can a true (realistic) SOFC exhibit steady-state multiplicity? Our first attempt to answer this question is to depart from the simple models considered in[55-56] and study the steady-state behavior of SOFCs described by more realistic models.

In 2006, Mangold et al.[56]also examined steady-state multiplicity in a SOFC. They proposed two models for the SOFC, a lumped model and a spatially distributed 1-D model. Three modes of operations including potentiostatic, galvanostatic and constant ohmic load were considered in their simulation studies. In their lumped model, the temperatures of anode and cathode gas channel were taken constant. Also, concentrations of the reactant and product gas species were assumed uniform and constant in the whole system. The model was developed by writing an energy balance for the solid structure of the cell (cathode, anode and electrolyte as a unit subsystem). In their distributed model, gas species concentrations and temperatures inside the cathode and anode gas channels were assumed to vary with position along the gas flow directions in the channels only; the temperatures and the species concentrations inside the channels and the electrolyte were assumed to be independent of position along the other two axes. Although this model is more realistic compared to the lumped model, it did not take into account concentration polarizations and changes in physical properties. Steady state simulation results under potentiostatic and galvanostatic modes were shown using the distributed model, but bifurcation analysis under constant ohmic load was not reported. Also, the effect of heat convection coefficient and variations in air and fuel inlet velocities on the steady state multiplicity of fuel cell was not investigated in this study.

Thermal management in SOFCs is very important. The existence of the multiplicity in SOFCs can make temperature control of the fuel cells as well as the auxiliary components in the fuel cell systems more challenging and can limit the performance of fuel cell controllers significantly. Fuel cell temperature control is needed to prevent degradation of the fuel cell at high temperatures, and maintain high efficiency because of the strong dependence of the electrolyte conductivity to temperature. Variations in the external load resistance can move the system towards an extinguished state and decrease the efficiency of fuel cells. On the other hand, an ignited state is not always desirable, because different materials used in the system may not tolerate the high temperature of the ignited state, and this may damage the cell, stack or auxiliary components. Therefore, depending on the design of the fuel cell and materials which are used, one needs to investigate the possibility of the system operating in the multiplicity region and determine the optimal operation parameters of the system to circumvent the difficulty of operation in the multiplicity region. When the system is operated within its steady-state multiplicity region, its temperature control becomes more challenging, and linear control may not be adequate.

This chapter presents a bifurcation study of a SOFC based on a mathematical model that is more realistic than the two lumped models considered in the previous studies[55-56]. Advantages of using a detailed lumped model over a distributed one are the lower computational cost and the easier task of solving the model equations numerically. An objective of this study is to investigate the effect of process parameter values on the steady-state multiplicity and the location of steady states. A more detailed mathematical model is first developed. Heat transfer, mass transfer and electrochemical processes are taken into account. Three modes of operation, under constant ohmic load, potentiostatic control and galvanostatic control, are studied. The existence of a unique steady state or multiple steady states in the system is investigated in terms of air and fuel inlet temperatures and velocities, convection heat transfer coefficient, and the external load resistance. The range of operating conditions for which steady state multiplicity exists is determined.

The organization of the rest of this chapter is as follows. Section 2 presents the motivation for this study. Section 3 describes the mathematical model of the SOFC. Section 4 discusses the numerical method used for the steady state and dynamic simulations. Section 5 presents and discusses the steady state behavior of the system. Section 6 presents the dynamic response of the cell to step changes in the external load resistance. Finally, Section 7 presents some concluding remarks.

2.2 Review: Motivation

This section presents a brief review of Mangold et al.'s model and results [56]; I consider and simulate their lumped model and reproduce some of their steady state results. My objective here is to use these results as a motivation for the rest of the chapter and as a basis for comparing my results obtained from a more detailed model presented in the next section.

In Mangold et al.'s lumped model[56], the temperatures of gases in the anode and cathode channels were taken constant. Also, concentrations of the reactant and product gas species were assumed uniform and constant in the whole system. The model was developed by writing an energy balance for the solid structure of the cell (cathode, anode and electrolyte as a unit subsystem). To calculate the voltage across the electrolyte and the activation losses, Nernst equation and Butler-Volmer equation were used, respectively. The activation losses are associated with overcoming reaction energy barriers of oxygen reduction and hydrogen oxidation reactions at the electrode-electrolyte interfaces [75-76]. To account for voltage losses, anode and cathode activation overpotentials and ohmic losses were subtracted from the Nernst open-circuit voltage. Concentration losses were not accounted for in the lumped model used in[56]. Concentration losses (polarizations) are caused by resistances to reactants mass transport via diffusion from the gas flow channels through the porous gas electrodes to the electrode/electrolyte interface. This phenomenon decreases the partial pressures of reactants at the reaction sites, while causing higher partial pressures for the products there. Mangold et al.'s model [56]is in the form:

$$\begin{aligned}&\left(d_A + d_E + d_C\right)(\rho c_p)^s \frac{dT^s}{dt} = \\ &\left(\frac{-\Delta_R H}{2F} - U^{cell}\right)\frac{I}{LB} + \left(\alpha + \frac{c_{p_{H_2}}}{2F}\frac{I}{LB}\right)\left(T^A - T^S\right) + \left(\alpha + \frac{c_{p_{o_2}}}{4F}\frac{I}{LB}\right)(T^C - T^S)\end{aligned} \tag{2.1}$$

$$\frac{I}{LB} = \gamma^C {y_{O_2}}^{0.25} \exp\left(\frac{-E^C}{RT^s}\right)\left\{\exp\left(\theta_a^C \frac{F}{RT^s}\eta^C\right) - \exp\left(-\theta_c^C \frac{F}{RT^s}\eta^C\right)\right\} \tag{2.2}$$

$$\frac{I}{LB} = \gamma^A y_{H_2} y_{H_2O} \exp\left(\frac{-E^A}{RT^s}\right)\left\{\exp\left(\theta_a^A \frac{F}{RT^s}\eta^A\right) - \exp\left(-\theta_c^A \frac{F}{RT^s}\eta^A\right)\right\} \qquad (2.3)$$

$$U^{cell} = U^0 - \eta^A - \eta^C - \rho^E d^E \frac{I}{LB} \qquad (2.4)$$

where the reversible cell voltage, U^0, is calculated by using the Nernst equation:

$$U^0 = E^0 - \frac{RT^S}{nF} ln\left(\frac{p_{H_2O}^{bulk}}{p_{H_2}^{bulk}\, p_{O_2}^{bulk\,0.5}}\right) \qquad (2.5)$$

We use the same model parameter values reported in[56]except for the cell length, L, and the parameter β_1, whose correct values (L= 0.04 m; β_1= 3.34x10^4 Ω^{-1}m^{-1}) were obtained from[77]. More details on the model can be found in[56]. Solving the lumped SOFC model described by Eqs.(2.1), (2.2), (2.3) and (2.4) at steady state conditions leads to the results presented in Figures 2.1, 2.2 and 2.3 that show the existence of multiple steady states in the SOFC. In the case of potentiostatic and constant load operations, up to three steady states were found[56], while in the case of galvanostatic operation, one intersection point was found, which implied the presence of one single steady state in the system. As pointed out by Mangold et al.[56], the constant current fixes the reaction rates of the cell and thus reduces the nonlinear effects of the reaction kinetics.

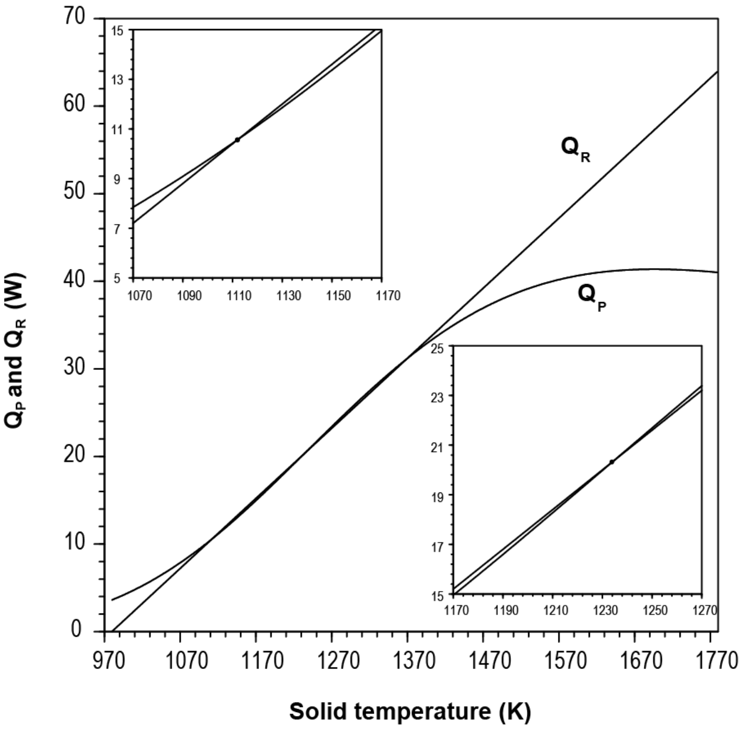

Figure 2.1. Steady-state heat generation (Q_P) and heat removal (Q_R) versus solid temperature at an external load resistance of 0.0065 Ω, based on the simple model in[56].

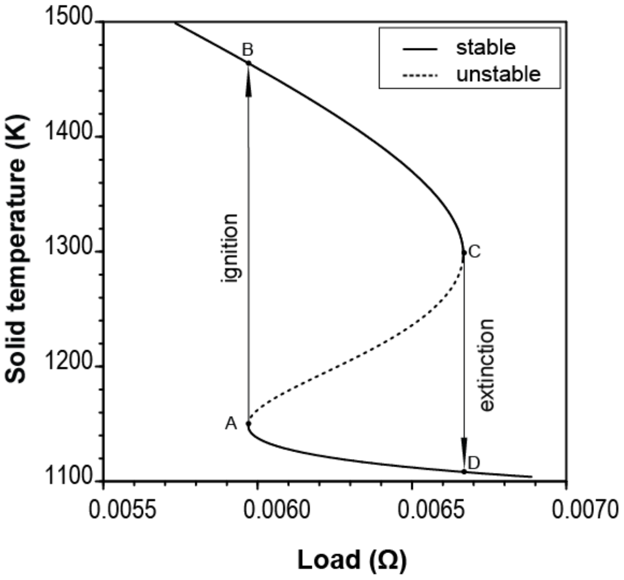

Figure 2.2. Bifurcation diagram (solid temperature versus load resistance), based on the simple model in[56].

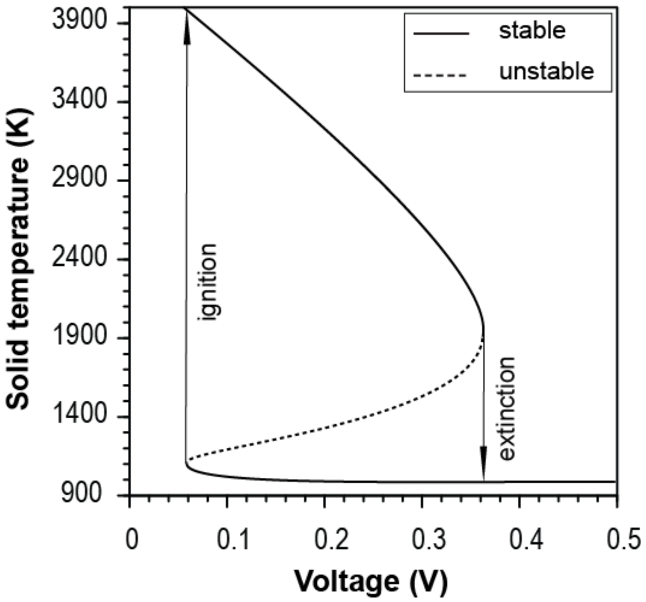

Figure 2.3. Bifurcation analysis (solid temperature versus cell voltage), based on the simple model in[56].

Figure 2.1 depicts a plot of heat generation and heat removal terms versus the solid temperature for an external load resistance of 0.0065 Ω, predicted by the model described by Eqs.(2.1)-(2.4). By solid, we mean the anode, cathode and electrolyte as a single unit. The points at which the heat removal and generation curves intersect represent the steady states corresponding to the external load level. As can be seen, there are three steady states (steady state temperatures) corresponding to the load level. When the load resistance is very small or very large, there is only one intersection (steady state). As in[56], one can also study the steady state multiplicity by varying the load resistance. Figure 2.2 depicts the steady-state solid temperature as the external load resistance varies. As can be seen in Figure 2.2, the temperature vs. load curve folds back on itself and thus gives rise to multiple values of the temperature for the resistive load levels approximately between 0.0059 to 0.0067 Ω.

Point A is the ignition point, and point C is the extinction point. Figure 2.3 depicts the steady state solid temperature as the cell outlet voltage varies. As can be seen, the temperatures on the upper branch are enormously high and outside the domain in which the model is valid[56]. Although the temperatures in the upper branch are not approachable in reality, the simulation result is indicative of potential instability and ignition-extinction phenomena in the steady state solution of the system.

The lumped model that Mangold et al.[56] used in their analysis was very simple, as their aim was to examine more the existence of multiple steady states and identify the cause of the multiplicity in the system. Unlike in PEMFCs, no experimental (actual) evidence of the multiplicity in SOFCs has been reported yet. Theoretical studies of the multiplicity in SOFCs using mathematical models that are less ideal (account for more practical issues) are steps towards an experimental validation of the multiplicity in a lab-, pilot-, or industrial-scale SOFC.

In this study, we consider a more detailed lumped model for analysis of multiplicity in a SOFC. This study is a step towards determining whether SOFC steady-state multiplicity truly exists in practical applications or not. The model considered herein accounts for several practical factors not accounted for in the lumped models used in these previous studies. These factors include: (i) non-identical inlet and outlet gas compositions in the anode and cathode channels, (ii) non-identical inlet and outlet temperatures in the anode and cathode channels, (iii) the dependence of the effective diffusion coefficient on the operating conditions such as solid temperature and partial pressures of gases, (iv) the temperature dependence of the physical properties of the gases, and (v) the concentration polarization, which has a strong effect on the fuel cell performance at high current densities.

2.3 Mathematical Modeling

The SOFC system under study is a single planar SOFC. Figure 2.4 shows the schematic of the SOFC. A dynamic model is developed using the approach similar to that presented in [10]. The fuel cell is divided into five subsystems: 1) a solid part which consists of the anode, cathode and electrolyte layers, 2) the diffusion layer inside the cathode side, 3) the gas channel on the cathode side, 4) the diffusion layer inside the anode side, and 5) the gas channel on the anode side. The following assumptions are made:

i. Temperature along the solid part (anode, cathode and electrolyte) structure is considered uniform, and the solid phase is considered as a one single subsystem.
ii. Each subsystem is locally homogeneous; each subsystem is considered as a stirred tank.
iii. Heat transfer coefficients for convection between (a) the anode and fuel stream and (b) the cathode and the air stream are constant.
iv. Heat transfer by radiation between the electrodes and the gases in the anode and cathode side channels is ignored.
v. All gases are ideal.

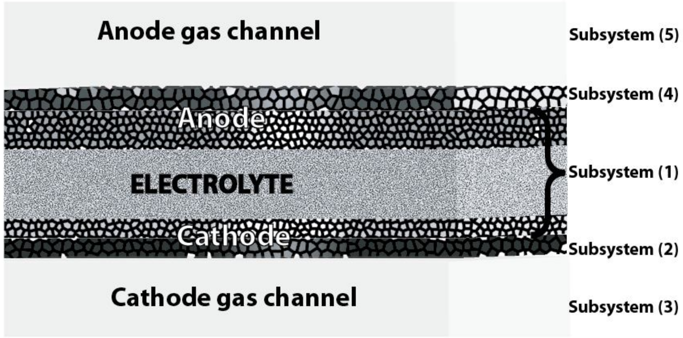

Figure 2.4. Planar SOFC divided into five subsystems.

For each of these subsystems, mass and energy conservation equations are written, leading to fourteen nonlinear equations (10 ordinary differential and 4 algebraic equations). The model parameter values listed in Table 2-1 are used. Specific heat capacity correlations used in this study are given in Table 2-2 [78].

Table 2-1. Parameter Values of the Detailed Model.

parameter	value	source
d_A	10^{-4} m	79
d_C	0.5×10^{-4} m	79
d_E	1.8×10^{-4} m	79
L	0.04 m	56
B	0.04 m	56
W	10^{-3} m	56
$\dot{n}_{\text{air,in}}^{\text{cat}}$	3.8×10^{-2} mol s^{-1}	56
$\dot{n}_{\text{fuel,in}}^{\text{an}}$	1.39×10^{-3} mol s^{-1}	56
$T_{\text{air,in}}^{\text{cat}}$	980 K-variable	56
$T_{\text{fuel,in}}^{\text{an}}$	980 K-variable	56
$v_{\text{fuel}}^{\text{an}}$	2.88 m s^{-1}	

$v_{\mathrm{air}}^{\mathrm{cat}}$	78.98 m s^{-1}	
$(\rho c_p)^s$	10^6 J $\mathrm{m}^{-3}\mathrm{K}^{-1}$	56
$\Delta_R H$	-241830 J mol^{-1}	56
γ^{A}	5.7×10^7 A m^{-2}	79
γ^{C}	7×10^9 A m^{-2}	79
θ_a^A	2	79
θ_c^A	1	79
θ_a^C	1.4	79
θ_c^C	0.6	79
β_1	3.34×10^4 $\Omega^{-1}\mathrm{m}^{-1}$	79
β_2	1.03×10^4 K	79
E^{A}	140000 J mol^{-1}	79
E^{C}	160000 J mol^{-1}	79
α	25 W $\mathrm{m}^{-2}\mathrm{K}^{-1}$-variable	56
Δ_{ano}	5×10^{-5} m	
Δ_{cat}	5×10^{-5} m	
$\varepsilon_{\mathrm{cat}}$	5×10^{-1}	32
$\varepsilon_{\mathrm{ano}}$	5×10^{-1}	32
τ_{ano}	3	32
τ_{cat}	3	32
δ_{ano}	5×10^{-7}	80
δ_{cat}	5×10^{-7}	80
υ_{H_2}	7.07	81
υ_{O_2}	16.6	81
υ_{N_2}	17.9	81
υ_{H_2O}	12.7	81

$y_{O_{2,\text{in}}}$	0.2	56
$y_{N_{2,\text{in}}}$	0.8	56
$y_{H_{2,\text{in}}}$	0.9	56
$y_{\text{H}_2\text{O}_\text{in}}$	0.1	56

Table 2-2. Specific heat capacities of the gas components[78].

	$C_p=a+bT+cT^2+dT^{-2}$		
component	H_2	O_2	H_2O
a	27.67	34.57	34.36
b	0.3386	0.1078	0.0627
c	0	0	0.56012
d	0	-784586	0

2.3.1 **Electrochemical Modeling**

Electrochemical reactions taking place inside a SOFC when hydrogen is used as a fuel are [82] :

Oxidation reaction at the anode side:

$$H_2 + O^{2-} \rightarrow H_2O + 2e^-$$

Reduction reaction at the cathode side:

$$\frac{1}{2}O_2 + 2e^- \rightarrow O^{2-}$$

So, the overall reaction is:

$$\frac{1}{2}O_2 + H_2 \rightarrow H_2O$$

Rates of hydrogen consumption, oxygen consumption and water production are directly calculated from the cell current using Faraday's law:

$$R_{H_2} = \left(\frac{1}{2F} \right) I \tag{2.6}$$

$$R_{O_2} = \left(\frac{1}{4F} \right) I \tag{2.7}$$

$$R_{H_2O} = \left(\frac{1}{2F} \right) I \tag{2.8}$$

The reversible cell voltage is calculated by using the Nernst equation:

$$U_0 = E^0 - \frac{RT_S}{nF} ln \left(\frac{p_{H_2O}^{bulk}}{p_{H_2}^{bulk} \, p_{O_2}^{bulk^{0.5}}} \right) \tag{2.9}$$

The actual cell output voltage is lower than the voltage from the Nernst potential (Eq.2.9) because of three potential drops/losses, ohmic polarization, concentration polarization, and activation polarizations. These losses should be subtracted from the reversible cell voltage to obtain the actual cell outlet voltage:

$$U_{cell} = U_0 - \eta_{an} - \eta_{cath} - \rho_E \, d_E \, i - \eta_{conc} \tag{2.10}$$

where η_{an} and η_{cath} represent the anode and cathode activation polarizations, respectively. They are described by Butler-Volmer equation for the anode and cathode sides[56]:

$$\frac{I}{LB} = \gamma^A p_{H_2}^{TPB} p_{H_2O}^{TPB} \exp\left(\frac{-E^A}{RT_S} \right) \left\{ \exp\left(\theta_a^A \frac{F}{RT_S} \eta_{an} \right) - \exp\left(-\theta_c^A \frac{F}{RT_S} \eta_{an} \right) \right\} \tag{2.11}$$

$$\frac{I}{LB} = \gamma^C p_{O_2}^{TPB^{0.25}} \exp\left(\frac{-E^C}{RT_S} \right) \left\{ \exp\left(\theta_a^C \frac{F}{RT_S} \eta_{cath} \right) - \exp\left(-\theta_c^C \frac{F}{RT_S} \eta_{cath} \right) \right\} \tag{2.12}$$

The activation overvoltages (polarizations) represent the voltage needed to overcome the activation energies of electrochemical reactions occurring in the triple phase boundary zone (TPB) [83].

The fourth term in the right hand side of the Eq.2.10, $\rho_E\ d_E\ i$, is related to ohmic losses. Ohmic losses are mainly due to ionic resistance of electrolyte rather than the electrical resistance in the electrodes. Electrical conductivity of the electrolyte is described as an Arrhenius type correlation, dependent on temperature [79]:

$$\rho_E = \frac{1}{\beta_1} \exp\left(\frac{\beta_2}{T_S}\right) \tag{2.13}$$

To account for the concentration polarization, the following correlation is used [54] :

$$\eta_{conc} = \frac{RT}{nF} ln\left(\frac{p_{H_2}^{bulk}\ {p_{O_2}^{bulk}}^{0.5}}{p_{H_2O}^{bulk}}\right) - \frac{RT}{nF} ln\left(\frac{p_{H_2}^{TPB}\ {p_{O_2}^{TPB}}^{0.5}}{p_{H_2O}^{TPB}}\right) \tag{2.14}$$

which is indeed the difference between two reversible cell voltages, one calculated based on bulk partial pressures of species and the other calculated based on partial pressures of species at the triple phase boundary.

2.3.2 **Model Equations for Subsystem 1**

Subsystem 1 is the solid phase of the cell, which consists of the anode layer, the cathode layer, and the electrolyte layer between them. Heat is transferred between the solid and gas streams in the anode and cathode gas channels by convection heat transfer. Heat generated in the cell is the difference between the heat released by the electrochemical reaction and the electric power supplied to the external load. An energy balance for this subsystem yields:

$$\left(d_A+d_E+d_C\right)\rho_S C_{p_S}\,\frac{dT_S}{dt}=\Delta H_R-U_{cell}\,\frac{I}{LB}+\alpha\left(T_{fuel}^{an}-T_S\right)+\alpha(T_{air}^{cath}-T_S\,)\quad(2.15)$$

where

$$\Delta H_R = N_{o_2}H_{o_2}^{cath}+N_{H_2}H_{H_2}^{an}-N_{H_2o}H_{H_2o}^{an}$$

2.3.3 Model Equations for Subsystem 2

This subsystem embodies the diffusion layer in the cathode side of the fuel cell. A mole balance on oxygen inside the cathode-side diffusion layer leads to:

$$\frac{\Delta_{cath}}{R}\frac{d}{dt}\left(\frac{p_{O_2}^{TPB}}{T_S}\right)=N_{O_2}-\frac{1}{LB}R_{O_2}\qquad(2.16)$$

where R_{O_2} is the molar rate of consumption of oxygen, described in section 2.3.1, and N_{O_2} is the molar flux of oxygen transferred from the cathode side channel into this layer. The mass flux of the diffusing oxygen can be defined in terms of the mass transfer coefficient by

$$N_{O_2}=k_{O_2}^{cath}\left(c_{air}^{cath}y_{O_2}^{cath}-\frac{p_{O_2}^{TPB}}{RT_S}\right)\qquad(2.17)$$

where $k_{O_2}^{\mathrm{cat}}$ is the mass transfer coefficient, is given by

$$k_{O_2}^{cath}=\frac{D_{e_{O_2}}}{\Delta_{\mathrm{cath}}}=\frac{\varepsilon_{cath}}{\tau_{cath}\Delta_{cath}}D_{O_2}\qquad(2.18)$$

$D_{e_{O_2}}$ is the effective diffusion coefficient, $\varepsilon_{\mathrm{cath}}$ and τ_{cath} are respectively the porosity and tortuosity of the cathode porous materials, Δ_{cath} is the thickness of the cathode diffusion layer, and D_{O_2} is the total diffusion coefficient which includes Knudsen and molecular combined diffusion given by [81].

$$\frac{1}{D_{O_2}} = \frac{1}{D_{O2N2}} + \frac{1}{D_{K_{O_2}}} \tag{2.19}$$

The binary diffusion coefficient of oxygen in nitrogen is calculated using the Fuller correlation

$$D_{O_2N_2} = \frac{1.013*10^{-7} {T_S}^{1.75} \left(\frac{1}{M_{O_2}} + \frac{1}{M_{N_2}} \right)^{0.5}}{\left[p_{O_2}^{TPB} + p_{air}^{cath} \left(1 - y_{O_2}^{cath} \right) \right] \left[{\upsilon_{O_2}}^{\frac{1}{3}} + {\upsilon_{N_2}}^{\frac{1}{3}} \right]^2} \tag{2.20}$$

The Knudsen diffusion coefficient given by [80]:

$$D_{K_{O_2}} = 97 \delta_{cath} \sqrt{\frac{T_S}{M_{O_2}}} \tag{2.21}$$

is used. This correlation is suitable for straight and round pores.

2.3.4 **Model Equations for Subsystem 3**

This subsystem is the cathode gas channel in which air flows through. The dynamics of this subsystem are described by the following three equations obtained from a mole balance on air, a mole balance on oxygen and an energy balance for the subsystem:

$$LBW \frac{dc_{air}^{cath}}{dt} = \dot{n}_{air,in}^{cath} - v_{air}^{cath} c_{air}^{cath} WB - N_{o_2} LB \tag{2.22}$$

$$LBW \frac{d(c_{air}^{cath} y_{o_2}^{cath})}{dt} = \dot{n}_{air,in}^{cath} y_{o_{2,in}} - v_{air}^{cath} c_{air}^{cath} y_{o_2}^{cath} WB - N_{o_2} LB \tag{2.23}$$

$$\begin{gathered} LBW \frac{d(c_{air}^{cath} c_{pair}^{\ cath} T_{air}^{cath})}{dt} = \\ \dot{n}_{air,in}^{cath} H_{air,in}^{cath} - v_{air}^{cath} c_{air}^{cath} H_{air}^{cath} BW + \alpha \left(T_S - T_{air}^{cath} \right) LB - N_{o_2} H_{o_2}^{cath} LB \end{gathered} \tag{2.24}$$

The first term from the right in Eq.(2.24) accounts for energy leaving the subsystem with the oxygen that diffuses into the cathode layer .

2.3.5 **Model Equations for Subsystem 4**

This subsystem represents the diffusion layer in the anode side of the fuel cell. The mole balances on the two species present in this layer, hydrogen and water, are as follows:

$$\frac{\Delta_{an}}{R}\frac{d}{dt}\left(\frac{p_{H_2O}^{TPB}}{T_S}\right) = -N_{H_2o} + \frac{1}{LB}R_{H_2o} \tag{2.25}$$

$$\frac{\Delta_{an}}{R}\frac{d}{dt}\left(\frac{p_{H_2}^{TPB}}{T_S}\right) = N_{H_2} - \frac{1}{LB}R_{H_2} \tag{2.26}$$

where R_{H_2} and R_{H_2O} are the molar rate of hydrogen consumption and water production, described in Section 2.3.1. N_{H_2} and N_{H_2o} are molar fluxes of hydrogen flowing out and water flowing into this layer, respectively. These two fluxes are given by:

$$N_{H_2} = k_{H_2}^{an}\left(c_{fuel}^{an} y_{H_2}^{an} - \frac{p_{H_2}^{TPB}}{RT_S}\right) \tag{2.27}$$

$$N_{H_2O} = k_{H_2O}^{an}\left(\frac{p_{H_2O}^{TPB}}{RT_S} - c_{fuel}^{an} y_{H_2O}^{an}\right) \tag{2.28}$$

The mass transfer coefficients of water and hydrogen are given by:

$$k_{H_2}^{an} = \frac{D_{e_{H_2}}}{\Delta_{\mathrm{an}}} = \frac{\varepsilon_{an}}{\tau_{an}\Delta_{an}} D_{H_2} \tag{2.29}$$

$$k_{H_2O}^{an} = \frac{D_{e_{H_2O}}}{\Delta_{\mathrm{an}}} = \frac{\varepsilon_{an}}{\tau_{an}\Delta_{an}} D_{H_2O} \tag{2.30}$$

where ε_{an} and τ_{an} are the porosity and tortuosity of the anode porous materials; and D_{H_2} and D_{H_2O} are the total diffusion coefficients of hydrogen and water, respectively, calculated from:

$$\frac{1}{D_{H_2}} = \frac{1}{D_{H_2H_2O}} + \frac{1}{D_{K_{H_2}}} \tag{2.31}$$

$$\frac{1}{D_{H_2O}} = \frac{1}{D_{H_2OH_2}} + \frac{1}{D_{K_{H_2O}}} \tag{2.32}$$

where

$$D_{K_{H_2}} = 97\,\delta_{an}\sqrt{\frac{T_S}{M_{H_2}}}$$

$$D_{K_{H_2O}} = 97\,\delta_{an}\sqrt{\frac{T_S}{M_{H_2O}}}$$

The binary diffusion coefficient of hydrogen in water, $\mathrm{D}_{H_2H_2O}$, is equal to water in hydrogen $D_{H_2OH_2}$ and can be calculated using the Fuller equation:

$$D_{H_2H_2O} = \frac{1.013*10^{-7}{T_S}^{1.75}\left[\frac{1}{M_{H_2}} + \frac{1}{M_{H_2O}}\right]^{0.5}}{\left(p_{H_2O}^{TPB} + p_{H_2}^{TPB}\right)\left({\upsilon_{H_2}}^{\frac{1}{3}} + {\upsilon_{H_2O}}^{\frac{1}{3}}\right)^2} \tag{2.33}$$

2.3.6 Model Equations for Subsystem 5

This subsystem is the anode-side channel gas including hydrogen and water. A total mole balance on the fuel, a mole balance on hydrogen, and an energy balance for the subsystem yield:

$$LBW\frac{dc_{fuel}^{an}}{dt} = \dot{n}_{fuel,in}^{an} - v_{fuel}^{an}c_{fuel}^{an}WB + (N_{H_2O} - N_{H_2})LB \tag{2.34}$$

$$LBW\,\frac{d(c^{an}_{fuel}y^{an}_{H_2})}{dt}=\dot{n}^{an}_{fuel,in}y_{H_{2,in}}-v^{an}_{fuel}c^{an}_{fuel}y^{an}_{H_2}WB-N_{H_2}LB \qquad (2.35)$$

$$LBW\,\frac{d(c^{an}_{fuel}c^{\;an}_{p\,fuel}T^{an}_{fuel})}{dt}= \qquad (2.36)$$
$$\dot{n}^{an}_{fuel,in}H^{an}_{fuel,in}-v^{an}_{fuel}c^{an}_{fuel}H^{an}_{fuel}BW+\alpha\left(T_S\;-T^{an}_{fuel}\right)LB+(N_{H_2o}H^{an}_{H_2o}-N_{H_2}H^{an}_{H_2})LB$$

2.4 Numerical Method

The fuel cell model described in Section 2 consists of fourteen nonlinear equations; ten ordinary differential equations (ODEs) and four nonlinear algebraic equations. Coupling among mass transfer, heat transfer, cell current and outlet voltage resulted in a set of nonlinear differential and algebraic equations, which should be solved simultaneously.

The model at steady state conditions reduces to fourteen algebraic equations, which are solved to calculate the steady state values of $p^{\mathrm{TPB}}_{O_2}$, $c^{\mathrm{cath}}_{\mathrm{air}}$, $y^{\mathrm{cath}}_{o_2}$, $T^{\mathrm{cath}}_{\mathrm{air}}$, $p^{\mathrm{TPB}}_{H_2O}$, $p^{\mathrm{TPB}}_{H_2}$, $c^{\mathrm{an}}_{\mathrm{fuel}}$, $y^{\mathrm{an}}_{H_2}$, $T^{\mathrm{an}}_{\mathrm{fuel}}$, I, V, η_{an}, η_{cath} and T_S for a given value of R_{load}. In the case of a constant ohmic load, load resistance (R_{load}) is selected as the bifurcation parameter. For a given load resistance, multiple steady state values may exist for the solid temperature (T_S). Thus, if we set the value of the load resistance, a numerical root-finding method finds the steady-state solid temperature that is closest to the initial guess used. On the other hand, for a given solid temperature (T_S), one load resistance (R_{load}) always exists. Therefore, if we set the value of T_S, rather than R_{load}, one suitable initial guess will be adequate. Furthermore, as the dependence of the cell behavior on the solid temperature is highly nonlinear, by setting the temperature and solving for the remaining variables one eliminates the most severe nonlinearity from the system of algebraic equations. The MATLAB routine `fsolve` is used to solve this set of nonlinear algebraic equations. After a solution is obtained for a specific value of the solid temperature, for the next value of the solid temperature, the initial guess vector is chosen to be the root corresponding to the previous value of the solid temperature. This approach reduces the convergence time and the number of numerical errors. To pinpoint the ignition and extinction points and locate the limiting boundaries of multiple steady state region, one needs to search for minimum and maximum values of R_{load} versus T_S and the outlet voltage versus T_S in the cases of constant ohmic load and potentistatic modes, respectively.

To simulate the dynamic response of the system, the model presented in Section 3 is integrated numerically. The dynamic model, which is in the form of a set of differential and nonlinear algebraic equations, is highly nonlinear, complex and stiff. The MATLAB routine ode15s is used for obtaining the solution of differential algebraic equations (DAEs). Ode15s is suitable for stiff ordinary differential equations (ODEs) of the form[84]:

$$M(t)y' = f(t,y)$$

When the mass matrix, M(t), is singular, the system is described by DAEs than ODEs. In this study, we have ten ODEs and three algebraic equations. Thus, M is a 13x13 identity matrix whose last three rows were replaced with zeros.

2.5 Steady State Analysis

To find the number of steady state solutions, one approach is to calculate and plot the heat generation and heat removal in the system versus the solid temperature, as is customary in studying steady-state multiplicity in chemical reactors. From energy balance Eq. (2.15), heat generation (Q_P) and heat removal (Q_R) are defined as [56]:

$$Q_P = \Delta H_R - U_{cell} \frac{I}{LB} \tag{2.37}$$

$$Q_R = 2\alpha T_S - \alpha(T_{fuel}^{an} + T_{air}^{cath}) \tag{2.38}$$

Heat generation and heat removal are equal at a steady state. Heat removal is by convection heat transfer and increases linearly with the solid temperature, while the heat generation increases sigmoidally. The steady state analysis are conducted for three modes of operation, as in[56]; the fuel cell is operated at constant external load resistance, under potentiostatic control and under galvanostatic control.

2.5.1 Constant Ohmic Load Operation

Under constant ohmic load operation, the ohm's law is used to describe the cell voltage and current relation:

$$U_{cell} = R_{Load} I$$

Figure 2.5 depicts the heat generation and heat removal terms versus the solid temperature using conditions identical to those in[56]; i.e., conditions used to generate the results shown in Figure 2.2. The inlet cathode and anode channel gas temperatures are 980 K. As can be seen, Q_P curve intersects Q_R line at one point only, contrary to three points in Figure 2.2. To investigate whether this fuel cell exhibits multiple steady states in other ranges of external load resistance, we conduct a bifurcation analysis of solid temperature versus load resistance. Figure 2.6(a) shows the simulation results obtained by varying the solid temperature. Load resistance is chosen as the bifurcation parameter. It can be seen that there is a monotonic relationship between solid temperature and load resistance, showing the existence of a unique stable steady state, while multiple steady states were observed in the range of 0.0059 to 0.0067 Ω in Figure 2.2. Figure 2.6(b) depicts heat removal and heat generation curves, which indicates the existence of a unique steady state for the load resistance of 0.0112 Ω.

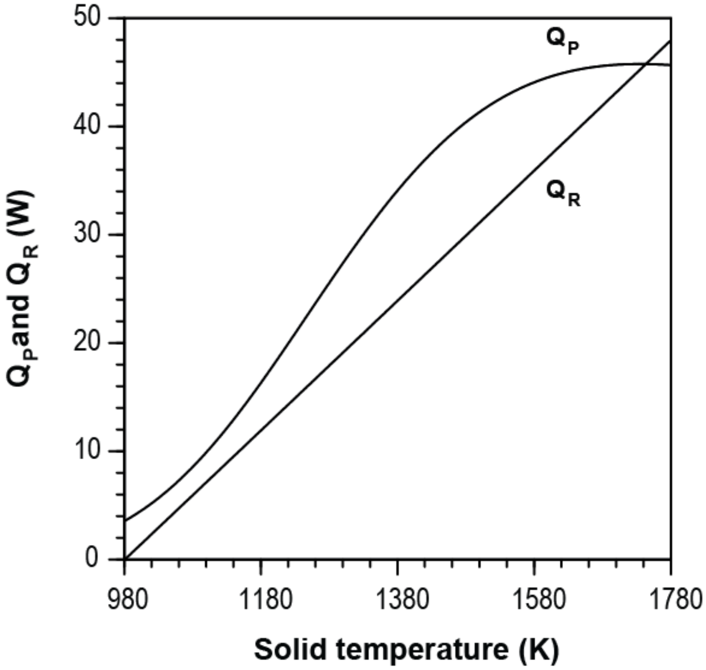

Figure 2.5. Steady-state heat generation (Q_P) and heat removal (Q_R) versus solid temperature at an external load resistance of 0.0065 Ω, based on the more detailed model.

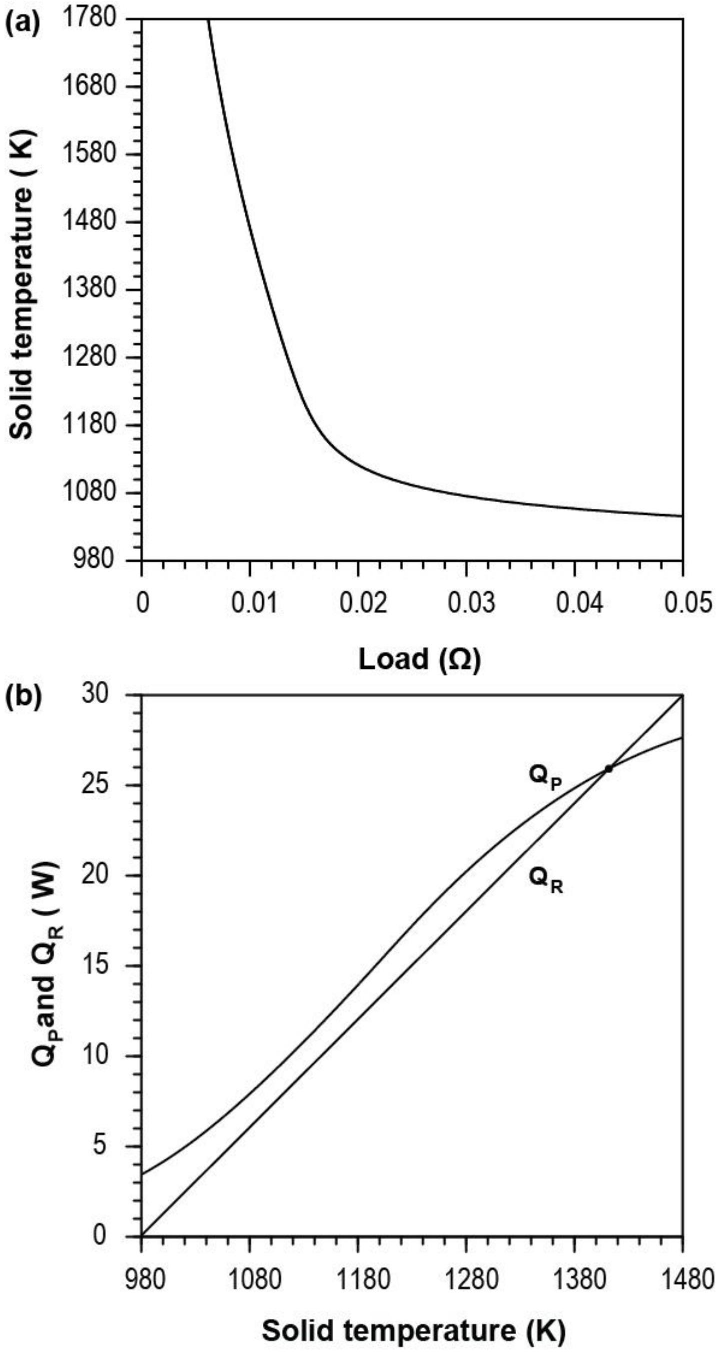

Figure 2.6. Steady state behavior under inlet gas channel temperatures of 980 K, based on the more detailed model: (a) Steady-state heat generation (Q_P) and heat removal (Q_R) versus solid temperature at an external load resistance of 0.0112 Ω; (b) steady state analysis of the detailed model (solid temperature versus load resistance).

To investigate the existence of multiple steady states in other ranges of operating conditions, we carry out a bifurcation analysis at lower values of inlet air and fuel temperatures. Figure 2.7(a) depicts heat generation and heat removal curves versus the solid temperature for an external load resistance of 0.0112 Ω. As can be seen, there are three steady states (steady state temperatures) corresponding to this load level. The middle steady state, as expected, is unstable. The corresponding T^S-R_{Load} plot is shown in Figure 2.7(b). A comparison of the bifurcation diagrams of the detailed model and the simple model, depicted in Figures 2.7(b) and 2.2, shows that in the case of the detailed model, the hysteresis loop moves toward higher values of external load resistance and the region of hysteresis loop is shrunk slightly, but the multiplicities are similar qualitatively. Figure 2.7(b) shows that for a load resistance between 0.011 to 0.0114 Ω, there is more than one value for solid temperature. It also indicates that this system exhibits hysteresis behavior, which involves two-saddle node bifurcations. If the cell is operated under a load resistance in this range, and the load resistance is then gradually lowered, the steady state moves towards point A, which is an ignition point. At this point, with a small further decrease in the load resistance, the temperature jumps to point B on the upper branch. As the load is increased at this point, the cell moves towards operating at point C, which is an extinction point. With a small further increase, the temperature drops sharply to the lower curve. Points A and C represent the boundaries of the hysteresis loop.

Figures 2.8(a) and 2.8(b) show that at steady state, the cathode and anode exit gas temperatures increase linearly with the solid temperature. However, the change in the anode exit gas temperature is higher compared to that in the cathode exit gas temperature. Figure 2.9 shows that the mole fractions of the reactants and product, especially those of hydrogen and water, at the triple phase boundary are not constant and change with the solid temperature. The significantly less dependence of oxygen mole fraction on the solid temperature is due to the much higher flow rate of air compared to that of the fuel.

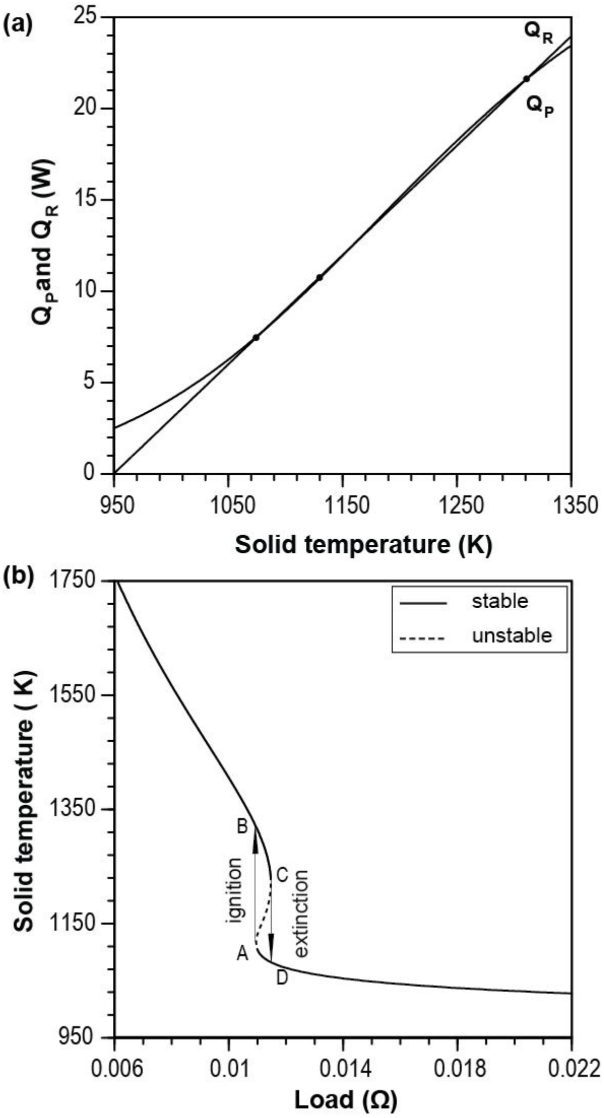

Figure 2.7. Steady state behavior under inlet gas channel temperatures of 950 K, based on the more detailed model: (a) Steady-state heat generation (Q_P) and heat removal (Q_R) versus solid temperature at an external load resistance of 0.0112 Ω; (b) Bifurcation analysis of the detailed model (solid temperature versus load resistance).

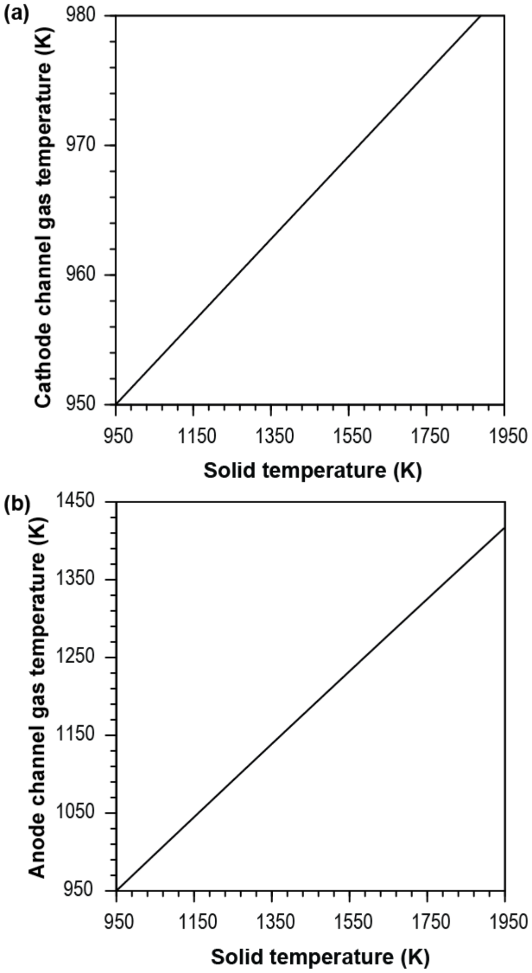

Figure 2.8. Variations in cathode and anode gas inlet temperature, based on the more detailed model: (a) cathode gas inlet temperature versus solid temperature; (b) anode gas inlet temperature versus solid temperature.

We also investigate the effect of heat convection coefficient on the multiplicity region of the SOFC under constant ohmic load operation. The shaded areas in Figure 2.10 show the regions of the inlet cathode and anode channel gas temperatures and the load resistance, within which the multiplicity exists, for different values of the heat transfer coefficient (α). As can be seen, the shape of this region is qualitatively similar at different values of the heat transfer coefficient. As the coefficient increases, the multiplicity region shifts towards lower values of the load resistance. This behavior is expected from the fuel cell: as the heat transfer coefficient increases, the rate of heat dissipation increases, and thus to operate the cell at the same steady-state solid temperature, the electrochemical reactions have to release more thermal energy. The higher rate of heat generation by the electrochemical reactions is possible at a higher current, which corresponds to a lower load resistance. Figure 2.10 also shows that for a given heat transfer coefficient and given inlet gas temperatures, there are a pair of turning points (saddle node bifurcation points). At higher heat transfer coefficients, these turning points exist at lower load resistances. Also, the distance between each pair of the turning points decreases, as the load resistance increases. An explanation for this cell behavior is as follows. As the anode and cathode inlet gas temperatures increase, less energy is removed from the cell by convection (flowing gases). Therefore, at steady state conditions, less energy should be released by the electrochemical reactions. The lower rate of heat release calls for a lower current, which can be attained at a higher load resistance. Thus, the inverse S-shaped curve generally shifts toward the higher values of load resistance. A three-dimensional plot of the solid temperature versus R_{Load} as a function of the inlet channel gas temperatures is illustrated in Figure 2.11. At low gas channel temperatures, there are multiple steady states (solid temperatures), but at high channel gas temperatures, there is a unique steady state.

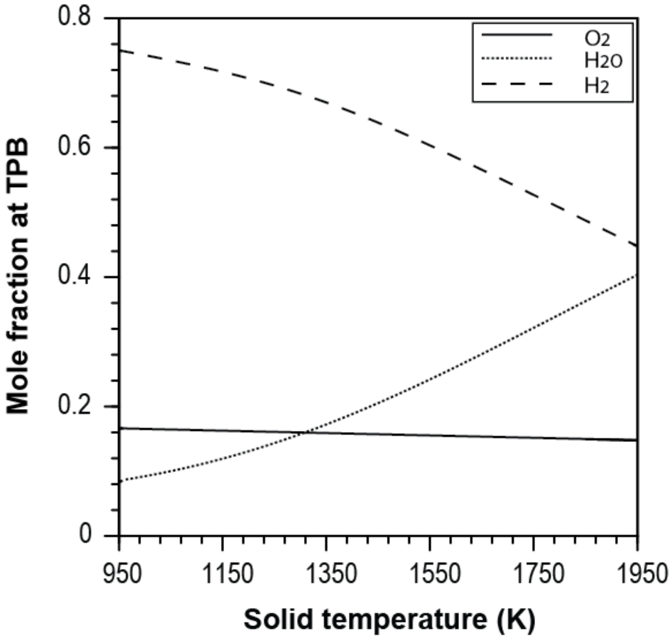

Figure 2.9. Variations in mole fraction of reactants and product species at the triple phase boundary zone, based on the more detailed model.

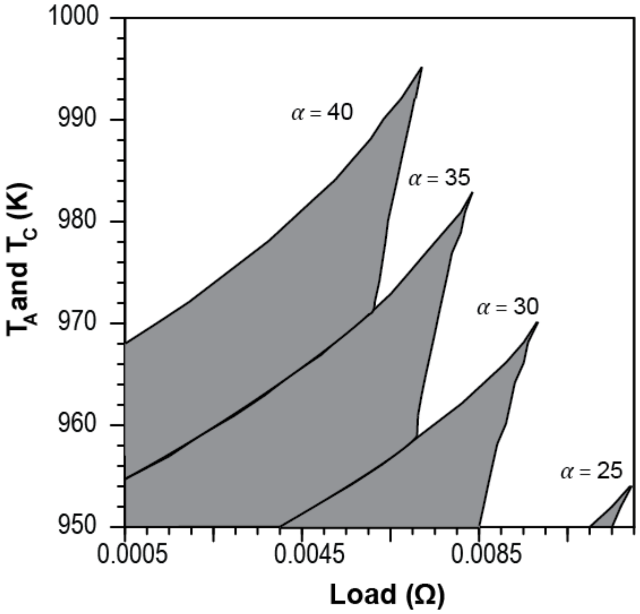

Figure 2.10. Multiplicity region for different heat convection coefficients in the constant ohmic load operation, based on the more detailed model.

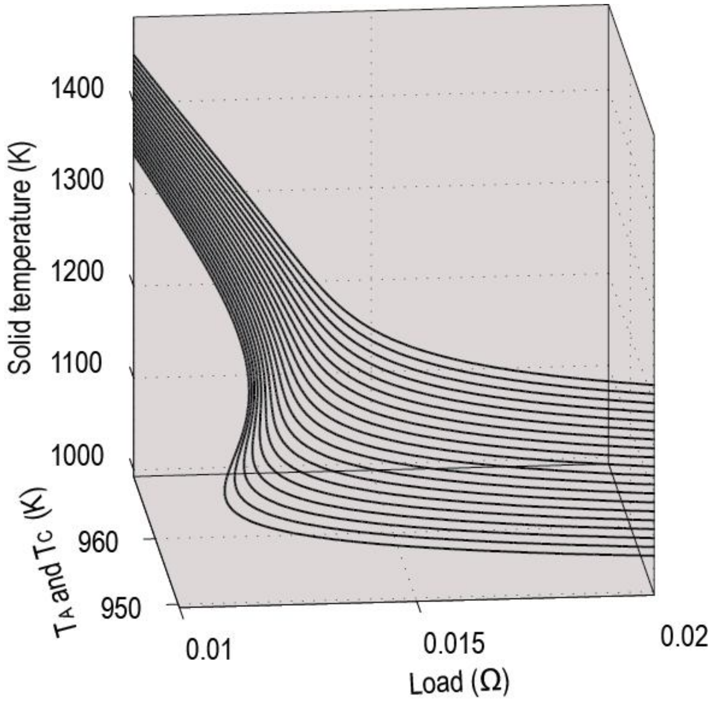

Figure 2.11. Solid temperature versus load resistance as inlet gas temperatures vary, based on the more detailed model.

The effect of the inlet fuel and air velocities is shown in Figure 2.12. As can be seen, the cell shifts from multiple steady states to a unique steady state as the inlet velocities decrease (A: twice the nominal values given in Table 2-1; B: the nominal values; C: half of the nominal values). The transition shown in this figure involved an increase in the load resistance from A to C due to the decrease in the velocity of the gas streams. The decrease in velocities increases the anode and cathode channel gas temperatures and hence decreases the heat dissipation by convection. Thus, the load resistance should increase to compensate for the decrease in the amount of heat dissipation. We also investigate independently the effects of the inlet fuel and air flow rates on the steady state multiplicity. Figure 2.13 is a three-dimensional plot of solid temperature versus load resistance and the inlet fuel flow rate. As can be seen, the range of the load resistance within which the multiplicity exists widens as the inlet fuel flow rate increases, and the inverse S-shaped curve moves toward lower values of the load resistance. Figure 2.14 shows the effect of the inlet air flow rate on the solid temperature-load resistance relationship. An increase in the air flow rate moves the inverse S-shapd curve towards the lower values of the load resistance very slightly. One can conclude that the inlet fuel flow rate has more influence in the multiplicity region than the inlet air flow rate does.

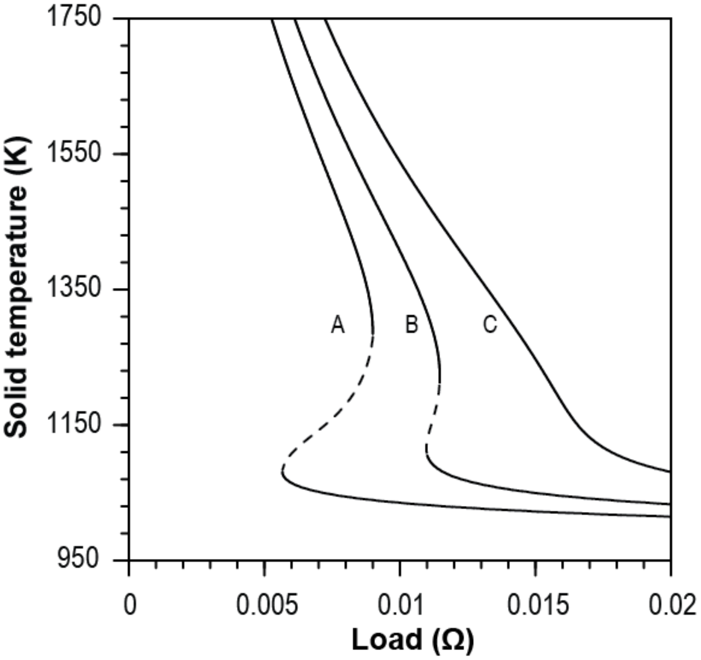

Figure 2.12. Solid temperature versus load resistance for different fuel and air velocities, based on the more detailed model (A: v_{air}^{cat} =157.96 m.s^{-1}, v_{fuel}^{an} = 5.76 m.s^{-1} B: v_{air}^{cat} =78.98 m.s^{-1}, v_{fuel}^{an} = 2.88 m.s^{-1} ;C: v_{air}^{cat} =39.49 m.s^{-1}, v_{fuel}^{an} = 1.44 m.s^{-1}).

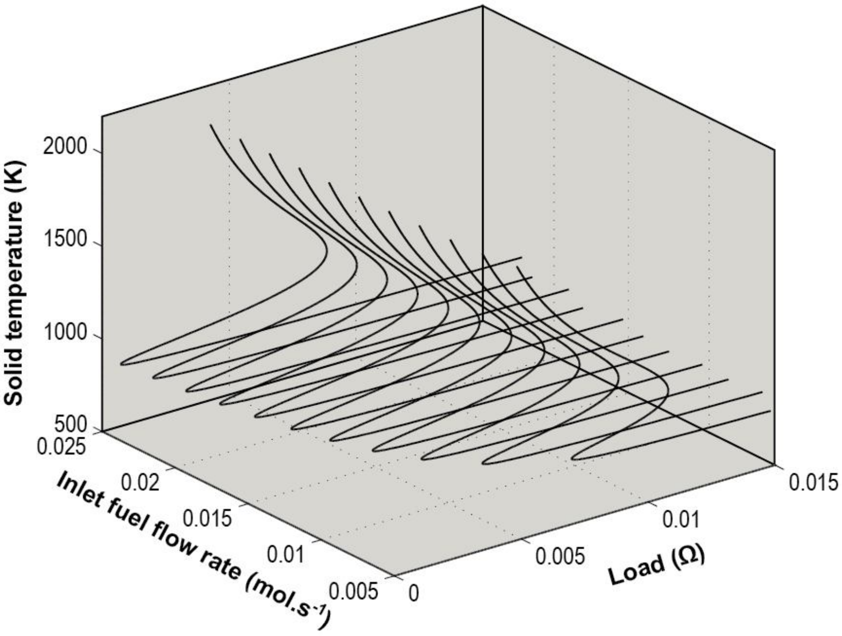

Figure 2.13. Solid temperature versus load resistance as inlet fuel flow rate varies, based on the more detailed model.

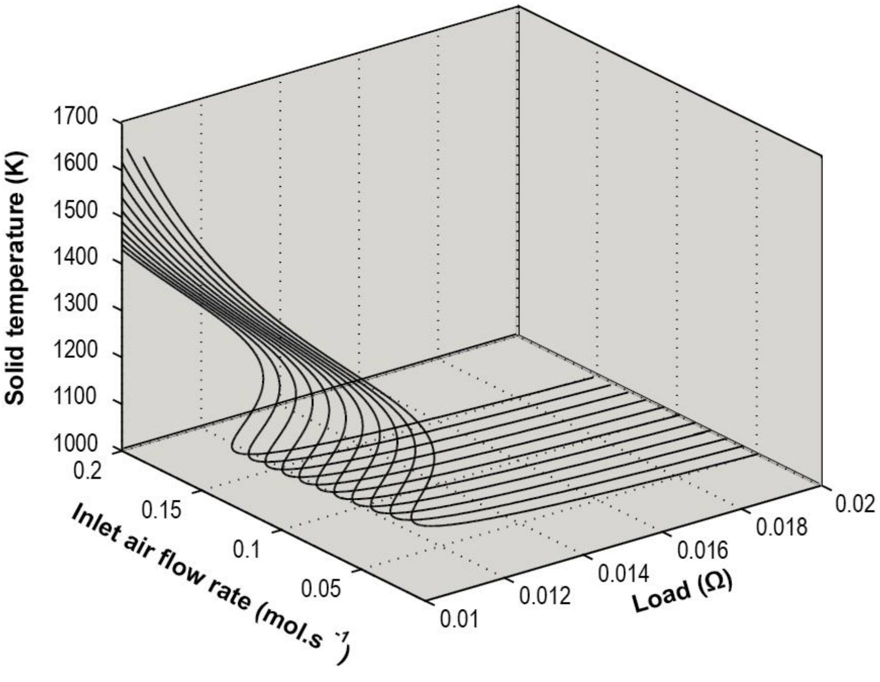

Figure 2.14. Solid temperature versus load resistance as inlet air flow rate varies, based on the more detailed model.

2.5.2 **Potentiostatic Operation**

The steady state multiplicity is also studied under potentiostatic mode (constant voltage). This mode of operation requires voltage control and is used to characterize a cell. In this case, the cell voltage is the bifurcation parameter. Figure 2.15 shows the bifurcation diagram drawn by plotting the steady state values of the solid temperature as a function of cell voltage at a channel gas temperature equal to 950 and 980 K. One can observe that more than one steady state exist in certain potential regimes. The middle one of the three steady states is unstable. The higher channel gas temperature (980 K) shifts the inverse S-shaped curve to higher values of the cell potential; this can be explained as follows. At a constant solid temperature, as the inlet gas temperatures increase, the rate of heat removal (by convection) from the cell decreases. This decrease in the rate of heat removal, at steady state conditions, leads to a decrease in the rate of heat production by the electrochemical reactions, and therefore the rate of the electrochemical reactions. The lower reaction rate is accompanied with a lower current and thus a higher cell voltage.

A comparison of Figures 2.15 and 2.3 shows that the behavior described by the detailed model is qualitatively similar to that described by the simple model of Mangold et al.[56]. However, we can observe quantitatively that the inverse S-shaped curve has shifted to higher values of cell voltage. Also, the upper curve (ignition curve) is at lower values of the solid temperature. We should note that the upper curve is beyond the limit of validity of the model, but the simulation results indicate hysteresis behavior and instability in the system under potentiostatic control.

Figure 2.16 shows the multiplicity region corresponding to channel gas temperature. The values of cell voltage on the boundaries (saddle node bifurcations) are found at different values of the inlet channel gas temperatures to determine the multiple steady state region. The dependence of multiplicity region on the heat convection coefficient is also shown. Similar to constant ohmic load operation, we can observe that the multiplicity region shifts toward lower values of the cell voltage. As the heat convection coefficient increases, heat dissipation increases and the solid temperature decreases, which in turn lowers the cell voltage.

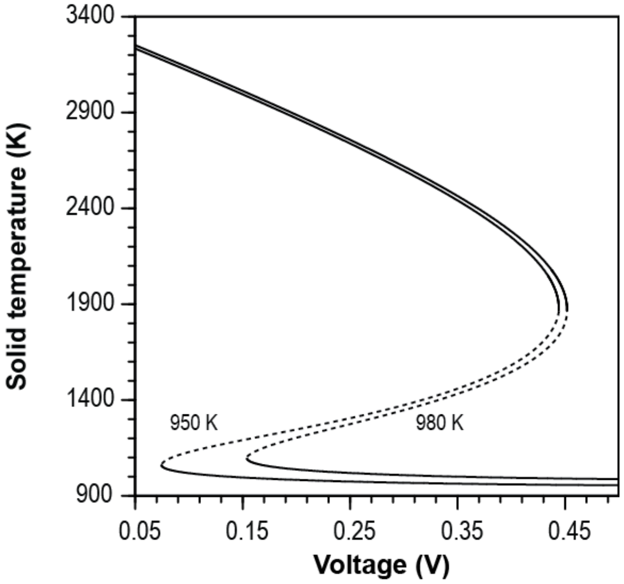

Figure 2.15. Bifurcation analysis potentiostatic control (solid temperature versus cell voltage), based on the more detailed model.

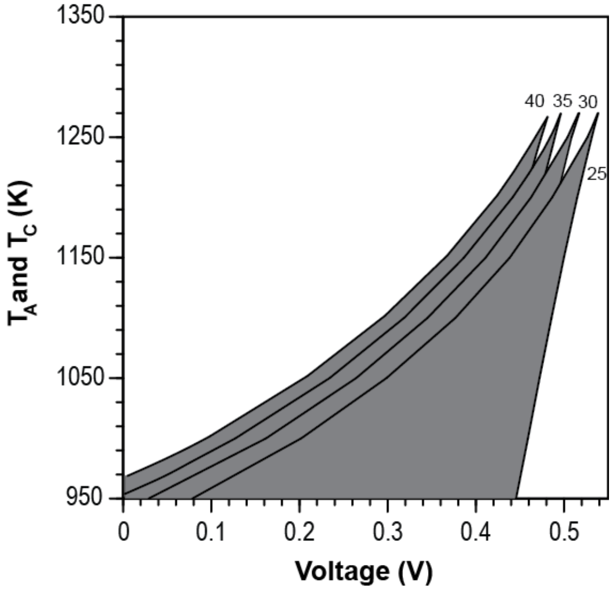

Figure 2.16. Multiplicity region for different heat convection coefficient values in the potentiostatic mode, based on the more detailed model.

2.5.3 **Galvanostatic Operation**

In the galvanostatic case, the current is kept constant. This type of operation is conducted under control and is used to characterize a cell. In this case, the free parameter is the cell current. The simulation results revealed a unique steady state in all operation conditions, similar to those of Mangold et al.[56]. Figure 2.17 shows the solid temperature versus the cell current. As can be seen, the dependence of the solid temperature on the cell current is monotonic, and at each current there is only one steady state corresponding to the solid temperature of the cell.

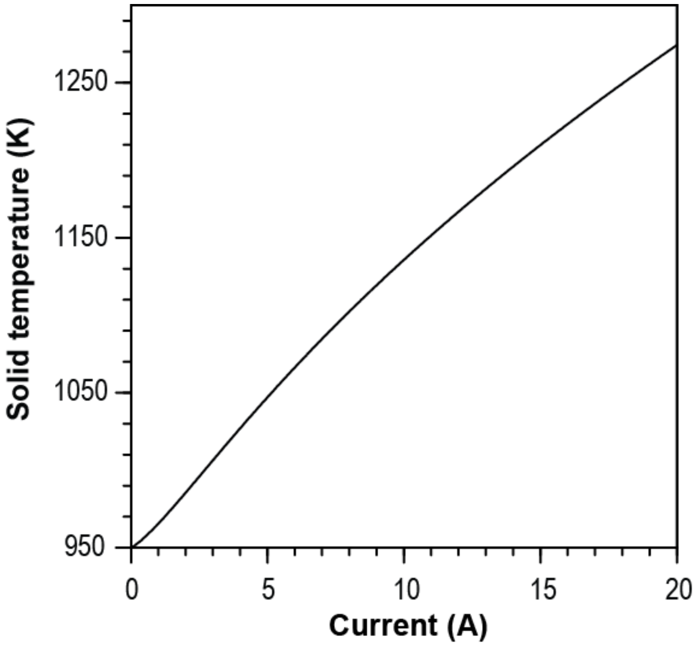

Figure 2.17. Solid temperature versus current under galvanostic operation mode, based on the more detailed model.

2.6 Dynamic Behavior

A SOFC is usually operated under varying load conditions. We study the dynamic behavior of the cell with the same parameter values used in the steady state study. Figure 2.18 shows the transient response of the fuel cell to a step change in the load resistance from 0.014 to 0.01Ω; it depicts how the solid temperature, current, voltage, and hydrogen, water and oxygen concentrations at the triple phase boundary vary with time. As Figure 2.7 shows, a slight change in the external load resistance moves the system from the extinction branch (lower curve) to the ignition branch (upper curve). The solid temperature response shows that the temperature jumps from 1053 to 1405 K, which is in agreement with the results in Figure 2.7. As the solid temperature jumps to the upper branch, the cell current increases and so does the rates of hydrogen and water consumptions, leading to a decrease in hydrogen and water concentrations at the triple phase boundary. Simultaneously, the rate of water production increases, leading to higher water concentration at the boundary. Interestingly, one can observe that the current and voltage responses to the step change in the load resistance are similar; that is, both variables increase with a step decrease in the load resistance. This cell behavior is contrary to the cell behavior when extinction or ignition does not occur.

To unravel the differences between dynamic behavior of the cell (a) when ignition or extinction occurs and (b) that when ignition or extinction does not occur, the dynamic response of the cell to a step change in the load resistance, from 10 to 5 Ω (outside the multiplicity region), is depicted in Figure 2.19. This figure shows that the cell voltage and current changes are in the opposite direction, and this behavior is opposite to the one observed in at the ignition point, shown in Figure 2.18. This is due to the effects of the electrolyte ohmic resistance and the cell current. When the ignition occurs, the cell current and temperature increase. With the temperature increase, the electrolyte ohmic resistance and the ohmic overpotential decrease. Figure 2.20 shows the changes in the ohmic overpotential in the two cases of step change in the load resistance from 0.014 to 0.01 and 10 to 5 Ω. When the ignition occurs, the ohmic resistance has a dominating effect, leading to a decrease in the ohmic overpotential, while when the ignition or extinction does not occur the cell current is more dominant, resulting in an increase in the ohmic overpotential.

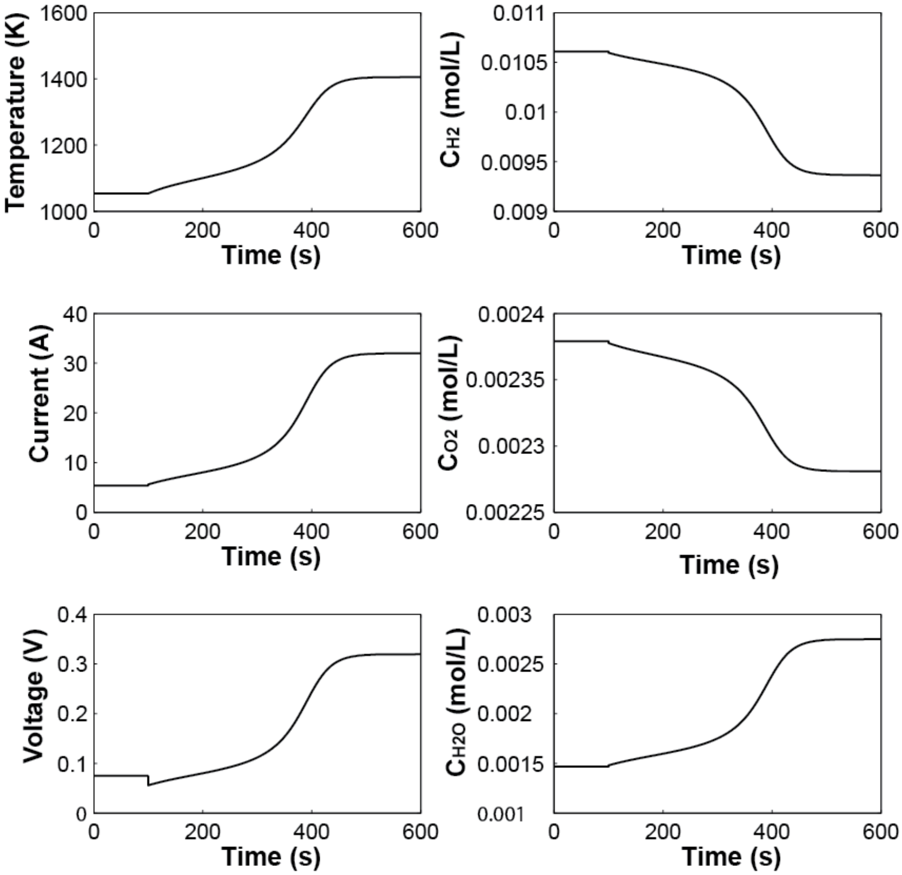

Figure 2.18. Dynamic response of the SOFC to a step change in the load resistance from 0.014 to 0.01 Ω, based on the more detailed model.

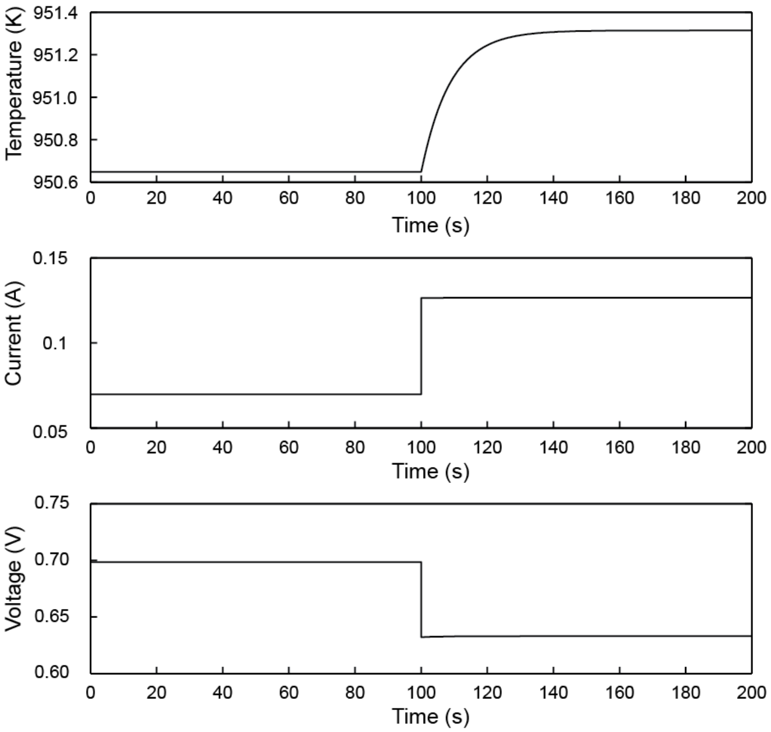

Figure 2.19. Dynamic response of the SOFC to a step change in the load resistance from 10 to 5 Ω, based on the more detailed model.

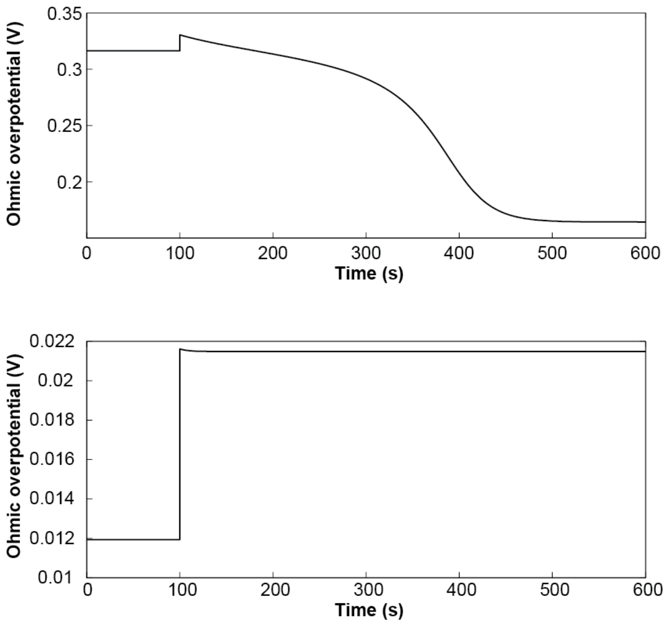

Figure 2.20. Variations in the ohmic overpotential in response to a step change in the ohmic load resistance, a) 0.014 to 0.01 Ω, and b) 10 to 5 Ω.

2.7 Conclusions

The steady state and dynamic behaviors of a SOFC were studied using a detailed lumped model of a planar SOFC. The SOFC system exhibits multiple steady states under certain parameter values. The effects of several operating parameters such as the heat convection coefficient, gas channel temperatures, and fuel and air flow rates on the steady-state multiplicity behavior of the cell were shown. Intricate dynamic characteristics, such as multistability, and temperature ignition and extinction under constant ohmic load and potentiostatic operations, were identified. A unique stable steady state was identified under galvanostatic control. The simulation results showed that with the addition of heat and mass transfer of the gas channel subsystem to the simple model, the steady state multiplicity region shifts towards the higher values of load resistance. Furthermore, under identical operating conditions in specific regions; the detailed SOFC model showed a unique steady state, while the simple SOFC model of Mangold et al.[56], which neglected the mass transfer dynamics and heat transfer in gas channels, exhibited multiple steady states.

Notation

B= length of gas channels (m)
C_p= specific heat capacity of the solid (J mol^{-1} K^{-1})
d_A= thickness of anode (m)
d_C= thickness of cathode (m)
d_E= thickness of electrolyte (m)
E^A= activation energy of the anodic reaction (J mol^{-1})
E^C= activation energy of the cathodic reaction (J mol^{-1})
E^0= standard potential (V)
F = Faraday constant (A s mol^{-1})

H= enthalpy (J mol^{-1})

ΔH_R= enthalpy change of the overall reaction (J mol^{-1})

i= cell current density (A m^{-2})

I= cell current (A)

L= length of the cell (m)

$\dot{n}$= molar flow rate (mol s^{-1})

T= temperature (K)

U^0= ideal voltage (V)

v= velocity (m s^{-1})

W= height of gas channels (m)

y_j= mole fraction

Greek Letters

α = heat transfer coefficient (W m^{-2} K^{-1})

β= coefficients in the electrolyte conductivity

γ = pre-exponential kinetic factor (A m^{-2})

δ = pore mean radius (m)

Δ = thickness of the diffusion layer (m)

ε = porosity

η = activation overpotential (V)

θ= charge transfer coefficient

υ= diffusion volumes for molecules

ρ = resistivity (Ω m)

ρ^s = density of the solid (kg m^{-3})

τ = tortuosity

Subscripts

A	anode
C	cathode
E	electrolyte
S	solid

3 Chapter 3: Mathematical Modeling and Steady-State Analysis of a Proton-Conducting Solid Oxide Fuel Cell

3.1 Introduction

In a SOFC, the electrolyte can be a proton-conducting material instead of the common oxygen ion-conducting oxides. The typical oxygen ion-conducting electrolyte is yttria-stabilized zirconia (YSZ), which requires the cell to be operated at high temperatures from 800 to 1200˚C to exhibit high ionic conductivity. This is due to the high activation enthalpies of their conductivity [85]. Because of their high operation temperature, SOFCs with oxygen ion-conducting electrolytes have two major drawbacks: long start-up and shut-down, and the high cost of materials that stand the high temperatures, in the manufacture of the fuel cells [86]. By lowering the operation temperature to 600-800˚C, these challenges can be addressed to some extent. One way to develop a low temperature SOFC is to utilize a proton conducting electrolyte. Perovskite-type proton conductors, such as $SrCeO_3$ and $BaCeO_3$, have been doped with low valence cations such as Y^{3+}or Yb^{3+} to create oxide ion vacancies, which are required for the formation of protonic defects [85, 87].

Proton-conducting SOFCs have several advantages over oxygen ion-conducting SOFCs. In doped perovskites, proton transport is generally dominant at temperatures in the range of 400 to 800°C [88-89]. The high conductivity of proton-conducting electrolyte at the lower temperatures lessens the operational cost. Furthermore, the product of electrochemical reaction, water, which is formed at the cathode side, prevents fuel dilution and therefore increases the system efficiency. An external reformer is required to convert hydrocarbon fuel to hydrogen fuel needed for low temperature SOFCs. In high operating temperature SOFCs, internal reforming can eliminate the need for a separate external reformer. However, carbon deposition is still an issue in direct-internal reforming SOFCs. Also, of importance are the system reliability and longevity of the cells as well as the life time of the balance of plant components. At low temperatures, the system is less susceptible to thermal degradation, leading to higher cell efficiency in a long run. As the development of proton-conducting SOFCs is still in an early stage [90], mathematical modeling of the cells can expedite design and optimization of the fuel cells.

There is no study in the literature on steady-state multiplicity in proton-conducting SOFCs. As many efforts are currently directed towards designing novel proton conducting electrolytes to obtain better proton conductivity and chemical stability, detailed steady-state analysis of this type of cells is indispensible to determine whether steady-state multiplicity in the cell temperature can occur. The ignition phenomenon can have detrimental effects on the cell system; sudden large changes in the solid temperature can ruin the balance of plant components. Thus, it is indispensable to study the possibility of the existence of steady-state multiplicity in proton-conducting SOFCs.

This chapter presents mathematical modeling and steady-state analysis of a proton-conducting solid oxide fuel cell with a SCY electrolyte and two platinum electrodes. To develop the model, heat and mass transfer for different subsystems and the electrochemical processes are integrated similar to the developed model in the previous chapter. The model is validated with the experimental data reported in [91], wherein a typical hydrogen-air SOFC with $SrCe_{0.95}Yb_{0.05}O_{3-\alpha}$ as electrolyte and porous platinum as the electrodes was studied.

Organization of the rest of this chapter is as follows. Section 2 describes the model development. Section 3 presents the model validation results. Section 4 presents and discusses the steady state behavior of the system. Finally, Section 5 presents some concluding remarks.

3.2 Model Development

A planar proton-conducting SOFC is considered in this study. Figure 1 shows a schematic of the cell. As explained in Section 1, unlike in oxygen ion-conducting SOFCs, in proton-conducting SOFCs water is produced at the cathode side. The electrochemical reactions in the anode and cathode sides of a proton-conducting SOFC are:

Anode side: $H_2 \rightarrow 2H^+ + 2e^-$

Cathode side: $\frac{1}{2}O_2 + 2H^+ + 2e^- \rightarrow H_2O$

Several phenomena including mass transfer, heat transfer, and electrochemical reactions take place in the cell. To develop the model, it is important to identify the physical processes taking place at different parts of the cell. Similar to the approach presented in Chapter 3, the system is divided to several subsystems based on these phenomena. As shown in Figure 1, the cell is divided into five subsystems: a) Subsystem 1 (SS1): anode gas channel, b) Subsystem 2 (SS2): anode side diffusion layer, c) Subsystem 3 (SS3): solid phase including the anode, cathode and electrolyte, d) Subsystem 4 (SS4): cathode side diffusion layer, and e) Subsystem 5 (SS5): cathode gas channel.

The following assumptions are made:

i. The inlet and outlet velocities of the gas stream in each channel are equal [92].

ii. Each subsystem is considered as a stirred tank. This assumption is applicable, as the electrolyte plane area is 0.01x0.04 m^2.

iii. Heat transfer coefficients for convection between (a) the anode and the fuel stream and (b) the cathode and the air stream are constant.

iv. Heat transfer by radiation between the electrodes and the gases in the anode and cathode side channels is ignored. For nonpolar gases, the radiation heat transfer can be ignored since the gases do not emit radiation [93]. Three of the species, O_2, N2 and H_2 are non-radiating, while water vapor is radiating. Due to the low partial pressure of water vapor, the emissivity factor of water vapor is low, and accordingly heat transfer by radiation is negligible in comparison to heat transfer by convection.

v. All gases are ideal because of low pressure and high temperature operating conditions.

vi. The fuel cell is adiabatic.

vii. A 0-dimensional model is developed by writing mass and energy balances, and accounting for electrochemical processes. In the following subsections, we explain the electrochemical processes in detail.

A 0-dimensional model is developed by writing mass and energy balances, and accounting for electrochemical processes. In the following subsections, we explain the electrochemical processes in detail.

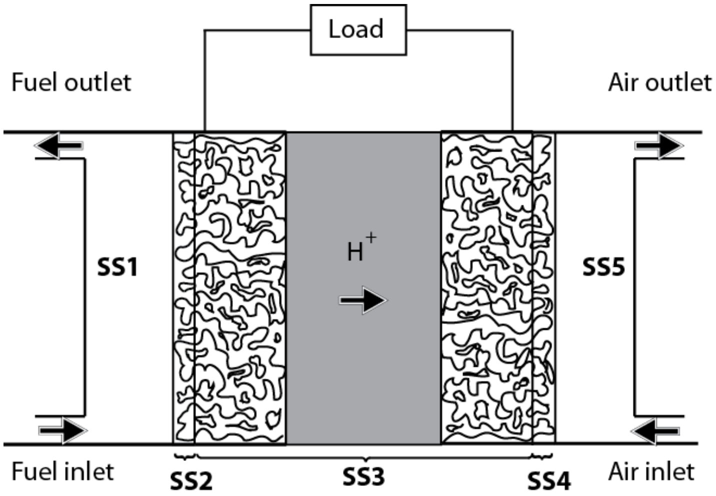

Figure 3.1. Planar SOFC divided into five subsystems.

3.2.1 Electrochemical Model

The electrochemical model is similar to what described in chapter 3 for oxygen-conducting SOFCs. The Nernst equation is used to calculate the reversible cell voltage, Eq. 3.9. As explained in Chapter 3, the actual cell voltage is lower than the reversible cell voltage calculated by the Nernst equation due to activation, ohmic and concentration overpotentials. At low currents, the activation overpotential is dominant. As the cell current increases, ohmic losses (mainly due to the resistance of the electrolyte than electrodes) lower the cell potential. Lastly at high current densities, mass-transport limitations are the dominant cause in lowering the cell potential. The overall cell voltage, U_{cell}, is calculated from Eq. 3. 10.

The anode and cathode activation overpotentials, η_{an} and η_{cath} are calculated using the two Butler-Volmer equations:

$$\frac{I}{LB} = i_{0,an}\left\{\exp\left(\alpha\frac{nF}{RT_s}\eta_{an}\right) - \exp\left(-\frac{(1-\alpha)nF}{RT_s}\eta_{an}\right)\right\} \tag{3.1}$$

$$\frac{I}{LB} = i_{0,cath} \left\{ \exp\left(\alpha \frac{nF}{RT_s} \eta_{cath} \right) - \exp\left(-\frac{(1-\alpha)nF}{RT_s} \eta_{cath} \right) \right\} \tag{3.2}$$

Here, α is the symmetric factor. A value of 0.5 is considered for the factor in this study [94].

There are two approaches for the calculation of the exchange current densities, $i_{0,an}$ and $i_{0,cath}$, in the literature. In one approach, the dependence of the exchange current densities on the absolute temperature and species partial pressures is described using Arrhenius type equations [79, 95]. In the other approach, the exchange current density is assumed to be constant [96]. For oxygen ion-conducting SOFCs, one can find several correlations for the exchange current densities in the literature. These correlations are based on the reaction kinetics [95]. However, for proton-conducting SOFCs, correlations to describe the dependence of the exchange current densities on temperature and species partial pressures have not been reported yet. Therefore, the exchange current densities have been assumed to be constant, and their estimates have been obtained by fitting models of the fuel cells to experimental data [91].

To calculate the cell voltage, the ohmic and concentration overpotentials should be defined as well. Concentration overpotential is calculated by Eq.3.14. The ohmic overpotential, $\rho_E d_E i$, represents the resistance of the electrolyte to proton flow, where ρ_E is the electrolyte resistivity, d_E is the electrolyte thickness, and i is the current density. The electrolyte resistivity decreases as the operating temperature increases. The dependence is typically defined using an Arrhenius type correlation [96-97]:

$$\rho_E = \frac{1}{225.92}\exp\left(\frac{6.3*10^3}{T_s}\right) \tag{3.3}$$

3.2.2 **Energy Conservation**

Conservation of energy is considered for the three subsystems, SS1, SS3 and SS5. We assume that temperatures in the anode and cathode side diffusion layers are equal to that of the solid phase of the cell, T_s.

The energy conservation equation for the solid phase (SS3) accounts for the flow of heat in and out through the transport of reactants to the reaction sites and transport of product to the gas channel respectively, as well as convective heat transfer between the solid part and the fuel and air streams, and the electric power supplied to the external load. The energy balance is presented by the following equation:

$$(d_A + d_E + d_C)\rho_s C_{p_s}\frac{dT_s}{dt} = \Delta H_R - U_{cell}\frac{I}{LB} + h_{an}(T_{an} - T_S) + h_{cath}(T_{cath} - T_S) \tag{3.4}$$

Where $\Delta H_R = N_{O_2}H_{O_2}^{cath} + N_{H_2}H_{H_2}^{an} - N_{H2O}H_{H2O}^{cath}$

The energy balances for the anode and cathode gas channels are as follow:

$$\begin{aligned}&(LBW)\frac{d(c_{fuel}^{an}c_{p\,fuel}^{an}T_{an})}{dt} = \\ &\dot{n}_{fuel,in}^{an}H_{fuel,in}^{an} - v_{fuel}^{an}c_{fuel}^{an}H_{fuel}^{an}BW + h_{an}(T_s - T_{an})LB - N_{H_2}H_{H_2}^{an}LB\end{aligned} \tag{3.5}$$

$$\begin{aligned}&(LBW)\frac{d(c_{air}^{cath}c_{p\,air}^{cath}T_{cath})}{dt} = \\ &\dot{n}_{air,in}^{cath}H_{air,in}^{cath} - v_{air}^{cath}c_{air}^{cath}H_{air}^{cath}BW + h_{cath}(T_s - T_{cath})LB - N_{O_2}H_{O_2}^{cath}LB \\ &+N_{H_2O}H_{H_2O}^{cath}LB\end{aligned} \tag{3.6}$$

where h_{an} and h_{cath} are the convective heat transfer coefficients for the fuel and the air streams, respectively.

3.2.3 **Mass Conservation**

The mass balances are written for different species in the cell (i.e., hydrogen, water and oxygen). The balance equations for the three different species in the triple phase boundary zone are as follow:

$$\frac{\Delta_{cath}}{R}\frac{d}{dt}\left(\frac{p_{O_2}^{TPB}}{T_S}\right)=N_{O_2}-\frac{1}{LB}R_{O_2} \tag{3.7}$$

$$\frac{\Delta_{cath}}{R}\frac{d}{dt}\left(\frac{p_{H_2O}^{TPB}}{T_S}\right)=-N_{H_2O}+\frac{1}{LB}R_{H_2O} \tag{3.8}$$

$$\frac{\Delta_{an}}{R}\frac{d}{dt}\left(\frac{p_{H_2}^{TPB}}{T_S}\right)=N_{H_2}-\frac{1}{LB}R_{H_2} \tag{3.9}$$

where R_{H_2} and R_{O_2} are the rates of consumption of hydrogen and oxygen, respectively, and R_{H_2O} is the rate of generation of water by the electrochemical reactions, as explained in Chapter 3, Eqs 3.6, 3.7 and 3.8 .

N_j is the molar flux of species j transferred from the gas channel into the diffusion layer or vice versa. The mass flux of the diffusing species can be defined in terms of the mass transfer coefficient using:

$$N_{O_2}=k_{O_2}^{cath}\left(c_{air}^{cath}\,y_{O_2}^{cath}-\frac{p_{O_2}^{TPB}}{RT_S}\right) \tag{3.10}$$

$$N_{H_2}=k_{H_2}^{an}\left(c_{fuel}^{an}\,y_{H_2}^{an}-\frac{p_{H_2}^{TPB}}{RT_S}\right) \tag{3.11}$$

$$N_{H_2O}=k_{H_2O}^{cath}\left(-c_{air}^{cath}\,y_{H_2O}^{cath}+\frac{p_{H_2O}^{TPB}}{RT_S}\right) \tag{3.12}$$

where k_j is the mass transfer coefficient of species j, given by

$$k_{H_2}^{an} = \frac{D_{e_{H_2}}}{\Delta_{an}} = \frac{\varepsilon_{an}}{\tau_{an}\Delta_{an}} D_{H_2} \tag{3.13}$$

$$k_{H_2O}^{an} = \frac{D_{e_{H_2O}}}{\Delta_{cath}} = \frac{\varepsilon_{cath}}{\tau_{cath}\Delta_{cath}} D_{H_2O} \tag{3.14}$$

$$k_{O_2}^{cath} = \frac{D_{e_{O_2}}}{\Delta_{cath}} = \frac{\varepsilon_{cath}}{\tau_{cath}\Delta_{cath}} D_{O_2} \tag{3.15}$$

D_{e_j} is the effective diffusion coefficient of species j, ε_{cath} and τ_{cath} are the porosity and tortuosity of the cathode, respectively, and ε_{an} and τ_{an} are the porosity and tortuosity of the anode electrode. D_j is the total diffusion coefficient of species j; it is described by two mechanisms of molecular diffusion and Knudsen diffusion[81, 94]:

$$\frac{1}{D_j} = \frac{1}{D_{j,i/mix}} + \frac{1}{D_{K_j}} \tag{3.16}$$

The Knudsen diffusion coefficient, D_{K_j}, depends on the pore mean radius; cell temperature and species molecular weight and is calculated from [80]:

$$D_{K_j} = 97\delta_{cath/an}\sqrt{\frac{T_S}{M_j}} \tag{3.17}$$

$D_{j,i/mix}$ is the binary diffusion coefficient of species j in i, or in the case of multiple components in the system it is the diffusion coefficient of species j in the mixture. In this study, we have three species, O_2, N_2 and H_2O, in the cathode gas stream, so the molecular diffusion is ternary diffusion; the diffusion coefficients are given by the Wilke formula [98-99].

$$D_{j,mix} = \frac{1-x_j}{\sum_{i=1,i\neq j}^{n} \frac{x_i}{D_{j,i}}} \tag{3.18}$$

The binary diffusion coefficient $D_{j,i}$ is calculated using the Chapman and Enskog equation [100]:

$$D_{j,i} = \frac{0.00266 T^{\frac{3}{2}}}{p M_{ji}^{\frac{1}{2}} \sigma_{ji}^{2} \Omega_D} \tag{3.19}$$

where $D_{j,i}$ = diffusion coefficient (cm^2/s), T = temperature (K), p = pressure (bar), σ_{ji} =characteristic length (Å), $\sigma_{ji} = (\sigma_j + \sigma_j)/2$, and Ω_D= diffusion collision integral. M_{ji} in Eq.3.19 is defined as:

$$M_{ji} = 2\left(\frac{1}{M_j} + \frac{1}{M_i}\right)^{-1} \tag{3.20}$$

M_j and M_i are molecular weights of j and i species. Ω_D is a function of KT/ε, where k is the Boltzmann's constant, and ε is the characteristic Lennard-Jones energy, given by [100]:

$$\Omega_D = \frac{A}{(T^*)^B} + \frac{C}{\exp(DT^*)} + \frac{E}{\exp(FT^*)} + \frac{G}{\exp(HT^*)} \tag{3.21}$$

Here, $T^*=KT/\varepsilon_{ji}$ and $\varepsilon_{ji}=(\varepsilon_j \varepsilon_i)^{1/2}$ .The values of the parameters in Eq. 3.21 are given in

Table 3-1. Parameter values in Eq. 3.21.

Parameter	Value	Source
A	1.06036	100
B	0.15610	100
C	0.19300	100
D	0.47635	100
E	1.03587	100
F	1.52996	100
G	1.76474	100
H	3.89411	100

Mass conservation equations for species in the gas channels are as follows:

$$LBW \frac{dc_{air}^{cath}}{dt} = \dot{n}_{air,in}^{cath} - v_{air}^{cath} c_{aiir}^{cath} WB - N_{O_2} LB + N_{H_2O} LB \tag{3.22}$$

$$LBW\frac{d(c_{air}^{cath}y_{O_2}^{cath})}{dt}=\dot{n}_{air,in}^{cath}y_{O_2,in}-v_{air}^{cath}c_{air}^{cath}y_{O_2}^{cath}WB-N_{O_2}LB \tag{3.23}$$

$$LBW\frac{d(c_{air}^{cath}y_{H_2O}^{cath})}{dt}=-v_{air}^{cath}c_{air}^{cath}y_{H_2O}^{cath}WB+N_{H_2O}LB \tag{3.24}$$

$$LBW\frac{dc_{fuel}^{an}}{dt}=\dot{n}_{fuel,in}^{an}-v_{fuel}^{an}c_{fuel}^{an}WB-N_{H_2}LB \tag{3.25}$$

$$LBW\frac{d(c_{fuel}^{an}y_{H_2}^{an})}{dt}=\dot{n}_{fuel,in}^{an}y_{H_2,in}-v_{fuel}^{an}c_{fuel}^{an}y_{H_2}^{an}WB-N_{H_2}LB \tag{3.26}$$

Eqs. 3.22, 3.23 and 3.24 are for the cathode gas stream (overall mole balance for the air stream, O_2 mole balance and H_2O mole balance, respectively), and Eqs. 3.25 and 3.26 are fuel stream and hydrogen mole balances, respectively. The model parameter values are listed in Table 3-2.

Table 3-2. Parameter values of the model.

parameter	value	source
Electrolyte-supported cell		
d_A	5×10^{-5} m	96
d_C	5×10^{-4} m	96
d_E	5×10^{-5} m	96
Anode- supported cell		
d_A	5×10^{-4} m	96
d_C	5×10^{-5} m	96
d_E	5×10^{-5} m	96
L	0.04 m	96
B	0.01 m	96
W	10^{-3} m	

$\dot{n}^{\mathrm{cat}}_{\mathrm{air,in}}$	3.8×10^{-2} mol s^{-1}	96
$\dot{n}^{\mathrm{an}}_{\mathrm{fuel,in}}$	1.39×10^{-3} mol s^{-1}	96
$T^{\mathrm{cat}}_{\mathrm{air,in}}$	750 K-variable	
$T^{\mathrm{an}}_{\mathrm{fuel,in}}$	750 K-variable	
α	0.5	96
$i_{0,a}$	700 A m^{-2}	
$i_{0,c}$	700 A m^{-2}	
h	25 W m^{-2}K^{-1}-variable	
Δ_{ano}	5×10^{-6} m	
Δ_{cat}	5×10^{-6} m	
ε_{cat}	0.4	96
ε_{an}	0.4	96
τ_{an}	5	96
τ_{cat}	5	96
δ_{an}	5×10^{-7}	96
δ_{cat}	5×10^{-7}	96
$y_{O_{2,\mathrm{in}}}$	0.2	96
$y_{N_{2,\mathrm{in}}}$	0.8	96
$y_{H_{2,\mathrm{in}}}$	0.97	96
$y_{\mathrm{H_2O_{in}}}$	0.03	96

3.3 Model Validation

The polarization curve of a fuel cell is a major representative of the performance of the cell. To obtain the polarization curve of the cell under isothermal conditions theoretically, the governing equations in Section 2, except for the energy balance equations, are solved. The isothermal model consists of 8 differential equations and three algebraic equations. At steady state, the differential equations reduce to algebraic equations. Thus, the model at steady state is a system of 11 coupled nonlinear algebraic equations, which is solved using the `fsolve` routine of MATLAB. This routine is based on the default trust-region-dogleg algorithm.

The model is validated using the experimental data reported in [91] obtained under isothermal operation at 1073 K. Figure 3.2 shows the experimental data and the model predictions. The unknown parameters, the exchange current densities ($i_{0,an}$ and $i_{0,cath}$) are estimated from the experimental data. The exchange current densities are assumed to be equal. The estimated values of $i_{0,an}$ and $i_{0,cath}$ are found to be 700 ± 91 A/m^2, which is close to the value reported by Patcharavorachot et al. [96].

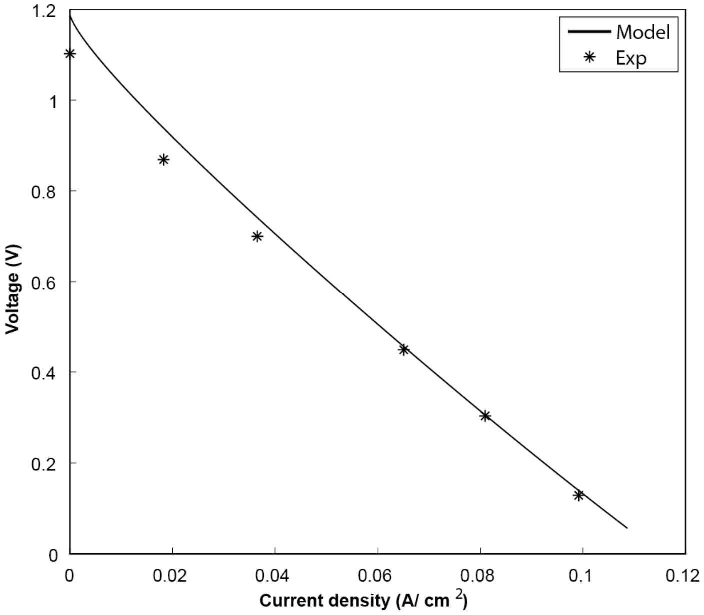

Figure 3.2. The IV curve at 1073 K: experimental data [91] and the model predictions.

3.4 Steady-state Multiplicity

The heat removal (linear) and heat generation (S-shaped curve) are plotted in the same diagram as a function of the solid temperature. As mentioned in previous section, by solid, we mean the anode, cathode and electrolyte as a single unit (SS3). As shown in Figure 3.3, the fuel cell may have one or three steady states. The heat generation and heat removal terms are shown for two cases corresponding to the external load resistance of 0.47 Ω at two different values of heat convection coefficient, 25 and 75 W/m^{2}K. In the case of heat convection coefficient equal to 25 W/m^{2}K, there are three steady states, the middle steady-state (point B) is unstable, while the other two (points A and C) are stable. At higher heat convection coefficient equal to 75 W/m^{2}K, there is one intersection point (A$^{'}$) presenting a unique steady state in the system. Figure 3.4 depicts the heat removal and heat generation terms at a higher load resistance of 5 Ω but with the same heat convection coefficient of 25 W/m^{2}K as in Figure 3.3. At this higher load resistance, as shown in Figure 3.4, the cell has a unique stable steady state.

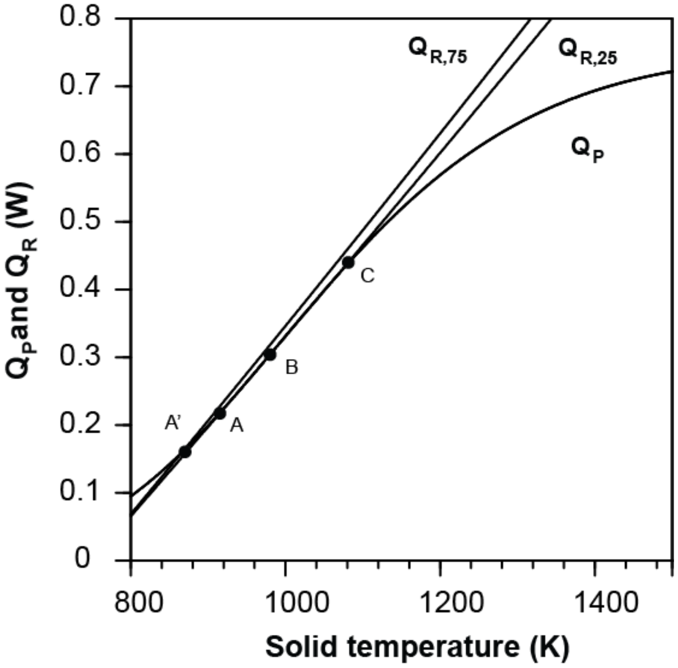

Figure 3.3. Steady state behavior under inlet gas channel temperatures of 750 K: Steady-state heat generation (Q_P) and heat removal ($Q_{R,25}$, $Q_{R,75}$) versus the solid

temperature at an external load resistance of 0.47 Ω, at two different values of the heat convection coefficient, (a) 25 and (b) 75 W/m^{2}K .

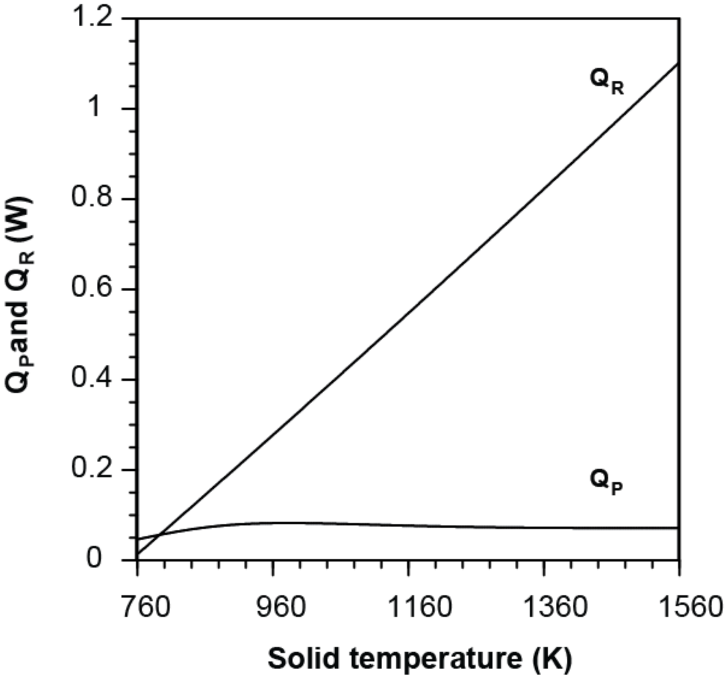

Figure 3.4. Steady-state heat generation (Q_P) and heat removal (Q_R) versus the solid temperature at an external load resistance of 5 Ω and a heat convection coefficient of 25 W/m^{2}K.

To analyze the effect of design conditions, the steady-state behavior of two types of SOFCs, an electrolyte-supported SOFC and an anode-supported SOFC is investigated. In an electrolyte-supported cell, a thick electrolyte supports the both electrodes, anode and cathode [54]. In an anode-supported SOFC design, a thin electrolyte is fabricated on a thick anode. Thus, the ohmic resistance of the electrolyte is lower compared to the electrolyte-supported case [54].

3.4.1 **Electrolyte-Supported Cell**

3.4.1.1 Constant Ohmic Load Operation

The steady-state behavior of the cell under constant ohmic load operation is studied to determine whether steady-state multiplicity exists and the parameter space in which the multiplicity occurs. As mentioned earlier, the bifurcation parameter is the external load resistance. Figure 3.5 shows the bifurcation diagrams of mole fractions of different species at the anode and cathode gas channels, outlet gas temperatures and the solid temperature. Interestingly, it can be observed that concentration and temperature multiplicities coexist. It can be seen that there is a region of three steady states between 0.465 and 0.474 Ω .The bifurcation curve for reactant species O_2 and H_2 is in the form of a S-shaped curve, while that of the product, water, is in the form of an inverse S-shaped curve. Suppose the cell is operating at the steady state point in the extinction branch solid temperature. As the resistive load decreases, the steady state follows this curve. Any further decrease in the load below the ignition point results in the steady state jumping to the high temperature branch. If we follow the behavior of the other variables; that is, outlet gas streams temperatures and water mole fraction in the cathode gas channel, the same behavior can be observed. As the solid temperature ignites to the upper branch, the cell current increases and accordingly the rates of consumption of the reactants and production of the product increase. This exhibits that temperature ignition is accompanied by concentration extinction of the reactants and concentration ignition of the product.

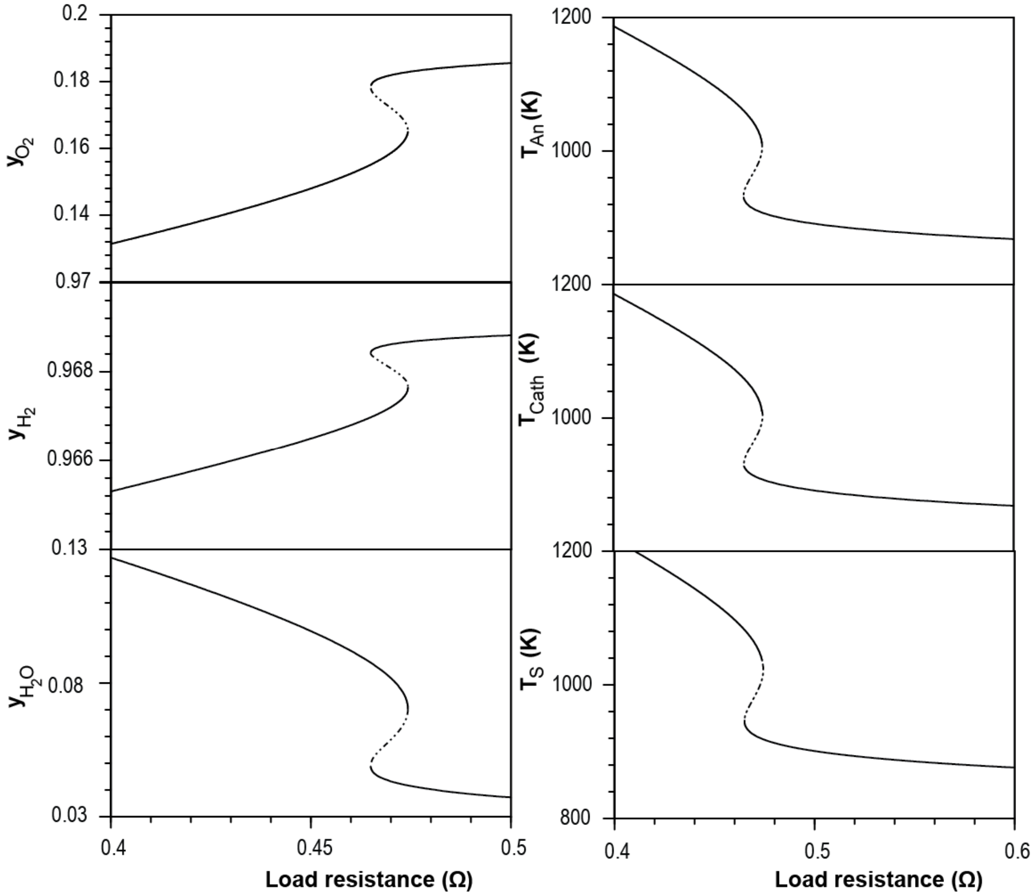

Figure 3.5. Bifurcation diagrams under constant ohmic load: species mole fractions (y_{O_2}, y_{H_2} , and y_{H_2O}) in the gas channels, the outlet gas temperatures (Tan, Tcath) and the solid temperature (Ts) versus load resistance.

The bifurcation analysis can be in terms of the load power density instead of the load resistance. Figure 3.6 shows the bifurcation curve of the solid temperature versus the load power density. For given cell operating conditions, the cell power is maximum at a certain ohmic load. The range of the load power density is 0-50 mW/cm^2 for the single cell under study.

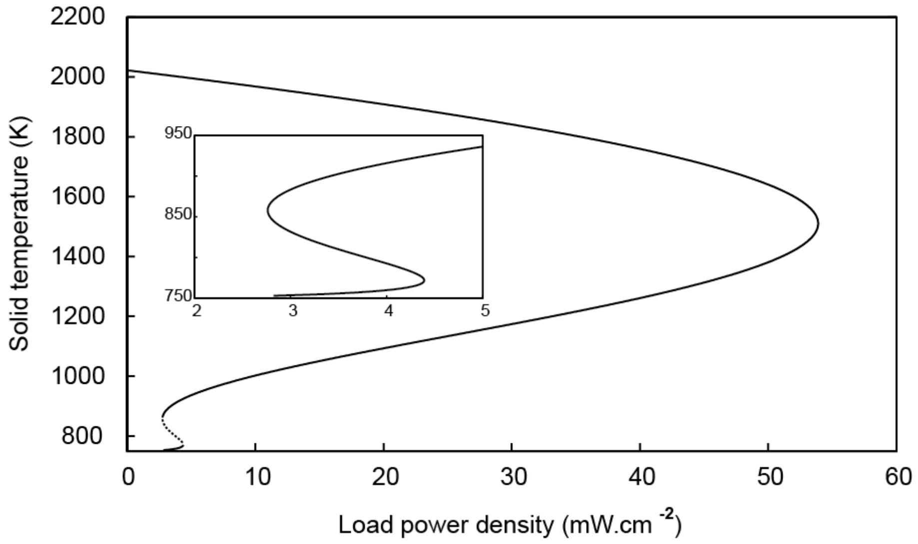

Figure 3.6. Bifurcation curve of the solid temperature versus the load power density.

To locate the multiple steady-state region, the ignition and extinction points (saddle-node bifurcation points) are determined at different values of inlet gas temperatures. As shown in Figure 3.7, the shaded area represents the steady-state region at different values of heat convection coefficients. It can be seen that the shaded area shifts toward the lower values of load resistance with the increase in the heat convection coefficient. This behavior is expected from the fuel cell: as the heat transfer coefficient increases, the rate of heat dissipation increases, and thus to operate the cell at the same steady-state solid temperature, the electrochemical reactions have to release more thermal energy. The higher rate of heat generation by the electrochemical reactions is possible at a higher current, which corresponds to a lower load resistance.

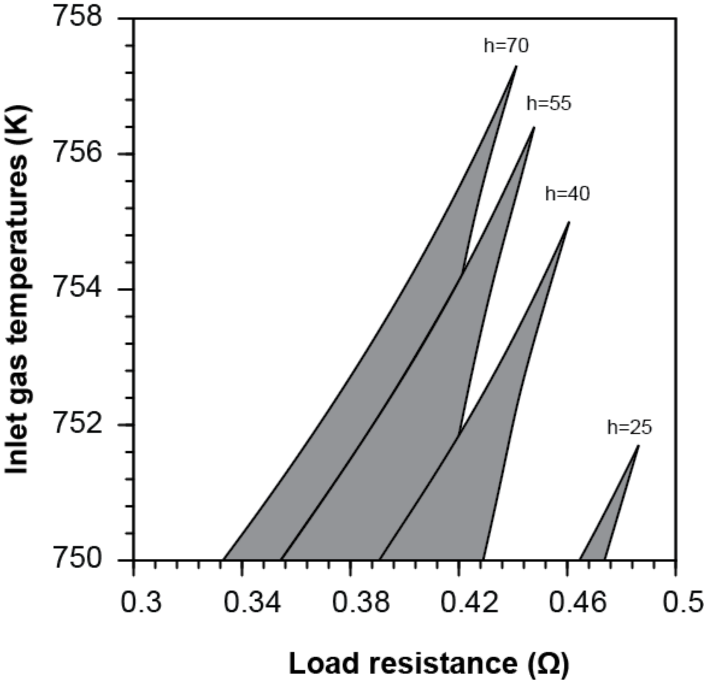

Figure 3.7. Multiplicity region for different heat convection coefficients in the constant ohmic load operation.

Figure 3.8 shows the steady-state manifold of the cusp catastrophe. We can observe that at higher values of inlet gas temperatures the multiple steady state region disappears. The multiplicity region can be detected by projecting the turning points (ignition and extinction points) locus onto the parameter space. Also, the cusp catastrophe surface is plotted considering the three bifurcation parameters, the inlet fuel and air flow rates and the external load resistance, in Figure 3.9. The manifold shows that the three-steady-state region disappears as the inlet fuel and air flow rates decrease.

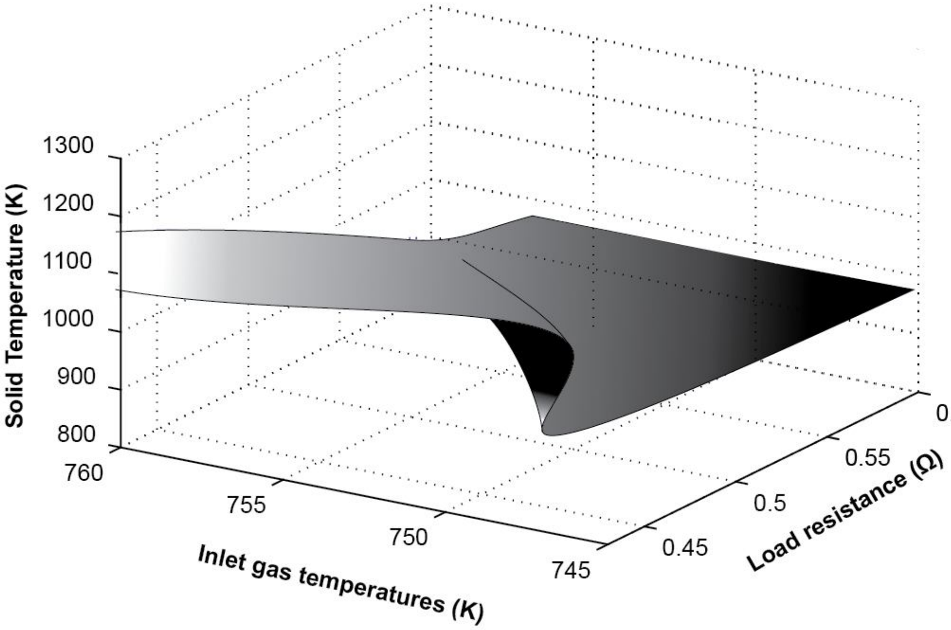

Figure 3.8. Solid temperature versus load resistance as the inlet gas temperatures vary.

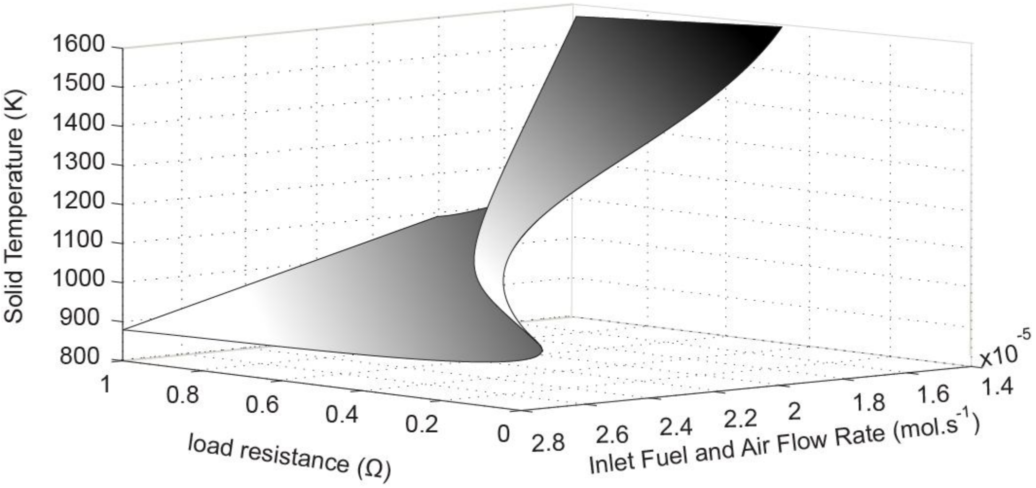

Figure 3.9. Solid temperature versus load resistance as the inlet fuel and air flow rates vary.

3.4.1.2 Potentiostatic Operation

Under potentiostatic operation, the cell voltage is kept constant. Therefore, the cell voltage is a bifurcation parameter. The bifurcation diagrams are shown in Figure 3.10 for the species mole fractions, outlet gas temperature and solid temperature. The behavior is similar to the constant ohmic load operation. Ignition and extinction phenomena can be observed for the species concentration and cell temperature. The bifurcation curves for reactants are opposite to those for solid temperature and product concentration, which means while the reactants are in the ignition branch, the cell temperature and product concentration are extinguished.

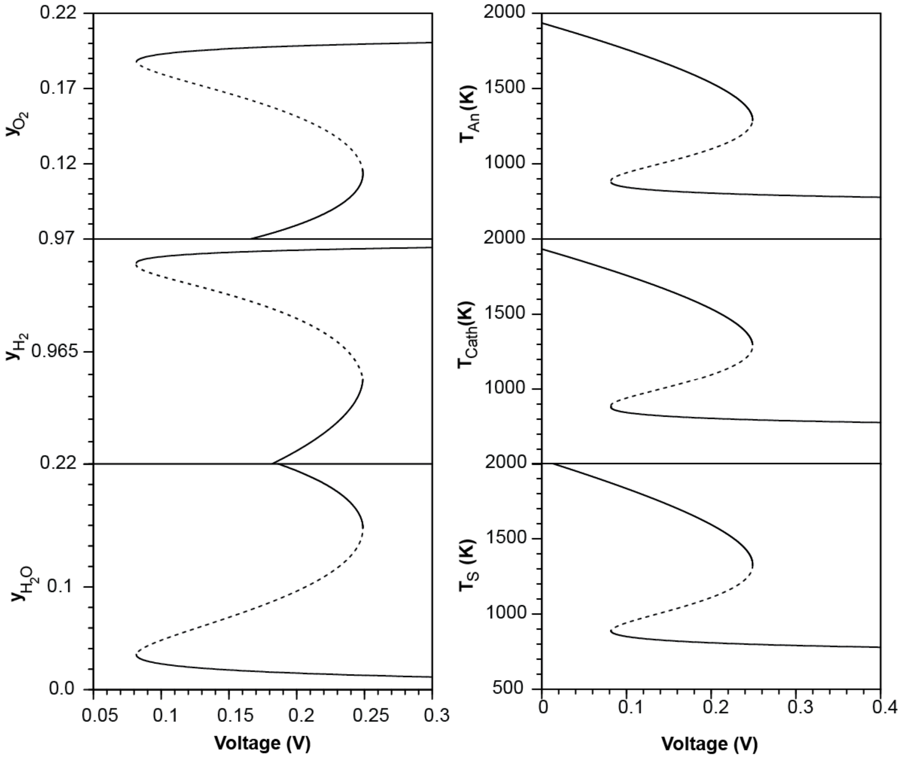

Figure 3.10. Bifurcation analysis under potentiostatic mode: species mole fractions (y_{O_2} , y_{H_2} , and y_{H_2O}) in the gas channels, the outlet gas temperatures (T_{an}, T_{cath}) and the solid temperature (T_s) versus cell voltage.

Figure 3.11 shows the effect of heat convection coefficient on the multiple steady-state region. The values of cell voltage on the ignition and extinction points are obtained at different values of the inlet channel gas temperatures to find out the multiple steady state region. As the heat convection coefficient increases, heat dissipation increases and the solid temperature decreases, which in turn lowers the cell voltage.

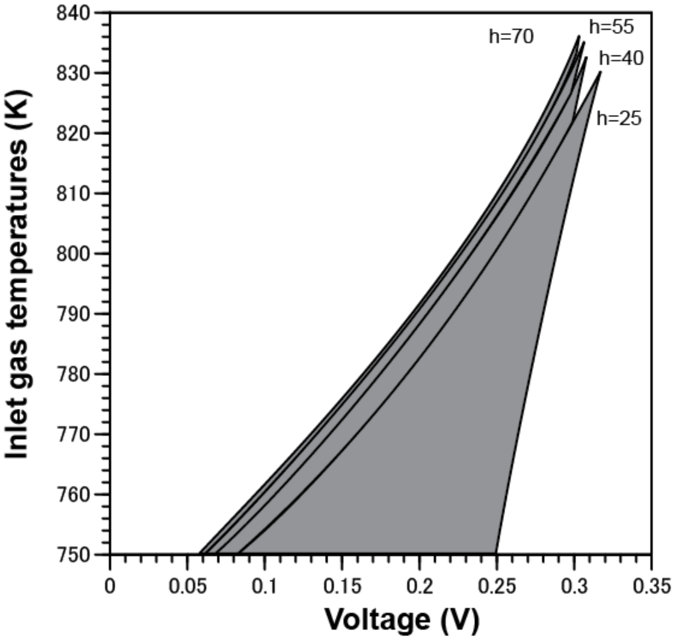

Figure 3.11. Multiplicity region for different heat convection coefficient values in the potentiostatic mode.

Figure 3.12 depicts the bifurcation diagram of solid temperature versus inlet gas temperatures at constant values of cell voltage. It can be seen that at higher values of cell voltage, the S-shaped curve shifts to higher values of inlet gas temperatures. As the cell voltage increases, the rate of heat removal from the cell increases. This increase in the rate of heat removal, at steady state conditions, leads to an increase in the rate of heat production, and therefore at a constant solid temperature to control the cell at higher value of cell voltage the inlet gas temperatures should increase. We can observe that the multiple steady-state region disappears as the cell voltage increases.

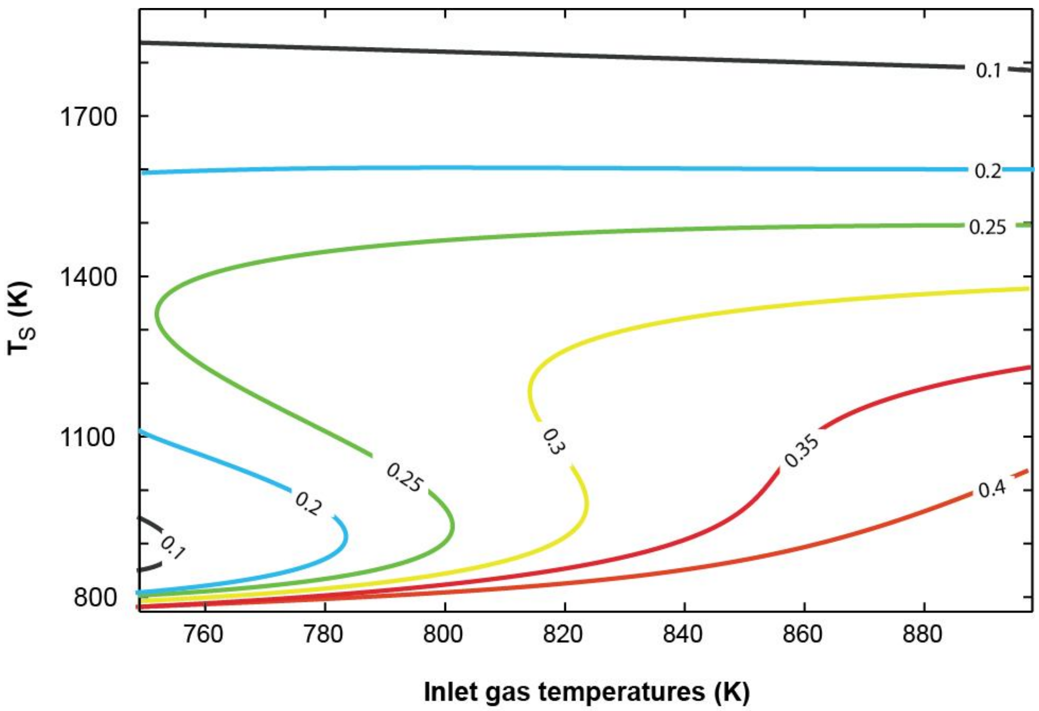

Figure 3.12. Solid temperature versus the inlet gas temperatures at different values of cell voltage.

3.4.1.3 Galvanostatic Operation

In the galvanostatic operation mode, the cell current is under control. As shown in Figure 3.13, we can observe that there is a unique steady state for all the variables, species concentration, outlet gas temperatures and cell temperature. This result is in agreement with that of an oxygen ion-conducting SOFC.

3.4.2 **Anode-Supported Cell**

To study and compare the steady-state behaviors of an electrolyte-supported cell and an anode-supported cell, for these two designs the bifurcation diagram of the solid temperature versus load resistance is plotted. As shown by plot (b) of Figure 3. 14, in the case of an anode-supported cell there is a monotonic relationship between the solid temperature and the external load, presenting a unique steady state in the system. The inset plot shows simulation results for a higher range of external load resistance. On the other hand, in the case of electrolyte-supported cell, plot (a), there can be up to three steady states. At a constant load resistance, the solid temperature of the anode-supported cell is higher than that of the electrolyte-supported cell due to the lower ohmic resistance of the electrolyte in the anode-supported cell.

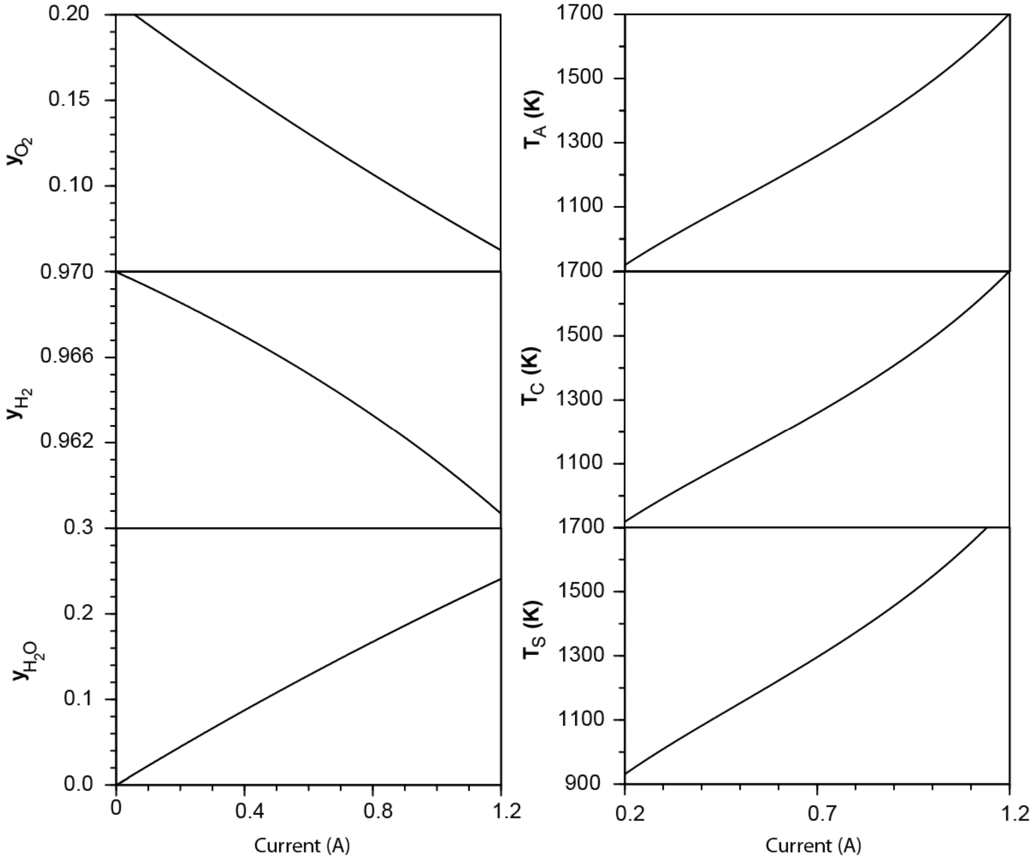

Figure 3.13. Species mole fractions (y_{O_2}, y_{H_2} , and y_{H_2O}) in gas channels, the outlet gas temperatures (T_{an}, T_{cath}) and the solid temperature (T_s) versus cell current under galvanostatic operation mode.

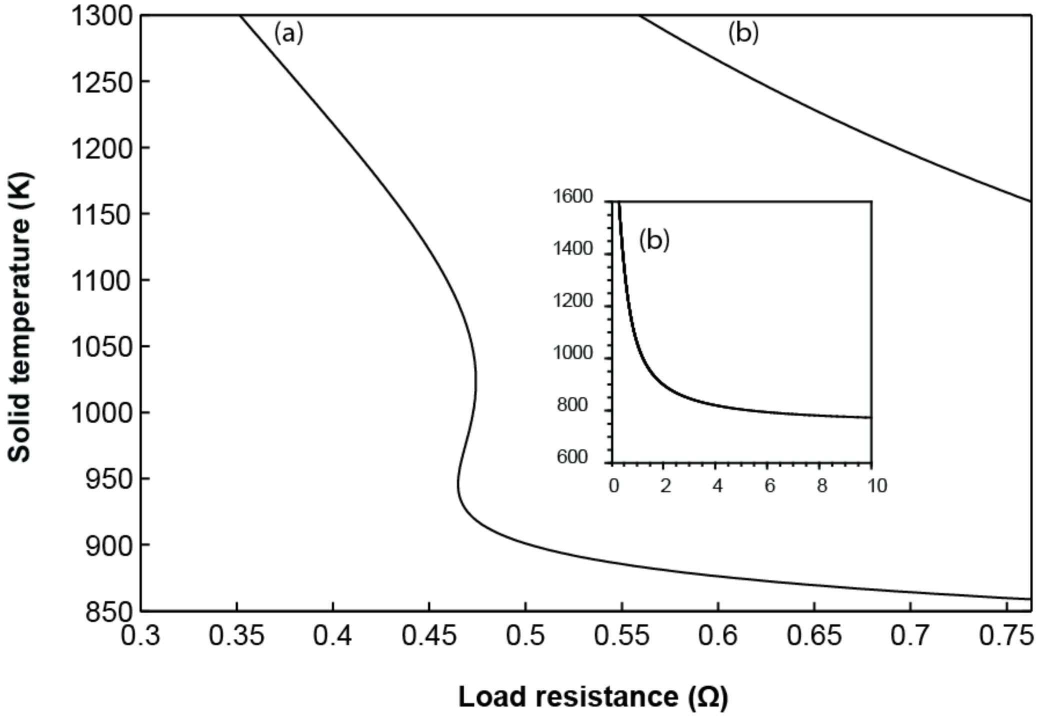

Figure 3.14. Solid temperature versus load resistance. (a) electrolyte-supported cell, (b) anode-supported cell.

3.5 Concluding Remarks

A mathematical model was developed to investigate the presence of steady-state multiplicity in a proton-conducting SOFC. Simulation results showed that steady state multiplicity exists at low inlet fuel and air temperatures. The ignition and extinction phenomena in the solid temperature and outlet gas temperatures were found. This result is in agreement with behavior reported for oxygen ion-conducting SOFCs, in which the existence of multiplicity has been attributed to the dependence of the electrolyte oxygen-ion conductivity to the electrolyte temperature. As the inlet fuel and air temperatures increase, the multiple-steady-state region decreases in size and finally disappears. Under constant ohmic load and potentiostatic operations, it was found that concentration and temperature multiplicities coexist. When ignition (extinction) occurs in the cell solid temperature, ignition (extinction) also happens in water outlet concentration, but extinction (ignition) takes place in the reactants outlet concentrations. While the reactants concentrations are under ignition, the cell temperature and the product concentration are in the extinction branch and vice versa.

It was shown that the type of cell support can affect the existence of multiplicity; a unique stable steady state was found for the anode-supported SOFC with the same parameter values and operation conditions with which an electrolyte-supported SOFC has multiple steady states.

Notation

B= height of cell (m)
C_p= specific heat capacity of the solid (J mol^{-1} K^{-1})
d_A= thickness of anode (m)
d_C= thickness of cathode (m)
d_E= thickness of electrolyte (m)
E^0= standard potential (V)
F = Faraday constant (A s mol^{-1})
h= heat transfer coefficient (W m^{-2} K^{-1})
H= enthalpy (J mol^{-1})
ΔH_R = enthalpy change of the overall reaction (J mol^{-1})
i= current density (A m^{-2})
$i_{0,an}$= exchange current density at anode (A m^{-2})
$i_{0,cath}$= exchange current density at cathode (A m^{-2})
L= length of cell (m)
$\dot{n}$ = molar flow rate (mol s^{-1})
T= temperature (K)

U_0= reversible cell voltage (V)

v= velocity (m s^{-1})

W= width of gas channels (m)

y_j= mole fraction of species j

Greek Letters

α = symmetric factor

δ = pore mean radius (m)

Δ = thickness of the diffusion layer (m)

ε_{an}= porosity of anode

ε_{cath}= porosity of cathode

ε_{ii} = the characteristic Lennard-Jones energy (J) j, i: H_2, H_2O, O_2, N_2

η_{conc} = concentration overpotential (V)

η_{an} = anode activation overpotential (V)

η_{cath} = cathode activation overpotential (V)

ρ = resistivity (Ω m)

ρ_s = density of the solid (kg m^{-3})

σ_{ji} = characteristic length (Å) j, i: H_2, H_2O, O_2, N_2

τ = tortuosity

Ω_D = diffusion collision integral

Subscripts

an = anode

cath = cathode

E = electrolyte

S = solid

Superscripts

TPB = triple phase boundary

4 Chapter 4: Modeling and Bifurcation Analysis of a Co-Ionic-Conducting Solid Oxide Fuel Cell

4.1 Introduction

During the last two decades, several oxides have been found with the potential application as the electrolytes in SOFCs[101]. Among these electrolytes are the ones that have high proton conductivity at lower temperatures or have mixed proton and oxygen ion conductivity under certain conditions.

Among various perovskites, barium cerates are potential candidates for use in SOFCs. $BaCeO_3$ by itself has a low conductivity. When it is doped with a trivalent rare-earth element such as Gd, Nd and Sm, a higher conductivity can be achieved. Substitution of Ce^{4+} with a trivalent rare-earth element causes the oxygen vacancy ($V_O^{\cdot\cdot}$),which is responsible for oxygen anion conductivity, to appear in the lattice to retain the electrical neutrality[102]. The oxygen vacancy can combine with O_2 or H_2O, leading to the formation of the lattice oxygen (O_o^x), an electron hole ($h^{\cdot}$) and a proton (H^+). This can be explained by the following postulated reaction mechanism[102-104]:

$$V_O^{\cdot\cdot} + \frac{1}{2} O_2 \rightarrow O_o^x + 2h^{\cdot}$$

$$V_O^{\cdot\cdot} + H_2O \rightarrow O_o^x + 2H^+$$

$$V_O^{\cdot\cdot} + H_2O + O_o^x \rightarrow 2\ OH_o^{\cdot}$$

$$h^{\cdot} + H_2O \rightarrow 2H^{+} + \frac{1}{2} O_2$$

$BaCeO_3$-base electrolytes exhibit proton conduction under hydrogen-containing atmospheres and are primarily considered as proton conducting ceramics. However, an increase in temperature can change these proton conductors to oxygen-anion conductors[105]. For $BaCe_{1-x}Sm_xO_{3-\alpha}$ electrolytes, as can be seen in Figure 4.1, the proton conductivity increases with temperature up to 1073 K[106]. Above this temperature, proton conductivity drops with temperature, and the oxygen-anion conductivity becomes dominant. This class of solid-state conductors has been shown to behave as a mixed proton and oxygen ion conductor under some fuel cell conditions, as water formation was observed in both cathode and anode gas channels of the cell. To predict the behavior of a fuel cell system with a $BaCeO_3$-base electrolyte and determine the rate of electrochemical reactions, both oxygen ion and proton conduction should be taken into account. To achieve this, protonic and oxide-ionic currents are calculated from the rates of water production at the cathode and anode sides of the cell, respectively.

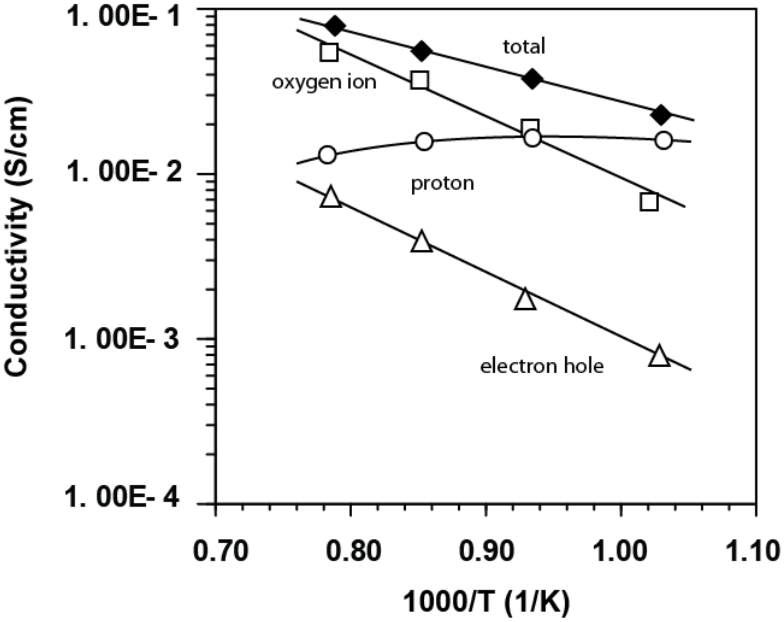

Figure 4.1. Component conductivities in $BaCe_{1-x}Sm_xO_{3-\alpha}$[106].

There have been several studies[107-110] on electrochemical transport and performance behavior of “mixed conducting” oxides for utilization in fuel cells, batteries and sensors. Herein, oxides that have ionic and electronic conductivity (allow one mobile ionic species [e.g., oxygen ion] and electronic carriers [electrons and holes] to go through) are called mixed conducting oxides, and oxides that conduct two different ionic species and electronic charge carriers are referred to as co-ionic conducting oxides. Compared to the studies on fuel cells with mixed conducting oxides[107-110], there have been only a very few theoretical studies on electrochemical transport and performance behavior of co-ionic conducting oxides in solid-state electrochemical devices. For example, Huang et al.[111] presented a mathematical model to describe the performance of a co-ionic conducting ceria-base composite electrolyte fuel cell. Their focus was more on transport of ionic species and electronic carriers and calculation of the ionic and electronic flux by utilizing the intrinsic ionic and electronic transport properties of the oxide layer. They did not account for mass transfer in the gas channels or heat transfer between the solid part of the cell and the gas streams in the cathode and anode gas channels.

The number of studies on mathematical modeling of SOFCs with alternative types of oxides (proton conducting or co-ionic conducting) is very limited. As many researches explore the utilization of these alternative oxides for application in SOFCs, there is also a need to theoretically model and capture the behavior of these fuel cells. Prior to this work, no study on steady-state multiplicity in co-ionic-conducting SOFCs was reported.

This chapter presents a study on mathematical modeling and steady-state analysis of a co-ionic-conducting solid oxide fuel cell with a Sm-doped barium cerate electrolyte, Ni as the anode and $Ni_{0.95}Li_{0.05}O_{1-\alpha}$ as the cathode. The model is validated using the experimental data reported in[106], wherein a hydrogen-air SOFC with $BaCe_{0.9}Sm_{0.1}O_{3-\alpha}$ as electrolyte, Ni as the anode and various oxides as the cathode was studied experimentally. The existence of multiple steady states with respect to ohmic external load, cell outlet voltage, cell current, and cell power density is studied. Detailed steady-state analysis of this type of cells is indispensible to determine whether steady-state multiplicity in the cell temperature can occur.

Organization of the rest of this chapter is as follows. Section 2 describes the model development. Section 3 presents the model parameter estimation and validation results. Section 4 explains the simulation method used to generate the results. Section 5 discusses the steady state behavior of the system. Finally, Section 6 presents some concluding remarks.

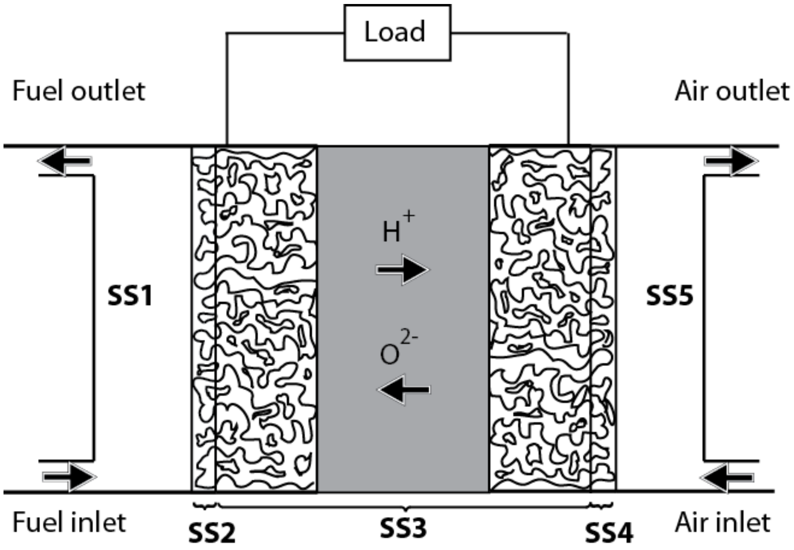

Figure 4.2. Planar SOFC divided into five subsystems.

4.2 Model Development

The SOFC system under study is a single planar SOFC. Figure 4.2 shows the schematic of the SOFC. As can be seen similar to the model development for the oxygen-ion-conducting and the proton conducting SOFC, the cell is divided into five subsystems: 1) anode gas channel, 2) anode side diffusion layer, 3) solid part of the cell consisting of the anode, electrolyte and cathode, 4) cathode side diffusion layer, and 5) cathode gas channel. The model is developed by writing the governing equations, which represent heat transfer, mass transfer and electrochemical kinetics. The following assumptions are made:

i. Each subsystem is locally homogeneous; each subsystem is considered as a stirred tank.

ii. The electron hole conductivity is ignored compared to the ionic conductivities (proton and oxygen ion), as the electronic conductivity is one order of magnitude less than those of oxygen ion and proton.

iii. Heat transfer by radiation between the electrodes and the gases in the anode and cathode side channels is ignored. For nonpolar gases, the radiation heat transfer can be ignored since the gases do not emit radiation[93]. Three of the species, O_2, N2 and H_2 are non-radiating, while water vapor is radiating. Due to the low partial pressure of water vapor, the emissivity factor of water vapor is low, and accordingly heat transfer by radiation is negligible in comparison to heat transfer by convection.

iv. All gases are considered as ideal gases.

v. The Fuel cell is adiabatic.

4.2.1 **Electrochemical Submodel**

As illustrated in Figure 4.3, the electrochemical reactions occur in the triple-phase boundary zone where the oxygen-ions/protons, electrons and gas phase are in contact. The hydrogen oxidation and oxygen reduction, result in the formation of protons and oxygen ions, respectively. The two reactions are assumed to be confined to the anode-electrolyte and cathode-electrolyte interfaces, respectively.

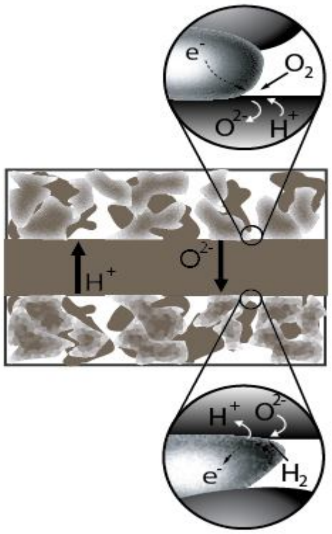

Figure 4.3. Triple phase boundary in a co-ionic conducting SOFC.

Unlike in SOFCs with an oxygen ion-conducting or a proton-conducting electrolyte in which water is produced either in the anode or in the cathode gas channel, in co-ionic conducting SOFCs water is formed in both anode and cathode gas channels. The electrochemical reactions in the anode and cathode sides of a co-ionic conducting SOFC are:

Anode side:

$$H_2 \rightarrow 2H^+ + 2e^- \tag{4.1}$$

$$H_2 + O^{2-} \rightarrow H_2O + 2e^- \tag{4.2}$$

Cathode side:

$$\frac{1}{2}O_2 + 2H^+ + 2e^- \rightarrow H_2O \tag{4.3}$$

$$\frac{1}{2}O_2 + 2e^- \rightarrow O^{2-} \tag{4.4}$$

As mentioned earlier, the reaction scheme shows the flow of both proton and oxygen ions across the electrolyte layer.

Based on our second assumption that the electron hole conductivity is negligible compared to the ionic conductivities (proton and oxygen ion), we propose the cell equivalent circuit shown in Figure 4.4. The circuit includes an electromotive force due to the oxygen ion current serially connected to the corresponding polarization resistance (charge transfer, ohmic and diffusion resistances), and these two elements are parallel connected to two similar elements related to the proton current.

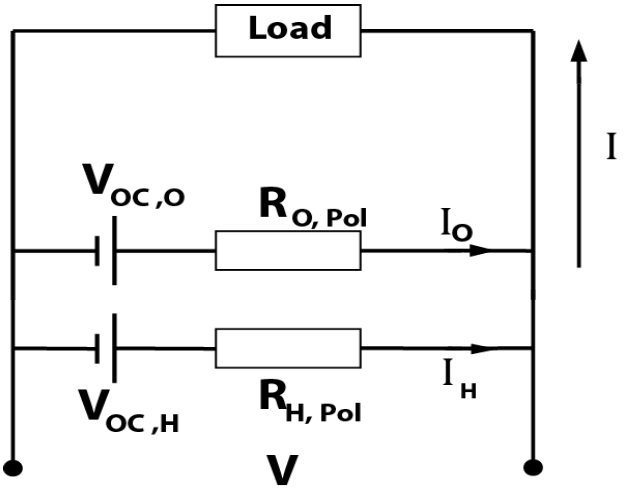

Figure 4.4. Equivalent circuit of the fuel cell.

The Nernst equation is used to calculate the reversible cell voltages, $V_{OC,O}$ and $V_{OC,H}$:

$$V_{OC,O} = E^0 - \frac{RT_S}{nF} ln\left(\frac{p_{H_2O}^{bulk,an}}{p_{H_2}^{bulk} p_{O_2}^{bulk0.5}} \right) \tag{4.5}$$

$$V_{OC,H} = E^0 - \frac{RT_S}{nF} ln\left(\frac{p_{H_2O}^{bulk,cath}}{p_{H_2}^{bulk} p_{O_2}^{bulk0.5}} \right) \tag{4.6}$$

The actual cell voltage is lower than both reversible cell voltages (electric potentials) due to the corresponding activation, ohmic and concentration overpotentials. Using Kirchhoff's voltage and Ohm's laws as well as the equivalent circuit, the cell outlet voltage, *V,* is calculated from:

$$V = V_{OC,O} - R_{O,Pol} I_O \tag{4.7}$$

$$V = V_{OC,H} - R_{H,Pol} I_H \tag{4.8}$$

where

$$R_{O,Pol} I_O = \eta_{an,O} + \eta_{cath,O} + \rho_{E,O} d_E \frac{I_O}{LB} + \eta_{conc,O} \tag{4.9}$$

$$R_{H,Pol} I_H = \eta_{an,H} + \eta_{cath,H} + \rho_{E,H} d_E \frac{I_H}{LB} + \eta_{conc,H} \tag{4.10}$$

$\eta_{an,H}$ and $\eta_{an,O}$ represent the anode activation polarizations related to the reactions in Eqs.4.27 and 4.28, respectively, and $\eta_{cath,H}$ and $\eta_{cath,O}$ are the cathode activation polarizations related to the reactions in Eqs.4.29 and 4.30, respectively. The third terms in Eqs.4.35 and 4.36, $\rho_{E,O}d_EI_O/(LB)$ and $\rho_{E,H}d_EI_H/(LB)$, are the ohmic overpotentials, which represent the resistance of the electrolyte with respect to oxygen ion and proton flows, where $\rho_{E,O}$ ($\rho_{E,H}$) is the oxygen ion (proton) electrolyte resistivity, d_E is the electrolyte thickness, and I_O (I_H) is the oxygen ion (proton) current. As shown in Figure 4.1, the electrolyte resistivity with respect to oxygen ions decreases as the operating temperature increases, and it is typically defined using an Arrhenius type correlation. The protonic conductivity increases very slightly in the range of 700-1000°C, but it starts decreasing with further increase in the operating temperature.

The last terms in Eqs.4.35 and 4.36 represent the concentration overpotentials (losses), which account for the potential losses due to the difference between the concentrations of each species in the bulk and the triple phase boundary. This voltage loss is the difference between the Nernst potentials in the bulk and the triple phase boundary[54]:

$$\eta_{conc,O} = \frac{RT}{nF} ln\left(\frac{p_{H_2}^{bulk} \, {p_{O_2}^{bulk}}^{0.5}}{p_{H_2O}^{bulk,an}} \right) - \frac{RT}{nF} ln\left(\frac{p_{H_2}^{TPB} \, {p_{O_2}^{TPB}}^{0.5}}{p_{H_2O}^{TPB,an}} \right) \tag{4.11}$$

$$\eta_{conc,H} = \frac{RT}{nF} ln\left(\frac{p_{H_2}^{bulk} \, {p_{O_2}^{bulk}}^{0.5}}{p_{H_2O}^{bulk,cath}} \right) - \frac{RT}{nF} ln\left(\frac{p_{H_2}^{TPB} \, {p_{O_2}^{TPB}}^{0.5}}{p_{H_2O}^{TPB,cath}} \right) \tag{4.12}$$

By applying the Kirchhoff's current law, the total current, I, is the sum of the currents I_O and I_H (flux of oxygen ions and protons). I_O and I_H are described by Butler-Volmer equation for the anode and cathode sides[79, 96]:

$$\frac{I_O}{LB} = \gamma^A p_{H_2}^{TPB} p_{H_2O}^{TPB,an} \exp\left(\frac{-E^A}{RT_s} \right) \left\{ exp\left(\theta_a^A \frac{F}{RT_s} \eta_{an,O} \right) - exp\left(-\theta_c^A \frac{F}{RT_s} \eta_{an,O} \right) \right\} \tag{4.13}$$

$$\frac{I_O}{LB} = \gamma^C p_{O_2}^{TPB0.25} \exp\left(\frac{-E^C}{RT_s} \right) \left\{ \exp\left(\theta_a^C \frac{F}{RT_s} \eta_{cath,O} \right) - \exp\left(-\theta_c^C \frac{F}{RT_s} \eta_{cath,O} \right) \right\} \tag{4.14}$$

$$\frac{I_H}{LB} = i_{0,an} \left\{ \exp\left(\alpha \frac{2F}{RT_s} \eta_{an,H} \right) - \exp\left(-(1-\alpha) \frac{2F}{RT_s} \eta_{an,H} \right) \right\} \tag{4.15}$$

$$\frac{I_H}{LB} = i_{0,cath} \left\{ \exp\left(\alpha \frac{2F}{RT_s} \eta_{cath,H} \right) - exp\left(-(1-\alpha) \frac{2F}{RT_s} \eta_{cath,H} \right) \right\} \tag{4.16}$$

where θ is the charge transfer coefficient and α is the symmetry factor, which is an indicator of the symmetry of the activation barrier[112].

At high current densities, mass-transport is the dominant cause in lowering the cell potential. This is because the concentration of the species in the electrode-electrolyte interface is different from the bulk and their values depend on the rate of mass transfer.

4.2.2 **Heat Transfer Sub-model**

Energy balances are written for the anode and cathode gas channels as well as the solid part of the cell. For the cathode and anode gas channels, the enthalpies of inlet fuel and air streams, heat transfer by convection between the gas channels and the solid part, and the enthalpies of outlet fuel and air streams are accounted for. The governing equations for heat transfer in SS1 and SS5 are as follow:

$$\left(LBW\right)\frac{d(c_{fuel}^{an}C_{p\,fuel}^{\;an}T_{an})}{dt}= \\ \dot{n}_{fuel,in}^{an}H_{fuel,in}^{an}-v_{fuel}^{an}c_{fuel}^{an}H_{fuel}^{an}\left(BW\right)+h_{an}\left(T_s-T_{an}\right)\left(LB\right)-N_{H_2}H_{H_2}^{an}\left(LB\right)+N_{H_2O,an}H_{H_2O}^{an}\left(LB\right) \tag{4.17}$$

$$\left(LBW\right)\frac{d(c_{air}^{cath}C_{pair}^{\;cath}T_{cath})}{dt}= \\ \dot{n}_{air,in}^{cath}H_{air,in}^{cath}-v_{air}^{cath}c_{air}^{cath}H_{air}^{cath}\left(BW\right)+h_{cath}\left(T_s-T_{cath}\right)\left(LB\right)-N_{o_2}H_{o_2}^{cath}\left(LB\right)+N_{H_2O,cath}H_{H_2O}^{cath}\left(LB\right) \tag{4.18}$$

where h_{an} and h_{cath} are the convective heat transfer coefficients for the fuel and the air streams, respectively. With the assumption of laminar boundary layer, the values of heat convection coefficients are calculated using the mean Nusselt number[81]:

$$Nu_{air}=\frac{h_{cath}L}{k_{air}}=0.664Pr_{air}^{\frac{1}{3}}Re_{air\,L}^{\frac{1}{2}} \tag{4.19}$$

$$Nu_{fuel}=\frac{h_{an}L}{k_{fuel}}=0.664Pr_{fuel}^{\frac{1}{3}}Re_{fuel\,L}^{\frac{1}{2}} \tag{4.20}$$

The energy conservation equation for the solid phase accounts for the flow of heat in and out through the transport of reactants to the reaction sites and transport of products (water from the anode side and cathode side triple phase boundary) to the gas channel, respectively, as well as the convective heat transfer between the solid part and the fuel and air streams, and the electric power supplied to the external load. The energy balance equation is:

$$\left(d_A + d_E + d_C\right)\rho_s \hat{C}_{ps}\frac{dT_s}{dt} = \Delta H_R - V_{cell}\frac{I}{LB} + h_{an}(\mathrm{T}_{\mathrm{an}} - \mathrm{T}_{\mathrm{s}}) + h_{cath}(\mathrm{T}_{\mathrm{cath}} - \mathrm{T}_{\mathrm{s}}) \quad (4.21)$$

where

$$\Delta H_R = N_{O_2}H_{O_2}^{cath} + N_{H_2}H_{H_2}^{an} - N_{H_2O,cath}H_{H_2O}^{cath} - N_{H_2O,an}H_{H_2O}^{an}$$

4.2.3 Mass Transfer Sub-model

The mass balances on hydrogen, water and oxygen in each subsystem of the cell are written. The mass balance on water should be written for both anode- and cathode-side triple phase boundary zones. In the triple phase boundary zone, the accumulation term is equal to the difference between the molar flux of species and the rate of the electrochemical reaction, which depends on the cell current. At steady state, the rate of reaction and the molar flux are equal. The mass balance equations for the three different species in the triple phase boundary zones are:

$$\frac{\Delta_{cath}}{R}\frac{d}{dt}\left(\frac{p_{O_2}^{TPB}}{T_s}\right) = N_{O_2} - \frac{1}{LB}R_{O_2} \quad (4.22)$$

$$\frac{\Delta_j}{R}\frac{d}{dt}\left(\frac{p_{H_2O}^{TPB,j}}{T_s}\right) = -N_{H_2O,j} + \frac{1}{LB}R_{H_2O,j} \quad (4.23)$$

where $j = cath,\ an$.

$$\frac{\Delta_{an}}{R}\frac{d}{dt}\left(\frac{p_{H_2}^{TPB}}{T_s}\right)=N_{H_2}-\frac{1}{LB}R_{H_2} \tag{4.24}$$

where R_{H_2} and R_{O_2} are the rates of consumption of hydrogen and oxygen, respectively, and R_{H_2O} is the rate of generation of water by the electrochemical reactions, obtained from Faraday's law:

$$R_{H_2O,cath}=\left(\frac{1}{2F}\right)I_H \tag{4.25}$$

$$R_{H_2O,an}=\left(\frac{1}{2F}\right)I_O \tag{4.26}$$

$$R_{H_2}=\left(\frac{1}{2F}\right)I \tag{4.27}$$

$$R_{O_2}=\left(\frac{1}{4F}\right)I \tag{4.28}$$

N_j is the molar flux of species j transferred from the gas channel into the diffusion layer or vice versa. The mass flux of the diffusing species can be defined in terms of the mass transfer coefficient using:

$$N_{O_2}=k_{O_2}^{cath}\left(c_{air}^{cath}y_{O_2}^{cath}-\frac{p_{O_2}^{TPB}}{R\mathrm{T_s}}\right) \tag{4.29}$$

$$N_{H_2}=k_{H_2}^{an}\left(c_{fuel}^{an}y_{H_2}^{an}-\frac{p_{H_2}^{TPB}}{R\mathrm{T_s}}\right) \tag{4.30}$$

$$N_{H_2O,cath}=k_{H_2O}^{cath}\left(-c_{air}^{cath}y_{H_2O}^{cath}+\frac{p_{H_2O}^{TPB,cath}}{R\mathrm{T_s}}\right) \tag{4.31}$$

$$N_{H_2O,an}=k_{H_2O}^{an}\left(-c_{fuel}^{an}y_{H_2O}^{an}+\frac{p_{H_2O}^{TPB,an}}{R\mathrm{T_s}}\right) \tag{4.32}$$

where k_j is the mass transfer coefficient of species j and its value is calculated as explained in Chapter 4, 4.2.3.

Mass conservation for species in the gas channels account for mass transfer with the inlet and outlet gas streams, and the transfer of the reactant species from the gas channel to the diffusion layer and product vice versa. The following equations describe mass transfer in the cathode and anode gas channels:

$$LBW\frac{dc_{air}^{cath}}{dt}=\dot{n}_{air,in}^{cath}-v_{air}^{cath}c_{air}^{cath}WB-N_{o_2}LB+N_{H_2O,cath}LB \tag{4.33}$$

$$LBW\frac{d(c_{air}^{cath}\,y_{o_2}^{cath})}{dt}=\dot{n}_{air,in}^{cath}y_{o_{2,in}}-v_{air}^{cath}c_{air}^{cath}\,y_{o_2}^{cath}WB-N_{o_2}LB \tag{4.34}$$

$$LBW\frac{d(c_{air}^{cath}\,y_{H_2O}^{cath})}{dt}=-v_{air}^{cath}c_{air}^{cath}\,y_{H_2O}^{cath}WB+N_{H_2O,cath}LB \tag{4.35}$$

$$LBW\frac{dc_{fuel}^{an}}{dt}=\dot{n}_{fuel,in}^{an}-v_{fuel}^{an}c_{fuel}^{an}WB-N_{H_2}LB+N_{H_2\mathrm{O,an}}LB \tag{4.36}$$

$$LBW\frac{d(c_{fuel}^{an}y_{H_2}^{an})}{dt}=\dot{n}_{fuel,in}^{an}y_{H_{2,in}}-v_{fuel}^{an}c_{fuel}^{an}y_{H_2}^{an}WB-N_{H_2}LB \tag{4.37}$$

Eqs.4.33, 4.34 and 4.35 are for the cathode gas stream and represent an overall mole balance for the air stream, an O_2 mole balance, and a H_2O mole balance, respectively. Similarly, Eqs.4.36 and 4.37 are fuel stream and hydrogen mole balances, respectively. The model parameter values are listed in Table 4-1.

Table 4-1. Fuel cell model parameter values.

parameter	value	source
A_Ω	1.06036	[100]
B	0.005 m	This work
B_Ω	0.15610	[100]
C_Ω	0.19300	[100]
D_Ω	0.47635	[100]
E_Ω	1.03587	[100]
E^A	253648 J mol^{-1}	This work
E^C	198954 J mol^{-1}	This work
F_Ω	1.52996	[100]

G_{Ω}	1.76474	100
H_{Ω}	3.89411	100
L	0.01 m	This work
$T_{\mathrm{air,in}}^{\mathrm{cath}}$	890 K	This work
$T_{\mathrm{fuel,in}}^{\mathrm{an}}$	890 K	This work
W	5×10^{-3} m	This work
d_A	5×10^{-5} m	96
d_C	5×10^{-5} m	96
d_E	5×10^{-4} m	106
$i_{0,an}$	1330 A m^{-2}	This work
$i_{0,cath}$	1330 A m^{-2}	This work
$\dot{n}_{\mathrm{air,in}}^{\mathrm{cath}}$	5.6×10^{-6} mol s^{-1}	113
$\dot{n}_{\mathrm{fuel,in}}^{\mathrm{an}}$	5.6×10^{-6} mol s^{-1}	113
α	0.5	96
$\rho_s \tilde{C}_{ps}$	10^6 J $m^{-3}K^{-1}$	56
γ^A	3.7×10^7 A m^{-2}	This work
γ^C	1.5×10^9 A m^{-2}	This work
θ_a^A	2	79
θ_c^A	1	79
θ_a^C	1.4	79
θ_c^C	0.6	79
Δ_{an}	5×10^{-6}m	This work
Δ_{cath}	5×10^{-6}m	This work
ε_{cath}	4×10^{-1}	96
ε_{an}	4×10^{-1}	96
τ_{an}	5	96
τ_{cath}	5	96
δ_{an}	5×10^{-7}	80
δ_{cath}	5×10^{-7}	80
υ_{H_2}	7.07	81
υ_{O_2}	16.6	81
υ_{N_2}	17.9	81
υ_{H_2O}	12.7	81
σ_{H_2}	2.968	114

σ_{O_2}	3.433	[114]
σ_{H_2O}	2.65	[114]
σ_{N_2}	3.681	[114]
$y_{O_{2,\text{in}}}$	0.2	This work
$y_{N_{2,\text{in}}}$	0.8	This work
$y_{H_{2,\text{in}}}$	0.97	This work
$y_{\mathrm{H_2O_{in}}}$	0.03	This work

4.3 Simulation Method

The prediction of the current-voltage (I-V) curve of the cell is one of the aims of this study. The I-V curve of the cell is usually obtained by linear sweep voltammetery using a potentiostat. This experiment is generally conducted in an isothermal furnace, thus isothermal condition can be assumed[115]. To simulate the I-V curve, energy balance equations are omitted from the model and all temperatures in the remainder of the model are set to the constant temperature at which the experiment was conducted. Under steady-state conditions, the right hand sides of all governing differential equations are zero, and therefore the system is a set of algebraic equations. The MATLAB routine `fsolve` is used to find the root(s) of these algebraic equations. At a given cell voltage (applied potential of the potentiostat), we solve the set of coupled algebraic equations to find the corresponding cell current. By repeating this step for different cell voltages, we are able to generate the polarization curve.

To investigate the steady-state behavior of the system, the model is solved under non-isothermal conditions to capture the effects of heat production. To examine the presence of steady-state multiplicity, as in reaction engineering, the heat production and heat generation rates are plotted. The intersection points of the two plots represent the steady-states of the system. Bifurcation analysis is conducted under four operating modes: fixed ohmic load, potentiostatic, galvanostatic and fixed cell power density (with bifurcation parameters being the external load resistance, cell voltage, cell current and cell power density, respectively). The inlet fuel and air flow rates are also considered as bifurcation parameters. To plot bifurcation diagrams, the nonlinear equations are solved as each bifurcation parameter is varied. For a given value of a bifurcation parameter, a numerical root finding method can find one steady state value depending on the chosen initial guess. One way to capture all the steady state values is to find the roots by systematically varying the initial guess. This method is not efficient, as it needs many trials and errors. On the other hand, for a given solid temperature, one load resistance always exists. Therefore, if we solve the algebraic equations for a given value of solid temperature rather than the external load resistance, one suitable initial guess is adequate to systematically find all steady states.

The MATLAB routine `fsolve` is used to solve this set of nonlinear algebraic equations. After a solution is obtained for a given value of the solid temperature, for the next value of the solid temperature, the initial guess vector is chosen to be the root corresponding to the previous value of the solid temperature (zero order continuation). This approach reduces the convergence time and the number of numerical errors.

4.4 Parameter Estimation and Model Validation

The polarization curve predicted by the model is validated using the experimental data of Iwahara et al.[106] obtained under isothermal operation at 1273 K. Figure 4.5 shows the experimental data and the model predictions.

The unknown parameters, $i_{0,an}$, $i_{0,cath}$, γ^A, γ^C, E^A and E^C are estimated from the experimental data. The exchange current densities, $i_{0,an}$ and $i_{0,cath}$ are assumed to be equal. To estimate the parameters, the MATLAB routine `fminsearch,` which is based on the Nelder-Mead simplex algorithm, is used to locate the parameter values that minimize the following objective function:

$$J\left(\vec{\Delta}\right) = \sum_{i=1}^{i=n} (I_{mod,i}(\vec{\Delta}) - I_{mea,i})^2 + (V_{mod,i}(\vec{\Delta}) - V_{mea,i})^2 \qquad (4.38)$$

where

$$\vec{\Delta} = (\gamma^A, \gamma^C, E^A, E^C, i_0)$$

$I_{mod,i}$ and $I_{mea,i}$ are model predicted and experimental values of the cell current, respectively, and $V_{mod,i}$ and $V_{mea,i}$ are model predicted and experimental values of cell voltage, respectively. Estimated values of the six model parameters are given in Table 4-1.

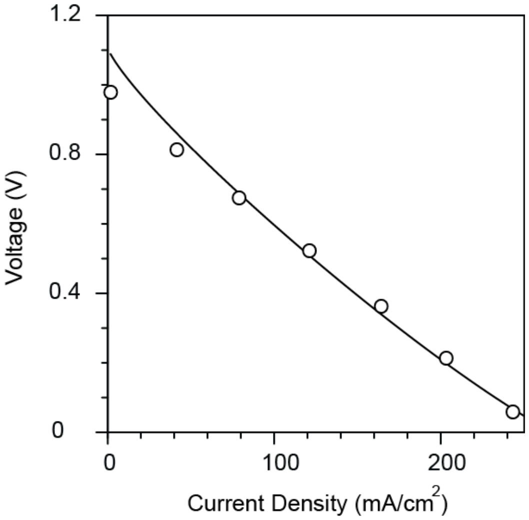

Figure 4.5. The I-V curve of the fuel cell at 1273 K (circles = experimental data[106], solid line = model prediction).

4.5 Steady State Behavior

Prior to this work, no study on steady-state multiplicity in co-ionic-conducting SOFCs was reported. Detailed steady-state analysis of this type of cells is indispensible to determine whether steady-state multiplicity in the cell temperature can occur.

Under non-isothermal conditions, the fuel cell model consists of twelve ordinary differential and six nonlinear algebraic equations; it reduced to eighteen algebraic equations under steady-state conditions. Figure 4.6 depicts the heat generation and heat removal terms versus the solid temperature. The inlet cathode and anode channel gas temperatures are 890 K. As can be seen in Figure 4.6(a), Q_P curve intersects Q_R line at three points when the applied load resistance is 2.6 Ω. As the load resistance is increased from 2.6 to 5 Ω, the cell current and consequently the heat generation rate decrease, and the heat generation and heat removal rates intersect at one point only, which presents a unique steady state. When the load resistance is 2.6 Ω, the lower and upper steady states are stable and the middle one is unstable.

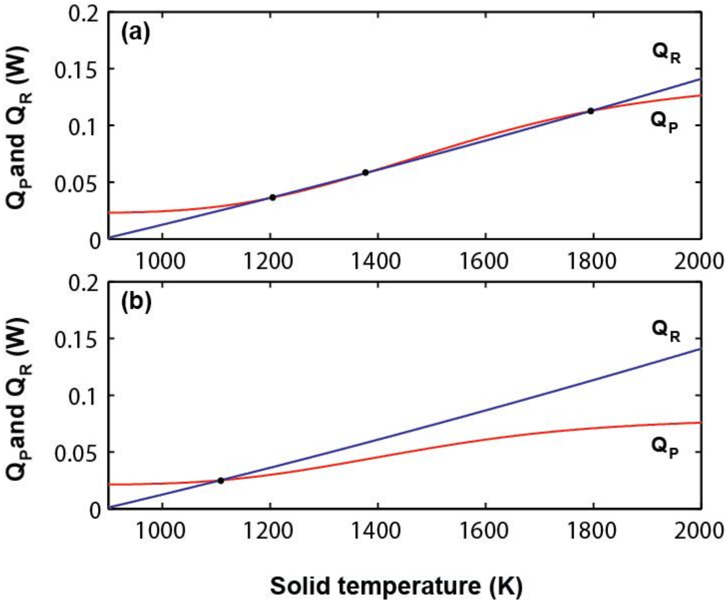

Figure 4.6. Steady-state heat removal and heat generation under two different external load resistances, (a) 2.6 Ω and (b) 5 Ω.

The bifurcation analysis is conducted under fixed ohmic load operation. In this case, the bifurcation parameter is the external load resistance. Figure 4.7 shows the bifurcation diagram of the solid temperature versus the load resistance. It can be seen that there is a region of three steady states between 2.4 and 2.8 Ω. Points A and C are the ignition and extinction points, respectively. At point A (ignition point), a small decrease in the load resistance leads to a jump in the cell temperature to the upper branch temperature, point B. The ignition phenomenon can have detrimental effects on the cell system; sudden large changes in the solid temperature can ruin the balance of plant components. Mole fractions of different species in the anode and cathode gas channels versus the bifurcation parameter, the load resistance, are shown in Figure 4.8. It can be observed that concentration and temperature multiplicities coexist. The bifurcation curves for reactant species, O_2 and H_2, and water formed at the cathode side are in the form of a S-shaped curve, while that of the water formed at the anode side, is in the form of an inverse S-shaped curve. Figure 4.9 shows the cusp catastrophe steady-state manifold. One can observe that at higher inlet gas temperatures the multiple steady state region disappears. The multiplicity region can be detected by projecting the turning points (ignition and extinction points) locus onto the parameter space. Figure 4.10 shows the cusp shape (shaded area) presenting the region of three steady states.

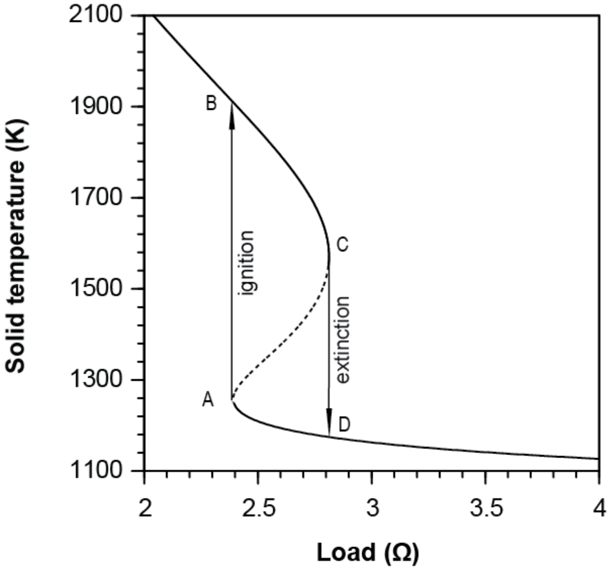

Figure 4.7. Bifurcation diagram (fixed ohmic load mode of operation).

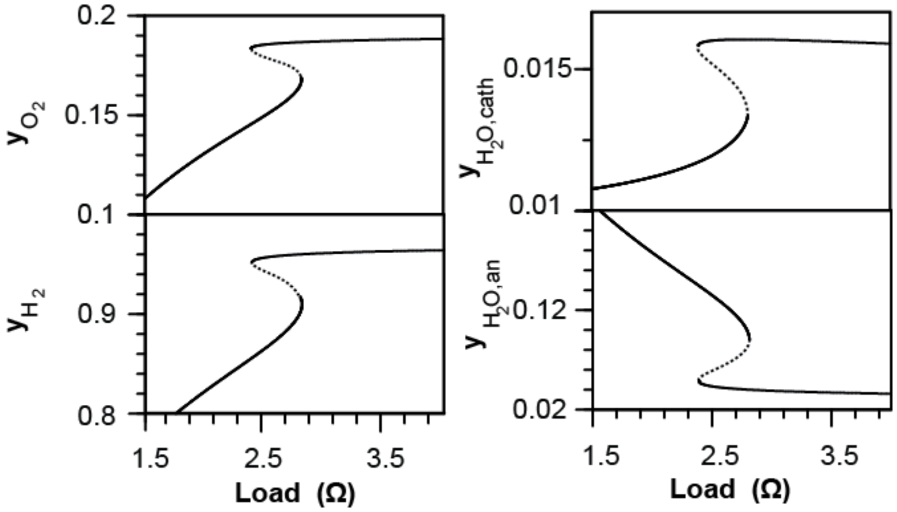

Figure 4.8. Bifurcation analysis under fixed ohmic load: species mole fractions (y_{O_2} , y_{H_2} , $y_{H_2O,cath}$ and $y_{H_2O,an}$) in the gas channels.

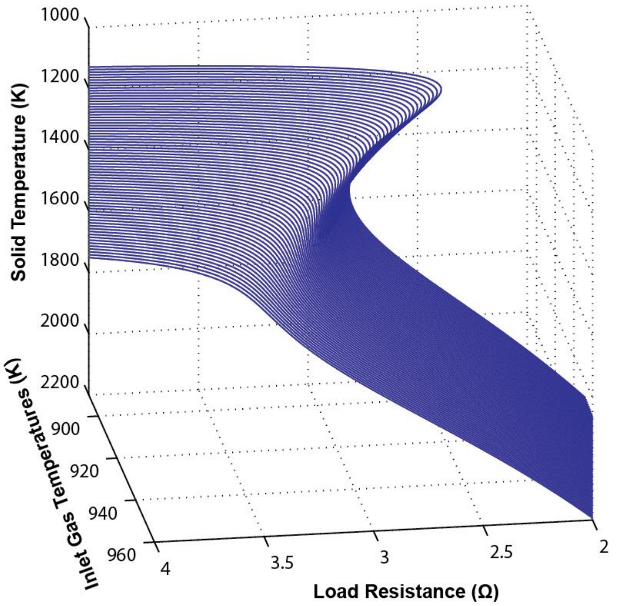

Figure 4.9. The bifurcation manifold of the cusp catastrophe: T_S versus R_{load} and the inlet gas temperatures

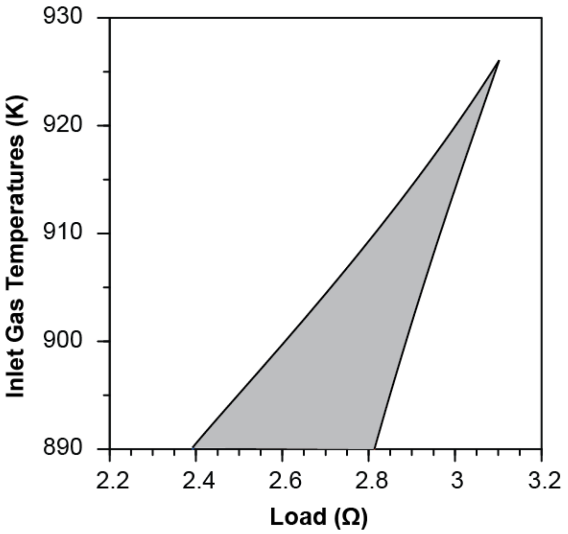

Figure 4.10. Multiplicity region in the fixed ohmic load mode.

The bifurcation diagram can be drawn with respect to the cell power density instead of the load resistance as shown in Figure 4.7. Figure 4.11 shows the bifurcation diagram of the solid temperature versus the cell power density. For given cell operating conditions, the cell power is maximum at a certain ohmic load. The range of the load power is 0-160 mW/cm^2 for the single cell under study. The effect of fuel and air flow rates is shown in Figure 4.12. As can be seen, the range of the load resistance within which the multiplicity exists widens as the inlet fuel and air flow rate increases, and the inverse S-shaped curve moves toward lower values of the load resistance. The increase in the flow rates decreases the anode and cathode channel gas temperatures and hence increases the heat dissipation by convection. Thus, the load resistance should decrease to compensate for the increase in the amount of heat dissipation. Under four operation modes of fixed ohmic load resistance, galvanostatic, potentiostatic and fixed cell power density, the bifurcation diagrams of solid temperature versus the inlet fuel and air flow rates are shown in

Figure 4.13. As can be seen, in the galvanostatic mode, there is a monotonic relationship between the solid temperature and the cell current, while under the three other modes, presence of multiple steady states can be observed.

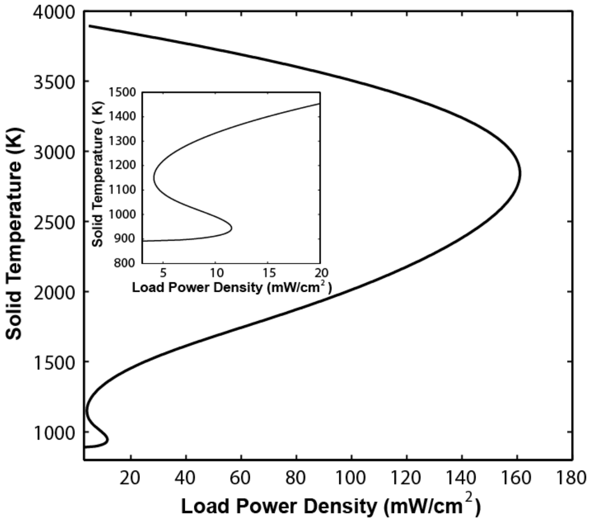

Figure 4.11. Solid temperature versus load power density.

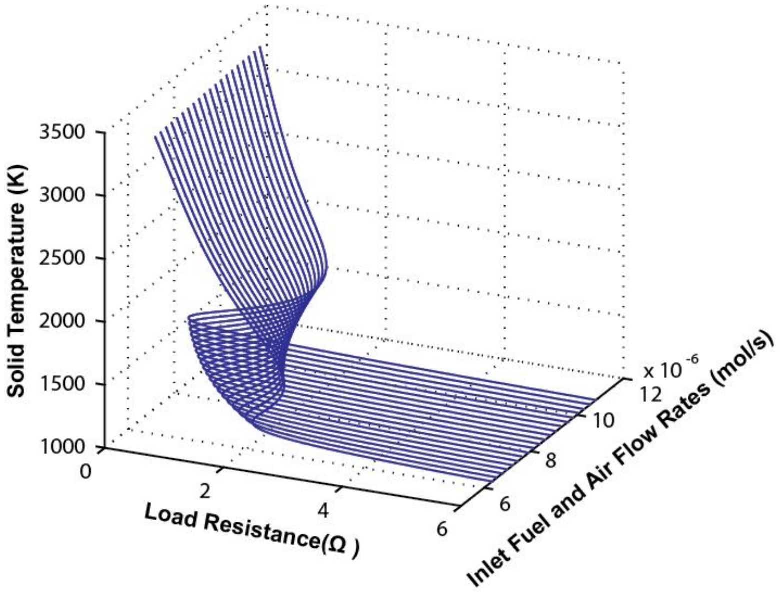

Figure 4.12. Solid temperature versus the load resistance and equal inlet fuel and air flow rates.

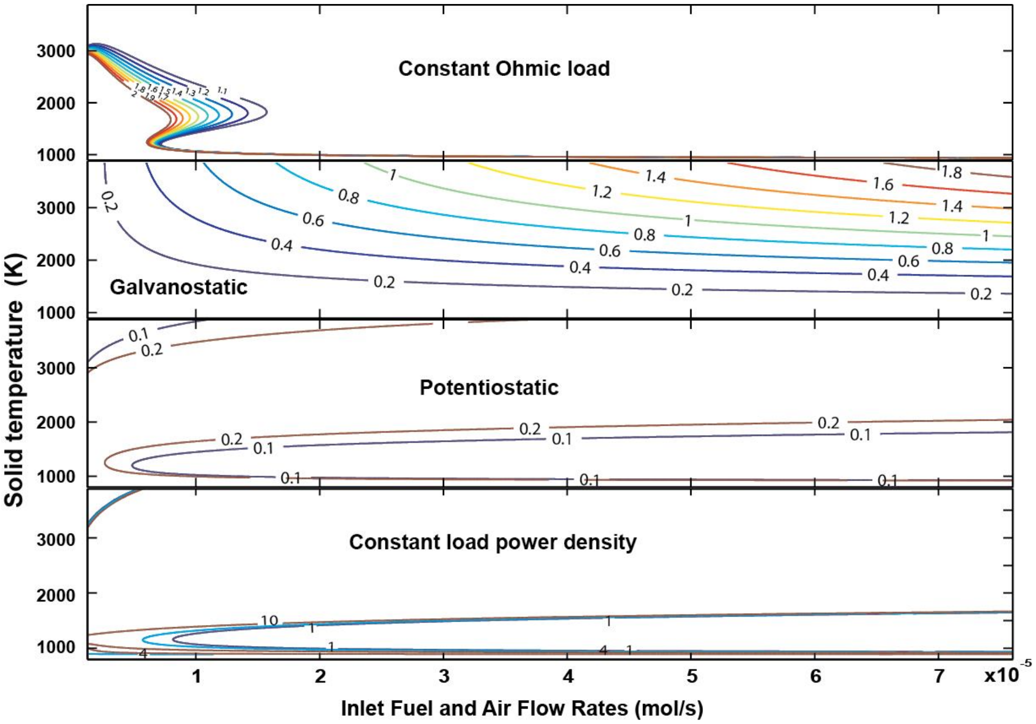

Figure 4.13. Bifurcation diagrams: solid temperature versus equal inlet fuel and air flow rates under four different operation modes of fixed ohmic load, galvanostatic, potentiostatic and fixed load power density.

The steady state multiplicity is also studied under potentiostatic mode (fixed cell voltage). This mode of operation requires voltage control and is used to characterize a cell. In this case, the cell voltage is the bifurcation parameter. Figure 4.14 shows the bifurcation diagram drawn by plotting steady state solid temperature as a function of cell voltage at equal inlet gas temperatures of 890 K. One can observe that more than one steady state exist in certain potential regimes. The middle one of the three steady states, shown by dashed line, is unstable.

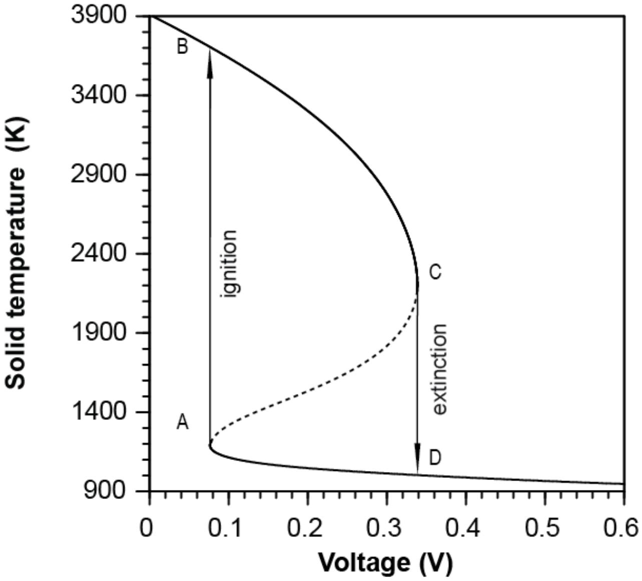

Figure 4.14. Bifurcation diagram: solid temperature versus cell voltage.

In the galvanostatic operation mode, the cell current is under control (is bifurcation parameter). As shown in Figure 4.15, there is a unique steady state for all species concentrations, outlet gas temperatures and cell temperature. This result is in agreement with that of an oxygen ion-conducting SOFC[56, 116].

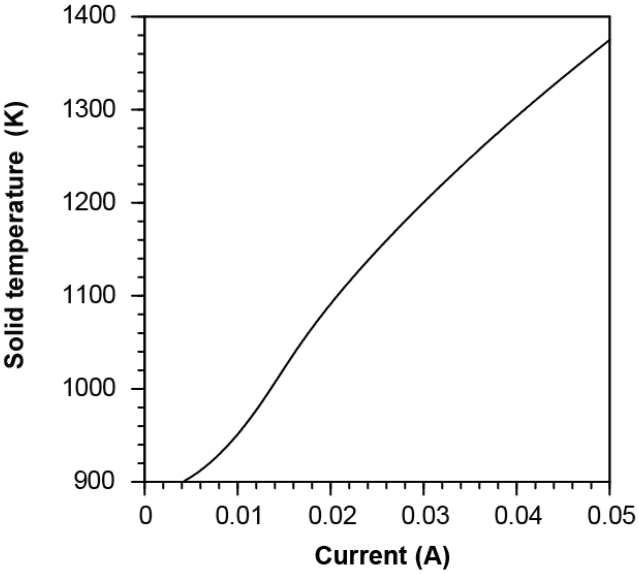

Figure 4.15. Solid temperature versus cell current.

4.6 Concluding Remarks

A mathematical model was developed to investigate the presence of multiplicity in a co-ionic conducting SOFC. Simulation results showed that a multiple steady state region exists in this type of SOFCs. Ignition and extinction phenomena in the solid temperature and outlet gas concentrations were observed. This result is in agreement with behavior reported for oxygen ion-conducting SOFCs and proton-conducting SOFCs, attributing the existence of multiplicity to the dependence of the electrolyte oxygen ion/proton conductivity to the electrolyte temperature. Under fixed ohmic load and potentiostatic operations, it was found that concentration and temperature multiplicities coexist. Ignition and extinction behavior in the cell temperature is opposite to that of the reactants concentration. While the reactants concentrations and water product at the cathode side are under ignition, the cell temperature and the water product concentration at the anode side are in the extinction branch and vice versa.

When the cell power density is the bifurcation parameter, the presence of steady state multiplicity was found. This multiplicity can pose a challenge when power control is needed. Also, the effect of inlet fuel and air flow rates on the presence of steady state multiplicity was investigated. It was shown that as the inlet fuel and air flow rates increase, the region of steady-state multiplicity expands and shifts towards lower values of load resistance.

Notation

C_p= specific heat capacity (J mol^{-1} K^{-1})

$\hat{C}_{ps}$= specific heat capacity of the solid (J kg^{-1} K^{-1})

d_A= thickness of anode (m)

d_C= thickness of cathode (m)

d_E= thickness of electrolyte (m)

F = Faraday constant (A s mol^{-1})

h= heat transfer coefficient (W m^{-2} K^{-1})

H= enthalpy (J mol^{-1})

ΔH_R= enthalpy change of the overall reaction (J mol^{-1})

I= cell current (A)

$i_{0,an}$= exchange current density at anode (A m^{-2})

$i_{0,cath}$= exchange current density at cathode (A m^{-2})

L= length of cell (m)

$\dot{n}$= molar flow rate (mol s^{-1})

T= temperature (K)

V_{cell}= cell voltage (V)

v= velocity (m s^{-1})

W= width of gas channels (m)

y_j= mole fraction of species j

Greek Letters

α = symmetric factor

δ = pore mean radius (m)

Δ = thickness of the diffusion layer (m)

ε_{an}= porosity of anode

ε_{cath}= porosity of cathode

ε_{ii} = the characteristic Lennard-Jones energy (J)   j, i: H_2, H_2O, O_2, N_2

η_{conc} = concentration overpotential (V)

η_{an} = anode activation overpotential (V)

η_{cath} = cathode activation overpotential (V)

θ= charge transfer coefficient

ρ = resistivity (Ω m)

ρ_s = density of the solid (kg m^{-3})

σ_{ji} = characteristic length (Å)   j, i: H_2, H_2O, O_2, N_2

τ = tortuosity

Ω_D = diffusion collision integral

Subscripts

an	anode
cath	cathode
E	electrolyte
S	solid

Superscripts

TPB	triple phase boundary

5 Chapter 5: Dye Sensitized Solar Cell Background and Literature Review

5.1 Introduction

The global demand for energy is estimated to be doubled in the next two decades. Currently, the needed energy is coming from fossil fuels. However, these fuels pose a major environmental challenge as the combustion gases such as CO_2 are a threat for the future of the planet. The energy and environmental challenges have motivated a major quest for cleaner, renewable energy resources, in particular solar energy, which is abundant and free. An interesting photovoltaic technology is that of dye sensitized solar cells (DSCCs), which relies on a semiconductor/liquid junction, has evolved quite rapidly to a point that currently its module is undergoing commercialization. Dye sensitized solar cells with acceptable efficiency first introduced by Michael Grätzel and Brian O'Regan[117], and later efforts resulted in increasing the efficiency of this design up to 11%. Lately, devices in the lab scale with efficiency as high as 12.3% are fabricated[117-118]. To be successful in commercialization of this technology and making a flourishing market, the total cost of the cell needs to be reduced based on the obtained current efficiency [119-120]. However, a higher efficiency DSSC can address this issue and make the extensive commercialization of this technology possible[121]. Here, we briefly describe the DSSC working principle and components. Further details of this system can be found elsewhere[122].

5.2 DSSC Working Principle

Figure 5.1 depicts a schematic of a DSSC. The main components of a DSSC are a transparent conductive oxide (TCO) electrode, a wide band gap semiconductor which is the electron acceptor, chromophore sensitizer that is the light absorption layer, a hole conductor media which can be a solid state or liquid-based redox solution, and a counter electrode to complete the circuit.

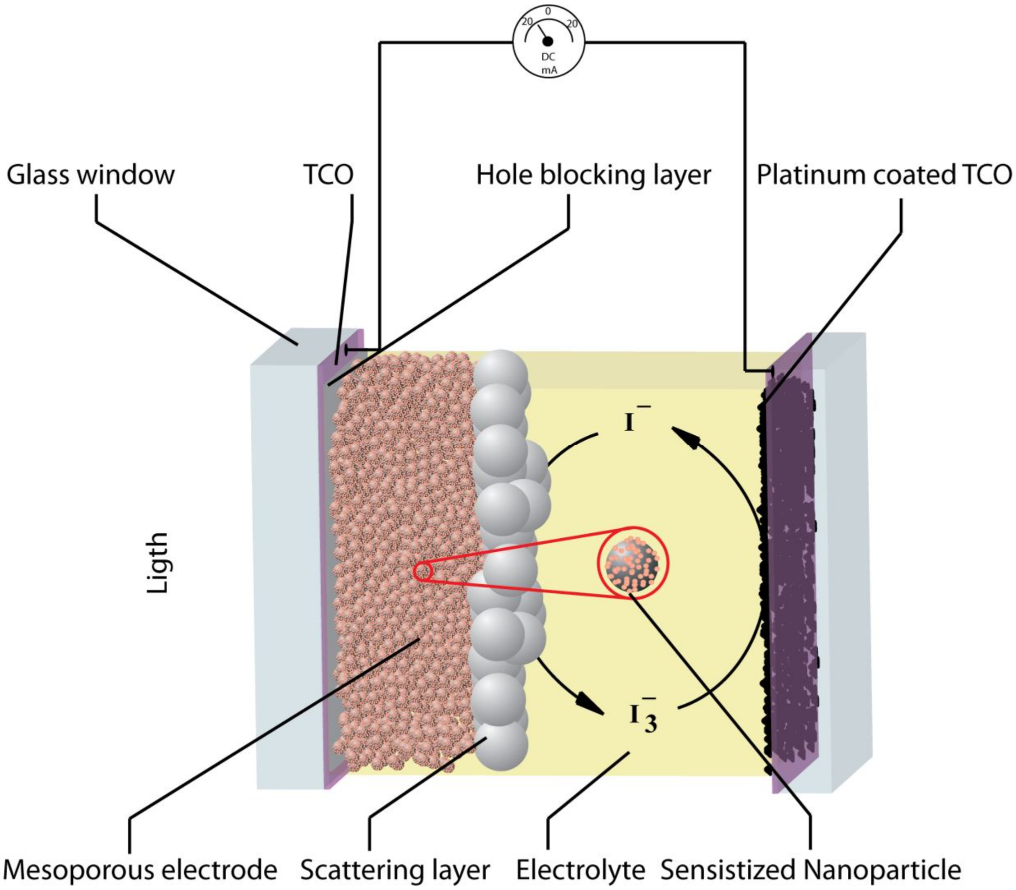

Figure 5.1. Schematic of a DSSC.

The electrodes in the DSSC are made of a transparent conductive oxide (TCO), which has a typical transparency around 85-95 %[123]. Fluorine doped tin oxide (SnO2:F) is the most widely used oxide; it is typically deposited by spray pyrolysis at different thicknesses on a glass substrate 300-800 nm). The conductivity and transparency of the oxide layer are inversely correlated, and the typical electrode conductivity of the layer is around 8-15 Ω/□. Transparent conductive electrodes (TCE) are mostly a wide band gap semiconductor that along with the TCO and the sensitizer chromophore forms the photanode of the cell. A wide range of oxides e.g. TiO2, ZnO, SnO2 and Nb2O5 can be suitable for this purpose[124]. Among different oxides the mesopourous TiO2 in the anatase form (has acceptable electron mobility) is the most commonly used electrode. Since this oxide mostly absorbs light in the UV range of the solar spectrum, decorating the oxide with a sensitizer chromophore with efficient optical absorption into near infrared range is the initial step into the more efficient light harvesting. Obviously, having more dye means more light absorption, however the cell is not efficient in the multilayer adsorption as the electronic pathway for injecting the photogenerated electron does not exist. To have higher efficiency, higher surface area that can accommodate more dye molecule within the same working volume in a monolayer adsorbed fashion is needed. This requirement has led researchers to produce interconnected networks of TCEs with high internal surface area[117, 125]. As mentioned the cell efficiency has direct correlation with the dye absorption spectrum. Also, it should be noted that the energetic alignment of the sensitizer at the interface needs to be in accordance with the rest of the cell to make the electron and hole transfer pathways viable and the charge dissociation efficient at the interface. The latter will pose limitation on the choice of the dye molecules A large number of sensitizer molecules with different absorption coefficients are available, and efforts are currently being made to extend the tail of absorption coefficient further into near IR[126-127].

Upon light illumination on the cell, the photons absorbed into the dye molecule causes the dye to reach its excited state. This excited state can go through relaxation into its initial condition or can inject electrons into the conduction band of the TCE. The oxidized dye needs to recapture an electron in order to go through continuous cycle and can contribute again to the light absorption process. In order not to favor the recombination pathway of the oxidized dye with the electron in the conduction band of TCE, a hole transfer material which in case of conventional DSSC is a redox couple in an organic solvent, donates an electron to the dye and oxidize itself. When choosing a redox couple for this process, due to multiple processes at interface with different time scales the kinetics of the reaction and the mobility of the ions in their solvent are the important parameters to be considered. The equilibrium potential of the redox is another important parameter that can lead into increase in solar cell efficiency by improving the open circuit voltage. Figure 5.2 shows different pathways for photogenerated electrons with the time constant attributed to this phenomenon.

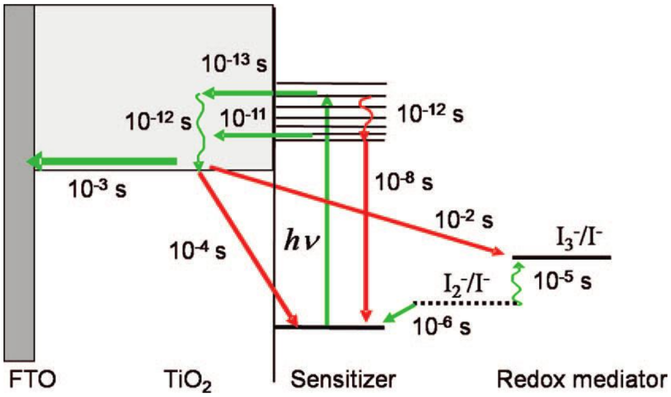

Figure 5.2. Diagram of the operation mechanism and different processes time constants[126].

5.3 Theoretical and Experimental Considerations in a DSSC

In this section, we discuss the processes behind the DSSC operation in detail. The goal of this section is to describe microscopic processes taking place in the cell and how these processes can be represented by mathematical models.

5.3.1 **Light to Electron Conversion**

A delicate component in a DSSC is the sensitizer chromophore that is adsorbed as a monolayer on the semiconductor electrode. It converts light to electrons. This component is the most striking feature of a DSSC. Broadly speaking, the light harvesting efficiency of the cell is a direct function of the optical properties of the dye. Upon illumination, the ground state of the dye is excited to its unrelaxed metal-to-ligand-charge-transfer (MLCT) state. The molecule undergoes relaxation within the manifold of vibronic excited states in tens of femto to a pico second or injects an electron into the semiconductor from any of the unthermalized states. The unrelaxed excitation results in the ultrafast injection and the relaxed state contributes to slower injection processes. This biphasic injection mechanisim was introduced by Asbury and colleagues[128]. When the dye reaches its triplet MLCT, it can decay back to its ground state. The multi step injection processes in a sensitized interface and the energy alignment seem to be key parameters in electron production as the efficiency of the electron injection and overall conversion efficiency needs a precise design of the energetic to avoid possible losses. In order to have an efficient electron injection from the excited state of the dye molecule to the conduction band an offset of about 100-150 mV is needed, although a precise value has not reported yet[129]. The injection efficiency therefore is a sensitive function of the conduction band position relative to the MLCT states of the dye and also to have a very efficient system, we just need enough overpotential for the injection and the extra can be vibrationally and thermally lost. So the design of the molecule at a specific interface and the way the molecule is electronically wired to the surface are very important in optimizing the electron injection. Bear in mind that in a DSSC the environment that the junction is seeing is completely filled with other species and all the adsorption and desorption processes taking place at the interface can lead to a change of surface energy states and consequently to the efficiency of photon to electron conversion. For now let us assume that the electron is produced and injected into the TiO_2 conduction band. The next section explains the transport of electrons.

5.3.2 **Electron Transport in the Semiconducting Oxide**

The DSSC made of the crystalline TiO_2 in the anatase form is the most studied design of DSSC. Typically mesoporous electrodes are being made through the sol-gel process and the layer is being coated on the glass substrate by different techniques including doctor blading, screen printing and spin coating. This method is used for random assemblage of the particles and the particle size are among the parameters that define the pore size, porosity, internal surface area and the light scattering inside the structure[125, 130]. How the electron transports and what the mechanism underlying this transport is are still under debate. The small size of the nanocrystalline colloids will not support an electrical field. So the carrier migration cannot be field assisted. Numerous studies have been performed on the effect of light intensity, carrier density and applied potential on carrier mobility and apparent diffusion of the electron inside the TiO_2 network[126, 131-132]. It is thought that electron does not move between two particles due to the drift but it hops from one particle to the neighboring one[133]. It was further confirmed that the electrical field in the network of TiO_2 in contact with electrolyte in DSSC is not present[132]. Photoconductivity and charge transport in dark and light and in air and vacuum for nanocrystalline network of TiO_2 have also been investigated[131, 134]. The studies have suggested that the charge transport is highly dependent on the surface adsorbed species and electron scavenger present in the media The fact that the electron transport mainly occurs through diffusion led others to believe that it will be a function of density of the states and also density of the trap sites[135]. The bulk traps are assumed to be involved in the electron transport in the nanoporous oxide through trapping-detrapping mechanism with conduction band states and the surface traps seems to be an additional path to transfer electron to the oxidized species in the electrolyte[136]. The electron transfer within titanium network has a significant role in the loss mechanism through the surface traps which has been shown to be a function of light intensity and has been the subject of many studies[137-138]. The dependency of TiO_2 conductivity on applied voltage has been also investigated by electrochemical impedance spectroscopy. The results have indicated that the conductivity of the TiO_2 network can vary over 8 order of magnitude, which suggests an average electron mobility of $2.3x10^{-4}$ [139].

In summary, the electron transport in the DSSC photoanode has not been well understood yet. Effects of electrolyte, light intensity, and trap density have been all enumerated as the sources affecting the electron mobility and carrier diffusion coefficient.

5.3.3 **Electrolyte**

One of the major losses in the dye sensitized solar cell can be attributed to the overpotential that is needed for the regeneration of the dye molecule by iodide in the electrolyte side. This overpotential for the current cell composition is in excess of 600 mV, if being used the cell efficiency would be much higher[121, 140]. The iodide/triiodide reaction in absence of the dye on the surface was the subject of few studies to address the ambiguity of reaction rate and mechanism for the recombination[141]. However, the debate is still ongoing on the reaction mechanism[142]. The importance of knowing the exact mechanism of the iodine reaction at the TiO_2 surface will be significant in the modeling; this is an additional level of complexity due to iodine two step reduction mechanism. To deviate from the iodide/triiodide system some practical consideration should be taken into account.[143] In the recent years different redox couple has been introduced to potentially substitute the iodide/triiodide.[118, 144-145]. Knowing the redox potential and kinetics of the reaction is two pieces of information that are necessary for the modeling purposes. The optical properties of the redox solution will be also useful when detail model with inclusion of the optical loss due to absorption of the redox solution is considered.

5.4 Characterization Techniques

There are different characterization techniques for analysis of solar cells. These techniques allow one to: a) assess the cell performance, b) identify the obstacles related to the stability and reproducibility, c) identify the physical processes behind photo conversion processes and d) optimize new material components and designs. These techniques include steady-state, frequency response and transient measurements.

Albeit steady-state techniques give us a general idea of the generation and collection of charge carriers, details of the charge carrier dynamics are out of the scope of this experiment[146]. With this respect, the time-resolved techniques and frequency methods are very beneficial. In the following section, we review the common measurement techniques for solar cells.

5.4.1 **IV, IPCE and APCE**

The IV curve is the most important characteristics of the DSSC. The overall cell efficiency can be defined using the fill factor (ff), short circuit current (I_{SC}), open circuit voltage (V_{OC}) and the incident light power ($P_{incident}$).

$$\eta = \frac{P_{\max}}{P_{incident}} = \frac{I_{SC} V_{OC} FF}{P_{incident}} \tag{5.1}$$

where the term FF, called the fill factor, is defined by:

$$FF = \frac{P_{\max}}{V_{OC} I_{SC}} = \frac{V_{mp} I_{mp}}{V_{OC} I_{SC}} \tag{5.2}$$

The incident photon to current conversion efficiency (IPCE) also called as the external quantum efficiency is used to describe the operation of the DSSC. It is defined by the product of the three factors η_{LH} (light harvesting efficiency), η_{inj} (injection efficiency) and η_{col} (collection efficacy) and represents the number of electrons corresponding to the photocurrent in the external circuit divided by the monochromatic photon flux[147-148]. IPCE is expressed by:

$$IPCE = \eta_{LH} \eta_{inj} \eta_{col} \tag{5.3}$$

The APCE expresses the absorbed photon to current conversion efficiency and describes the efficiency of the absorbed photons conversion into current. APCE is calculated by dividing the IPCE by the light harvesting efficiency[147].

5.4.2 **Frequency Resolved Methods**

DC techniques do not give any information about internal system dynamics and time constants of different processes, but frequency methods can provide information on the dynamics of internal processes. In this technique, we subject the system to an alternating signal of small magnitude and record the cell response to the applied signal[112]. These techniques are based on applying a sinusoidal perturbation to the incident light, δP and voltage, δV. A small amplitude modulation of potential or light illumination is superimposed on a steady-state DC signal of a constant cell voltage as an example the cell voltage under open circuit condition or a constant background illumination[149].

5.4.2.1 Electrochemical Impedance Spectroscopy

The impedance is calculated as the frequency domain ratio of the voltage to the current[126] and is calculated as follows[150]:

$$Z(\omega) = \frac{v_0 \sin(\omega t)}{I_0 \sin(\omega t + \phi)} = Z_0 \frac{\sin(\omega t)}{\sin(\omega t + \phi)} \tag{5.4}$$

The impedance spectroscopy measurements are commonly represented in the form of Bode plot or Nyquist plot in which log |Z| (amplitude) and φ (phase shift) are plotted versus the frequency or the imaginary part of the impedance is plotted versus the real part respectively. Measurements are usually made over a wide frequency range of about 1mHz to 1MHz.

Different equivalent circuits may lead to the same frequency-dependent impedance response. It should be noted that a priori distinction between degenerate circuits is not trivial[151] and it may bring up different interpretations. Thus, generating the electrochemical impedance spectra using a first-principle model is very advantageous.

5.4.2.2 Light Modulation Methods

Intensity modulated photocurrent spectroscopy (IMPS) measures the AC photocurrent resulting from the incident light modulation, whereas the intensity modulated photovoltage spectroscopy (IMVS) measures the AC-photovoltage[149]. In the IMVS technique, constant illumination of a DSSC at open circuit is used for generation of a photovoltage. The cell then is being perturbed by a small sinusoidal modulation of the illumination intensity superimposed on the steady-state level, and the response is being measured. To have the sample response in a linear regime the AC perturbation should be chosen in a way that the amplitude of the photo voltage does not deviate from its steady state more than 5-10 mV. The time constant that is extracted from the IMVS signal is attributed to the effective electron lifetime. In a similar fashion IMPS is the photocurrent response of the cell under light modulation[149]. Nevertheless the information that is being extracted from the data is quite different and is being used for determining the effective electron diffusion coefficient in the anode.

5.5 Conclusions

DSSC is a promising technology. It is estimated that its efficiency can reach values as high as 17%. To reach this goal, many parameters need to be optimized as the processes involved in the cell contain significant level of complexity. The energetic of the dye/semiconductor interface is an important parameter when new chromopohores as the light harvesting element in the cell is being considered. The semiconductor morphology, porosity and internal surface area are all among the parameters that determine the cell performance. The hole transport material in the cell which typically consists of a liquid electrolyte and the processes that govern the charge recombination and transfer at the interface of the electrolyte/semiconductor are among the major parameters for cell optimization. The most plausible scenarios to increase the cell efficiency are the increase in the light absorption in the cell and engineering the interface to reduce dye regeneration overpotential. A realistic model that accounts for the processes taking place in the cell can be helpful to a great extent when one considers fabricating a new cell and also investigates the reasons behind observed trend in the cell response. Fortunately with the wealth of experimental techniques, it is possible to calculate a large number of parameters that influence the cell behavior and used them as the input to the model to find the parameters that cannot be certainly measured using modeling approach. Besides, a true model based on the processes taking place in the system can significantly be useful in giving insight into design of the new system before doing any experiments.

6 Chapter 6: Macroscopic Modeling and Analysis of Dye Sensitized Solar Cells

6.1 Introduction

As stated in IEA report of 2011, solar power must see an annual average growth rate of 22% to meet the 2020 targets. Since 2005, a significant average growth rate of 50% in solar technologies has been observed. As it has been pointed out in this report, there remain challenges in maintaining this high growth for the longer term. As mentioned in the previous chapter, achieving this goal needs manufacturing cost reduction.

Many efforts should make to develop the lower cost solar cells to accomplish the cost reduction goal. With this respect, the manufacturing cost including processing as wells as raw materials, life time and stability of the cells, efficiency, scale-up and maintenance are the factors determining the success of the new developed solar cell technologies. Currently, the third generation photovoltaic cells based on hybrid junctions (nanocrystalline material and organic dye) and polymer-based materials are realized as the answer to producing low-cost devices [152]. DSSCs are the leading edge technology among the third generation photovoltaics[152]. The DSSC has the potential for a cost-effective photovoltaic technology because of the low cost of the raw materials and the capability of easy automated manufacturing[153-154]. Though having the advantage of low manufacturing cost, this technology suffers from some technological problems including leakage of solvents over the long term operation and corrosion of metal electrodes[152]. Thus, replacing the liquid electrolyte is critical for enhancing the operability and durability of the cell. Furthermore, despite the fact of inevitable losses in scaling up to module size, higher efficiencies compared to the highest reported conversion efficiency of 11% are still demanded, to ensure a long service life [153]. It is promising that the need to reach higher efficiencies will be resolved, since it appears that there is still room for improvement and optimization of the cell performance by adjusting the energetics inside the DSSC[153].

In the past few decades, extensive studies have been conducted in the utilization of solar energy as an alternative source of energy. As many efforts are currently toward the optimization of DSSCs and achievement of higher efficiency by tuning of the different cell components, mentioned in the previous chapter, mathematical models can expedite the route toward arriving to the optimal design and higher efficiency. Mathematical models can predict the performance of the cells, the IV curve and the cells efficiency, provide a better understanding of the physics behind the photo-conversion processes, and used in the design and optimal operation of the cells.

6.2 Literature Review on modeling of DSSCs

Generally, mathematical models can be developed on the basis of two different viewpoints, detailed level and system level. Hence, a photovoltaic system can be modeled to describe the cell characteristics, module characteristics, orientation and geometric characteristics, array-level characteristics, power conditioning unit level characteristics, plant-level characteristics, operations and maintenance characteristics and so [155].

Although modeling of the solid state solar cell has been extensively investigated and comprehensive models are available for this technology [155-157], the new generation of solar cell still needs to be studied as the physical phenomena occurring in the cell can be substantially different (e.g. dye sensitized and bulk heterojunction solar cells with inclusion of electrochemical processes and exciton-charge recombination respectively [158-159]). In summary, a solar cell system model can be developed by accounting for different phenomena including; photovoltaic, electro-thermal and direct heating and cooling processes [156]. Different approaches including equivalent circuit modeling and continuum modeling have been introduced as an effective way to predict the cell system behavior [160-163]. Because of the nonlinear dependence of the current-voltage characteristics of the cells on temperature and irradiance level, the cells are highly nonlinear[164].

For any type of solar cells, high efficiency is the key factor toward the large scale applications [165]. In this respect, optimization studies are very indispensible. Simulation studies should be performed to obtain the optimal design parameters at different irradiances. The decision variables are those characteristics of solar cell design which can be manipulated to achieve the optimization goal depending on the type of the solar cell [166]. As an example in the case of silicon solar cells, the major design parameters involve rear point contact area coverage, substrate doping concentration, and cell thickness [167]. Another important feature to consider in optimization studies is the sensitivity of efficiency to variations in the cell design parameters [166]. For DSSCs, almost all the components of the cell, including the semiconducting oxide substrate, the dyes, the electrolytes, the redox mediators and the counter electrode are tunable[149]. Here, we review some of the studies on modeling of DSSCs.

Södergren et al. [168] developed a simulation model accounting for electron diffusion in the TiO_2 layer. To simplify the model, the effect of electrolyte was not accounted in this model and analytical solution for the distribution of electron density was presented. Ferber et al. [162] developed a DSSC model as a pseudo-homogeneous effective medium, containing the nanoporous TiO_2 semiconductor, the dye and the redox electrolyte. The model was developed by applying continuity and transport equations for all the charge carriers, the electrons in the TiO_2 layer, the iodide, the triiodide and the cations of the electrolyte. They included the effect of electric field in their model attributed to the unbalanced charge-carrier distribution under illumination.

An extension to this model was presented by Oda et al. in which the bulk electrolyte layer was taken into account[169]. Topic et al. [170] developed a model by considering an optical model based on one-dimensional semi-coherent optical simulator SunShine, in which nanoporous active layer was modelled as effective medium layer with effective scattering of light at its front and back surface interface using effective roughness. The electrical model follows the work of Ferber et al.[162] with the exception that it does not account for the migration term. Generally in the charge transport both migration and diffusion can play a role within the semiconductor and electrolyte. In DSSCs, the electric field can be ignored because the electron charge is screened by the electrolyte, which eliminates the internal field[171].

It is noteworthy to mention that most of the studies on modeling of DSSCs are based on the Steady-state model and only few studies have been done under transient condition. Barnes et al. presented a model to study the steady state and transient behavior of the cell[172]. In this model, the electron density is distinguished to two terms of electron density in the trap states and conduction band. The time dependent simulations were compared with small and large transient photovoltage and photocurrent measurements. Andrade et al. presented a one-dimensional transient phenomenological model of a DSSC[173]. In this model, the recombination rate is based on a first order kinetic. They have also pointed to the advantages of a transient model for obtaining the relevant kinetic parameters with higher accuracy. Using parameter values by Wang et al., they showed that their simulation results agreed well with the EIS measurements. In this study, they showed that the EIS data can be found by applying the transient model[173], but detailed analysis of EIS was out of the scope of their study.

6.3 Model Development

Continuity and transport equations for all charged species in the cell, including the electrons in the TiO_2 semiconductor, and the redox species, have formed the backbone of the model. The model development has been along the work of Ferber et al.[162] but with the advantages of the model reduction and extending the model to transient conditions. The continuity equations for the four species in the cell including electrons (e^-), triiodide (I_3^-), iodide (I^-) and lithium ions (Li^+) are as follow:

$$\frac{\partial n_i}{\partial t} = G_i - R_i + \nabla \bullet J_i \tag{6.1}$$

Where i=e^- , I_3^- , I^- , and Li^+

G_i is the generation term and R_i is the loss rate which in the case of ionic species is the rate of their consumption and in the case of the electrons is called the electron recombination rate. Lastly, J_i is the flux of the species. In this section, the above terms for all the present species will be introduced and their corresponding equations will be defined.

6.3.1 **Electrons Recombination**

As explained in the previous chapter, not all the electrons created by the light absorption can be collected and transfer to the external circuit, because some of the charge carriers recombine before they transport through diffusion or drift to the external circuit[174]. Recombination can occur through two different pathways: a) regeneration of dye cation and b) reduction of the oxidized species in the electrolyte. It has been demonstrated that the first pathway is negligible in the presence of sufficient concentrations of iodide and sufficiently conductive electrolyte due to the rapid regeneration rate of the oxidized dye molecules by iodide[141].Therefore, the only recombination process considered in this study has been the electron transfer from the TiO_2 to the electrolyte. To calculate the recombination rate, the specific reaction scheme consisting of the intermediate steps should be taken into account[141]. The net reaction of iodide/triiodide (not an elementary step) is a two electron transfer process shown in the following equation:

$$3I^- \rightleftharpoons I_3^- + 2e^- \tag{6.2}$$

Three different reaction schemes have been suggested in the literature[137, 141, 175]. Schemes 1 and 2 propose that the back reaction is second order with respect to electron density. Schemes 1 and 2 are shown in the following consecutive reactions. The two elementary steps of 6.3 and 6.4 are the same in these two schemes. Scheme 1 takes the reaction 6.5 as the rate determining step, yet reaction 6.6 is the rate determining step in scheme 2 [141].

$$I_3^- \overset{K_1}{\rightleftharpoons} I_2 + I^- \tag{6.3}$$

$$I_2 + e^- \overset{K_2}{\rightleftharpoons} I_2^{-\bullet} \tag{6.4}$$

$$2I_2^{-\bullet} \xrightarrow{k_3} I_3^- + I^- \tag{6.5}$$

$$I_2^{-\bullet} + e^- \xrightarrow{k_4} 2I^- \tag{6.6}$$

The recombination rate based on the first and second schemes can be found by EQs. 6.7 and 6.8 respectively, where $\bar{n}_e$ is the dark equilibrium electron density.

$$R_e = K_1^2 K_2^2 k_3 \frac{n_{I_3^-}^{\ 2} (n_e - \bar{n}_e)^2}{n_{I^-}^{\ 2}} \tag{6.7}$$

$$R_e = K_1 K_2 k_4 \frac{n_{I_3^-} (n_e - \bar{n}_e)^2}{n_{I^-}} \tag{6.8}$$

The third scheme can be presented by[162]:

$$2I^- \underset{k_b}{\overset{k_f}{\rightleftharpoons}} 2I^\bullet + 2e^- \tag{6.9}$$

$$2I^\bullet \overset{K_5}{\rightleftharpoons} I_2 \tag{6.10}$$

$$I_2 + I^- \overset{K_6}{\rightleftharpoons} I_3^- \tag{6.11}$$

Reactions 6.10 and 6.11 are fast chemical reactions and they are assumed to be under equilibrium. Based on reaction 6.9, the net electron flow can be calculated by accounting the kinetics of forward (oxidation) and backward (reduction) reactions and is described by the following equation[162]:

$$R_e = k_b n_e n_{I^\bullet} - k_f n_{I^-} \tag{6.12}$$

At equilibrium, the rates of forward and backward reactions are equal and we have:

$$k_f \bar{n}_{I^-} = k_b \bar{n}_e \bar{n}_{I^\bullet} \qquad (6.13)$$

If we insert k_f from EQ. 6.13 and also find the concentration of $I^\bullet$ with respect the two fast reactions of 6.10 and 6.11 and plug into EQ.6.12, the rate of recombination can be described by[162]:

$$R_e = K_e \left\{ n_e \sqrt{\frac{n_{I_3^-}}{n_{I^-}}} - \bar{n}_e \sqrt{\frac{\bar{n}_{I_3^-}}{\bar{n}_{I^-}^3}} n_{I^-} \right\} \qquad (6.14)$$

$$\text{Where } K_e = \frac{k_b}{\sqrt{K_5 K_6}}$$

If we ignore the rate of forward reaction in the electron transfer reaction of 6.9 , the rate of recombination is given by [137]:

$$R_e = K_e (n_e - \bar{n}_e) \sqrt{\frac{n_{I_3^-}}{n_{I^-}}} \qquad (6.15)$$

Where K_e is the electron relaxation rate constant and $\bar{n}_e$, $\bar{n}_{I_3^-}$ and $\bar{n}_{I^-}$ are the dark equilibrium densities. Thus to evaluate the electron recombination rate, the equilibrium densities of electrons, iodide and triiodide should be found. The redox couples equilibrium densities can be considered as their initial concentration, since the initial iodide and triiodide concentrations are orders of magnitude higher than that of electrons[162]. The evaluation of electron density under dark equilibrium will be explained later in this section.

In the steady state model, four scenarios for recombination term have been considered based on calculation of recombination rate constants by EQs. 6.7, 6.8, 6.14 and 6.15. The EQ. 6.15 is based on the first order kinetic and it agrees with the approach presenting the recombination rate constant as the difference of the electron density with the dark equilibrium electron density divided by electron mean lifetime and calculated by[162]:

$$R_e = \frac{n_e - \overline{n}_e}{\tau_r} \tag{6.16}$$

By comparison of EQ. 6.15 by Eq. 6.16, we can find the definition of electron mean life time by:

$$\tau_r = \frac{1}{K_e}\sqrt{\frac{n_{I^-}}{n_{I_3^-}}} \tag{6.17}$$

6.3.2 **Electrons Generation**

Similar to Barnes et al.[172], the electron generation profile is approximated by using a single dye absorption coefficient which is equivalent to the supposition of monochromatic illumination. Thus the generation term can be explained by:

$$G_e = \alpha I_0 \exp(-\alpha x) \tag{6.18}$$

Where α is the absorption coefficient and I_0 is the incident photon flux.

6.3.3 **Ionic Species Generation and Consumption Rates**

Based on the net reaction of triiodide/iodide EQ. 6.2, the generation of two electrons relates to the production of one triiodide ion and the consumption of three iodide ions. Since cations are not involved in the electrochemical reaction, they are neither consumed nor generated. Thus, the rate of redox species generation and consumption are given by[162]:

$$\begin{aligned} G_{I_3^-} &= \frac{1}{2}G_e \\ R_{I_3^-} &= \frac{1}{2}R_e \\ G_{I^-} &= \frac{3}{2}R_e \\ R_{I^-} &= \frac{3}{2}G_e \\ G_{Li^+} &= R_{Li^+} = 0 \end{aligned} \tag{6.19}$$

6.3.4 Electrons and Ionic Species Transport

The driving force for the transport of species comes from the gradient of electrochemical potential. Using the Einstein relation to correlate mobility and diffusion ($\frac{u_i}{D_i} = \frac{q}{K_B T}$), the flux of species J_i is defined by:

$$J_i = -D_i \frac{\partial n_i}{\partial x} - z_i n_i u_i \frac{\partial \phi}{\partial x} \tag{6.20}$$

The first term is the Fick's law of diffusion and the second term is the migration or drift term[176].

6.3.5 Electrical Characteristics and the Energetics of the DSSC

The internal cell voltage relates to the difference between the Fermi level of the electron in the oxide layer and the redox potential of the electrolyte[147]. It should be noted that the internal cell voltage refers to the difference of potential between the boundaries of TCO and oxide layer and TCO and Pt layer. The internal cell voltage is defined by the following equation[162]:

$$U_{\text{int}} = \frac{1}{q}(E_F^n(0) - E_{\text{Re}dox}) \tag{6.21}$$

Where E_F^n is the electron quasi Fermi level and E_{redox} is the redox energy.

The density of electron in the conduction band determines the electron quasi Fermi level and the definition is as follow[149]:

$$n_e = N_{CB} \exp - \left(\frac{E_{CB} - E_F^n}{K_B T} \right) \tag{6.22}$$

Where E_{CB} is the energy of the conduction band edge and N_{CB} is the effective density of electron in the conduction band and is defined by the following equation:

$$N_{CB} = 2 \left(\frac{2\pi m_e^* K_B T}{h^2} \right)^{\frac{3}{2}} \tag{6.23}$$

m_e^* is the effective electron mass and h is the Planck's constant.

In the dark, electrons in the oxide layer are in equilibrium with the redox species and their equilibrium density can be given by:

$$\overline{n}_e = N_{CB} \exp - \left(\frac{E_{CB} - E_{F,redox}}{K_B T} \right) \tag{6.24}$$

To calculate the redox energy, the overvoltage at the Pt electrode (η_{Pt}) should be taken into account. The overvoltage is the difference of redox energy under open circuit condition and the redox energy at the working condition (j>0) and can be shown by the following equation:

$$\eta_{Pt} = \frac{E_{\mathrm{Re}dox}^{OC} - E_{\mathrm{Re}dox}}{q} \tag{6.25}$$

The redox energy under open circuit condition can be calculated using the Nernst equation as follow[162]:

$$E_{Redox}^{OC} = E_{\mathrm{Re}dox}^{0} - \frac{K_B T}{2} \ln \frac{n_{I_3^-}^{OC}(d) / n_{ref}}{\left(n_{I^-}^{OC}(d) / n_{ref} \right)^3} \tag{6.26}$$

Where $E^0_{\mathrm{Re}dox}$ is the standard redox potential and n$_{\mathrm{ref}}$ corresponds to the standard reference of 1 mol/L.

The internal cell current can be calculated from the rate of electron transfer at Pt electrode using the Butler-Volmer equation shown in the following equation:

$$j_e = j_0 \left\{ \sqrt{\frac{n_{I^{3-}}(d) n^{oc}_{I^-}(d)}{n^{oc}_{I^{3-}}(d) n_{I^-}(d)}} e^{(1-\beta)\frac{q}{K_B T}\eta_{pt}} - \frac{n_{I^-}(d)}{n^{oc}_{I^-}(d)} e^{-\beta\frac{q}{K_B T}\eta_{pt}} \right\} \tag{6.27}$$

Where j$_0$ is the exchange current density and β is the transfer coefficient.

If we insert EQ. 6.21 into EQ. 6.24, we can obtain the activation overpotential in the following form:

$$\eta_{Pt} = \frac{1}{q} E^n_F(0) - \frac{1}{q} E^{OC}_{redox} - U_{\mathrm{int}} \tag{6.28}$$

The external voltage is measured at the external contacts and is influenced by the series resistance in the TCO layers. The internal cell resistances arouse from charge transfer resistance, mass transfer resistance and so which are modeled with the set of governing differential equations[162]. Two other resistances including the TCO resistance and shunt resistance (R_p) , should be taken into account. Figure 6.1 shows the equivalent circuit of the cell; accounting for the series and shunt resistances[162].

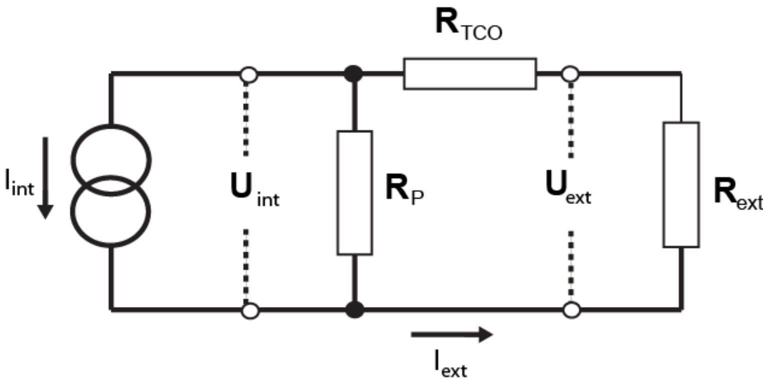

Figure 6.1. Equivalent circuit of the DSSC.[162]

By applying the Kirchhoff's law, the external current can be obtained by[162]:

$$I_{ext} = \left(\frac{R_P}{R_{ext} + R_{TCO} + R_P} \right) j_e A \tag{6.29}$$

From the equivalent circuit, it can be seen that the internal cell voltage is equal to the voltage drop across the external and TCO resistances and can be found by:

$$U_{\text{int}} = R_{TCO} I_{ext} + R_{ext} I_{ext} = \left(\frac{(R_{TCO} + R_{ext}) R_P}{R_{ext} + R_{TCO} + R_P} \right) j_e A \tag{6.30}$$

6.4 Steady State model

The schematic of the DSSC is shown in Figure 6.2. As can be seen, the cell is considered as a 1-D Pseudo-homogeneous medium of thickness L.

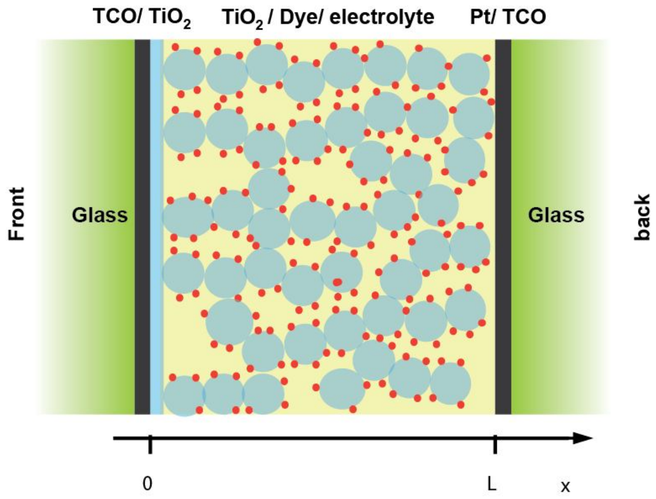

Figure 6.2. Schematic of a DSSC.

The continuity equation EQ. 6.1 for the different species in the cell under steady state condition can be formulated by the following set of equations:

$$\frac{dj_e}{dx} = R_e - G_e \tag{6.31}$$

$$\frac{dj_{I^-}}{dx} = -\frac{3}{2}\frac{dj_e}{dx} = \frac{3}{2}G_e - \frac{3}{2}R_e \tag{6.32}$$

$$\frac{dj_{I_3^-}}{dx} = \frac{1}{2}\frac{dj_e}{dx} = \frac{1}{2}R_e - \frac{1}{2}G_e \tag{6.33}$$

$$\frac{dj_c}{dx} = 0 \tag{6.34}$$

The mechanism of electron transport in the oxide phase leads to the development of two models. The first model is based on the assumption that both diffusion and migration should be considered in the charge transport and the second model ignores the effect of drift term. The drift term is due to electric field and can be characterized by the Poisson's equation[162].

$$\frac{dE}{dx} = \frac{q}{\varepsilon\varepsilon_0}(n_c - n_e - n_{I^-} - n_{I_3^-}) \tag{6.35}$$

Where ε_0 and ε are the permittivity of free space and the effective dielectric constant respectively.

To solve this set of equations, we nondimensionalize the system as follow:

$$D_e{}^* \frac{d^2 n_e^*}{dx^{*2}} + \psi e^{-\gamma x^*} - \varphi^2 \left\{ n_e^* \sqrt{\frac{n_{I_3^-}^*}{n_{I^-}^*}} - \overline{n}_e^* \sqrt{\frac{\overline{n}_{I_3^-}^*}{\overline{n}_{I^-}^{*\,3}} n_{I^-}^*} \right\} + \chi_1 \left(n_e{}^* \frac{dE^*}{dx^*} + E^* \frac{dn_e{}^*}{dx^*} \right) = 0 \tag{6.36}$$

$$D_{I_3^-}{}^* \frac{d^2 n_{I_3^-}^*}{dx^{*2}} + \frac{1}{2}\psi e^{-\gamma x^*} - \frac{1}{2}\varphi^2 \left\{ n_e^* \sqrt{\frac{n_{I_3^-}^*}{n_{I^-}^*}} - \overline{n}_e^* \sqrt{\frac{\overline{n}_{I_3^-}^*}{\overline{n}_{I^-}^{*\,3}} n_{I^-}^*} \right\} + \chi_2 \left(n_{I_3^-}^* \frac{dE^*}{dx^*} + E^* \frac{dn_{I_3^-}^*}{dx^*} \right) = 0 \tag{6.37}$$

$$D_{I^-}{}^* \frac{d^2 n_{I^-}^*}{dx^{*2}} - \frac{3}{2}\psi e^{-\gamma x^*} + \frac{3}{2}\varphi^2 \left\{ n_e^* \sqrt{\frac{n_{I_3^-}^*}{n_{I^-}^*}} - \overline{n}_e^* \sqrt{\frac{\overline{n}_{I_3^-}^*}{\overline{n}_{I^-}^{*\,3}} n_{I^-}^*} \right\} + \chi_3 \left(n_{I^-}^* \frac{dE^*}{dx^*} + E^* \frac{dn_{I^-}^*}{dx^*} \right) = 0 \tag{6.38}$$

$$D_{Li^+}{}^* \frac{d^2 n_{Li^+}^*}{dx^{*2}} - \chi_4 \left(n_{Li^+}^* \frac{dE^*}{dx^*} + E^* \frac{dn_{Li^+}^*}{dx^*} \right) = 0 \tag{6.39}$$

$$\frac{dE^*}{dx^*} = \frac{qLn_{ref}}{\varepsilon\varepsilon_0 E_{ref}}(n_{Li^+}^* - n_e^* - n_{I^-}^* - n_{I_3^-}^*) \tag{6.40}$$

Where $\varphi^2 = \frac{k_e L^2}{D_{ref}}$, $\psi = \frac{\eta_{inj}\alpha I_0 L^2}{n_{ref} D_{ref}}$, $\chi_1 = \frac{\mu_e E_{ref} L}{D_{ref}}$, $\chi_2 = \frac{\mu_{I_3^-} E_{ref} L}{D_{ref}}$, $\chi_3 = \frac{\mu_{I^-} E_{ref} L}{D_{ref}}$ and

$\chi_4 = \frac{\mu_{Li^+} E_{ref} L}{D_{ref}}$.

The above model is a system of nonlinear boundary value problems (BVPs). EQs. 6.36, 6.37, 6.38 and 6.39 are 2nd order ODEs and they can be converted to 1st order ODEs. After the conversion, we have a set of nine 1st order ODEs and the MATLAB routine *bvp5c* is used to solve this system of equations with the appropriate boundary conditions. We call this model, model I in the rest of this chapter. Model II ignores the drift term and assumes that there is no electric field in the media. Therefore, all the drift terms in the above system of equations disappear (the last term in the equations). Also, the continuity equation for cations is redundant in this case. Since there is no source or sink for cations, we have $j_{Li^+} = 0$ [162] which indicates constant density of cations in the absence of electric field. By this, model II reduces to a system of three 2nd order ODEs. Similar to model I, this model can be solved by converting the equations to six 1st order ODEs. This model can be implemented in MATLAB and integrated by BVP5c routine. In the following subsection, we introduce the boundary conditions of this problem.

6.4.1 **Boundary Conditions**

The boundary conditions are along with the work of Ferber et al.[162].For the electrons, at x=0 (the TCO and TiO_2 contact) the electron flux is correlated to the flow of electrons (cell current) from external circuit to the counter electrode (where the reduction occurs) which is calculated by using the Butler-Volmer equation, EQ. 6.27. The flux of electrons at x=d is zero because there is no contact between TiO_2 and platinized TCO[162]. The boundary conditions are given by:

$$x^* = 0 \quad \frac{n_{ref} D_{ref} q}{L}\left(D_e^* \left.\frac{dn_e^*}{dx^*}\right|_{x^*=0} \right) = j_0 \left\{ \sqrt{\frac{n_{I^{3-}}^*(d)\, n_{I^-}^{oc^*}(d)}{n_{I^{3-}}^{oc^*}(d)\, n_{I^-}^*(d)}}\, e^{(1-\beta)\frac{q}{K_B T}\eta_{pt}} - \frac{n_{I^-}^*(d)}{n_{I^-}^{oc*}(d)}\, e^{-\beta\frac{q}{K_B T}\eta_{pt}} \right\} \tag{6.41}$$

$$x^* = 1 \quad \frac{dn_e^*}{dx^*} = 0 \tag{6.42}$$

Based on the conservation of particles and the reaction scheme, three integral boundary conditions can be given by[162]:

$$\int_0^1 n^*_{Li^+}\,dx^* = \overline{n}^*_{Li^+} \tag{6.43}$$

$$\int_0^1 (n^*_{I_3^-} + \frac{1}{3} n^*_{I^-})\,dx^* = \overline{n}^*_{I_3^-} + \frac{1}{3}\overline{n}^*_{I^-} \tag{6.44}$$

$$\int_0^1 (\frac{1}{2} n^*_e + \frac{1}{3} n^*_{I^-})\,dx^* = \frac{1}{2}\overline{n}^*_e + \frac{1}{3}\overline{n}^*_{I^-} \tag{6.45}$$

The rest of the boundary conditions are given in the following equations:

$$j_{I^-}(0) = j_{I_3^-}(0) = j_{Li^+}(0) = 0 \tag{6.46}$$

$$E^*(0) = 0 \tag{6.47}$$

6.4.2 **IV Curve Generation**

Under steady state conditions, the IV curve of the cell can be constructed using the continuation method. A physical parameter of interest, external load resistance, is then varied from open circuit (Rext= ∞) to short circuit (Rext= 0) to have a sequence of problems with solutions close enough to secure convergence for the next value of the parameter on the way to reach the load resistance close to zero in which the short-circuit photocurrent is measured and the voltage is zero.

6.4.3 **Simulation Results: Model I and Model II**

The input parameters used in the simulation and comparison of model I and model II are identical to the ones presented by Ferber et al.[162] and are listed in Table 6.1.

Table 6-1. Input parameters of the model[162].

Description	Symbol	Value
Electron recombination rate constant	K_e	10^4 s^{-1}
Electron mobility	μ_e	0.3 cm^2/Vs
Iodide diffusion coefficient	D_{I^-}	8.5x10^{-6} cm^2/s
Triiodide diffusion coefficient	$D_{I_3^-}$	8.5x10^{-6} cm^2/s
Initial concentration of iodide	$c_{I^-}^0$	0.45 M
Initial concentration of triiodide	$c_{I_3^-}^0$	0.05 M
Effective mass of electron	m_e^*	5.6 m_e
Exchange current density at the Platinum electrode	j_0	0.1 A/cm^2
Symmetry parameter	β	0.78
Effective relative dielectric constant	ε	50
Difference of TiO_2 conduction band and standard redox energy	$E_{CB} - E_{\mathrm{Redox}}^0$	0.93 ev
TCO resistance	R_{TCO}	$6\,\Omega/\square$
Shunt resistance	R_P	10 $k\Omega$
Thickness of the cell	L	10 μm
Cell area	A	1 cm^2
Light intensity	I_0	$1*10^{17} cm^{-2}s^{-1}$
Light absorption coefficient	α	5000 cm^{-1}

The simulation results for model I are shown in figure 6.3. The plot shows the density of the different species in the cell, including the current density and the electric field. As can be seen, the electric field is not significant and in the case of open circuit condition is less compared to the short circuit because of the smoother profiles of the density of charged specie

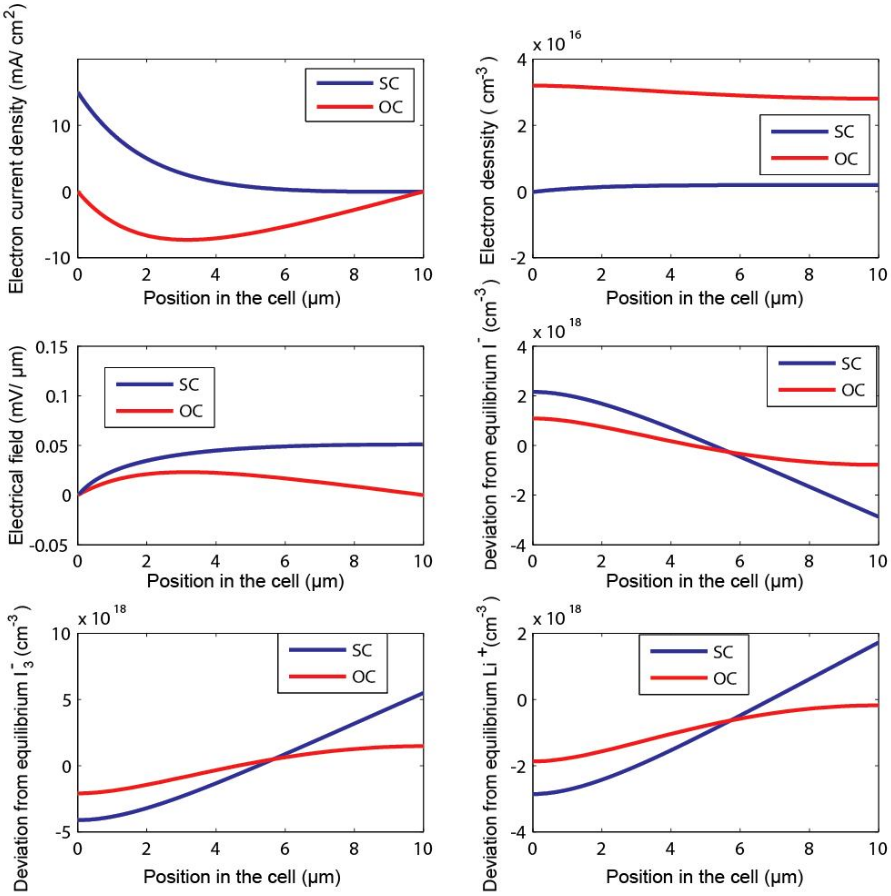

Figure 6.3. Model I simulation results: distribution of electron current density, electron density, electric field, deviation of iodide species from equilibrium, deviation of triiodide species from equilibrium, and deviation of lithium ions from equilibrium under short circuit (SC) and open circuit (OC) conditions.

The simulation results of model II are illustrated in figure 6.4. If we compare the profile of electron density, current density and difference of triiodide and iodide with the equilibrium values under the two limiting conditions of short circuit and open circuit, we can observe that they are similar. This theoretical simulation proves that the effect of electric field is negligible and diffusion term mostly contributes in the electron and charged species transport.

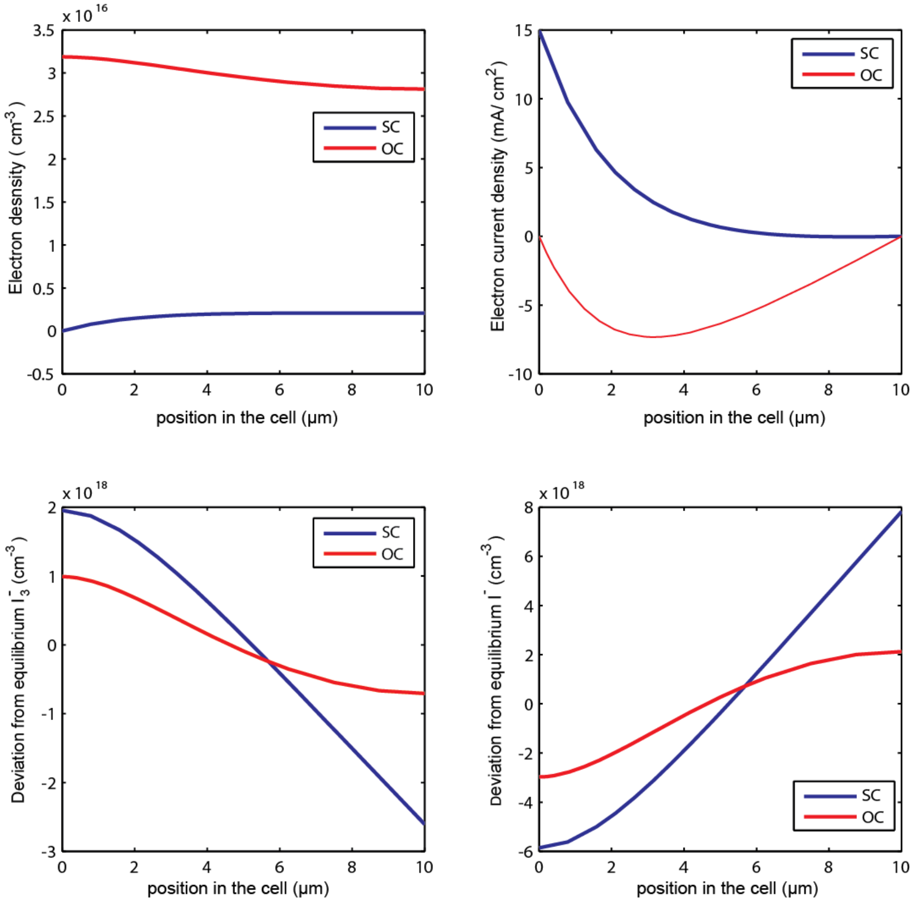

Figure 6.4. Model II simulation results: distribution of electron density, electron current density, triiodide and iodide deviations from equilibrium.

6.4.4 Champion DSSC: 11.1 % Conversion

So far, 11.1 % efficiency is one of the highest achieved efficiencies for DSSCs[177]. The photoanode of this cell is composed of a 12 micron mesoporous titanium dioxide electrode fabricated through sol-gel process using nanoparticles of 20 nm with 4 µm scattering layer which consists of 400 nm particles. The effect of scattering layer is mostly in the red region. The photoanode was sensitized by soaking them in $5x10^{-4}$ M N719 dye in 50/50 volume % solution of acetonitrile in tert-butanol. Finally a sandwich cell was prepared by using the dye sensitized electrode as the working electrode and conducting glass coated with chemically deposited platinum from 0.05M-hexachloroplatinic acid as a counter electrode. The two electrodes were superimposed and separated with a thin transparent film of Surlyn polymer gasket. The electrolyte solution; which was employed, contained 0.60 M butylmethylimidazolium iodide (BMII), 0.03 M I2, 0.10 M guanidinium thiocyanate and 0.50 M tertbuthylpyridine in a mixture of acetonitrile and valeronitrile volume ratio: 85:15, was introduced into inter electrode space from the counter electrode side through a pre-drilled hole. This cell was masked with a black plastic with a hole (0.158 cm^2) and tested under 1 Sun (1.5 AM) condition. Here in the modeling of the above cell, we considered four different scenarios based on the different mechanisms for the recombination kinetic (EQs. 6.7, 6.8, 6.14 and 6.15) to estimate the cell parameters by optimization method. The estimated parameters are the critical parameters in the performance of the cell and it is of importance to investigate the effect of these parameters.

6.4.4.1 Parameter Estimation

To estimate the parameters, the MATLAB routine `fminsearch,` which is based on the Nelder-Mead simplex algorithm, is used to locate the parameter values that minimize the following objective function:

$$J\left(\vec{\Delta}\right)=\sum_{i=1}^{i=n}(I_{mod,i}(\vec{\Delta})-I_{mea,i})^2+(V_{mod,i}(\vec{\Delta})-V_{mea,i})^2 \tag{6.48}$$

Where $\vec{\Delta}=(K_e, D_e, j_0, E_{CB}-E^0_{\mathrm{Re}dox}, R_P, \alpha, I_0)$

Where K_e is the recombination rate constant, D_e is the effective electron diffusion coefficient, j_0 is the exchange current density, $E_{CB}-E^0_{\mathrm{Re}dox}$ is the difference of the conduction band energy and the standard redox potential, R_P is the shunt resistance, α is the absorption coefficient and I_0 is the light intensity.

6.4.4.2 Scenario I

In this case, the recombination rate follows EQ. 6.7 and the recombination rate is 2nd order with respect to electron density and triiodide density.

Table 6-2. Estimated parameters employing a second order electron recombination kinetic EQ. 6.7.

K_e (recombination rate constant) ($1/m^3s$)	1.7e-19
D_e (electron diffusion coefficient) (m^2/s)	9.8e-07
j_0 (exchange current density) (A/m^2)	2506.1
R_P (shunt resistance) (*ohm*)	413.5
E_{CB}-E^0_{redox} (difference of conduction band and formal redox potential) (*eV*)	1.03
α (absorption coefficient) (*1/m*)	8.5e+5

I_0(spectral incident photon flux density)($m^{-2}s^{-1}$)	1.17e+21

6.4.4.3 Scenario II

In this case, the recombination rate follows EQ. 6.14 and the recombination rate is 1st order with respect to electron density.

Table 6-3. Estimated parameters employing a second order electron recombination kinetic EQ. 6.14.

K_e (recombination rate constant)($1/m^3s$)	2.9e-20
D_e (electron diffusion coefficient) (m^2/s)	9.9e-07
j_0 (exchange current density) (A/m^2)	1278.7
R_P (shunt resistance) (*ohm*)	409.7
E_{CB}-E^0_{redox} (difference of conduction band and formal redox potential) (*eV*)	1.04
α(absorption coefficient) (*1/m*)	9.5e+5
I_0(incident photon flux) ($m^{-2}s^{-1}$)	1.17e+21

6.4.4.4 Scenario III

In this case, the recombination rate follows EQ. 6.14 and the recombination rate is 1st order with respect to electron density.

Table 6-4. Estimated parameters employing a first order electron recombination kinetic EQ. 6.14.

K_e (recombination rate constant) (*1/s)*	1342.5
D_e (electron diffusion coefficient) (m^2/s)	9.79e-07
j_0 (exchange current density) (A/m^2)	1053.3
R_P (shunt resistance) (*ohm*)	4370.4
E_{CB}-E^0_{redox} (difference of conduction band and formal redox potential) (*eV*)	1.05
α(absorption coefficient) (*1/m*)	7.2e+05
I_0(incident photon flux)($m^{-2}s^{-1}$)	1.11e+21

6.4.4.5 Scenario IV

In this case, the recombination rate follows EQ. 6.15 and the recombination rate is 1st order with respect to electron density.

Table 6-5. Estimated parameters employing a first order electron recombination kinetic EQ. 6.15.

K_e (recombination rate constant)(*1/s*)	1022.2
D_e (electron diffusion coefficient) (m^2/s)	9.2e-07
j_0 (exchange current density) (A/m^2)	3017.9
R_P (shunt resistance) (*ohm*)	471.99
E_{CB}-E^0_{redox} (difference of conduction band and formal redox potential) (*eV*)	1.05
α (absorption coefficient) (*1/m*)	7.05e+05
I_0(incident photon flux)($m^{-2}s^{-1}$)	1.17e+21

6.5 Sensitivity Analysis

Not all the parameters introduced in the previous section have similar influence on the system behavior. In this section, the sensitivity of different parameters on the system behavior; when the recombination rate follows scenario III, is determined. The sensitivity of the parameters is obtained by applying a small change ±5-10% in the parameter and determining the corresponding change in the objective function relative to the optimal objective function value. Table 6-6 shows the sensitivity analysis of the seven parameters. It can be seen that the most sensitive parameters are the light intensity and the difference of conduction band with standard redox electrolyte.

Table 6-6. Model parameters sensitivity analysis.

Parameter	% change in the parameter with respect to the optimal value	% change in the objective function with respect to the optimal value
K_e	-10,-5, 5, 10	3.83, 3.87, 5.44, 5.48
D_e	-10, -5, 5,10	3.91, 3.92, 5.40, 5.41
J_0	-10, -5, 5,10	-0.03, -0.02, 0, 3.92
R_P	-10, -5, 5,10	2.23, 3.12, 6.12, 6.79
$E_{CB}-E^0_{redox}$	-10, -5, 5,10	31.71, 11.32, 8.71, 16.72
α	-10, -5, 5,10	3.93, -4.68, 3.93,3.94
I_0	-10, -5, 5,10	105.02, 35.77, 35.18, 99.83

6.6 Effect of Recombination Rate Constant and Conduction Band Movement

To study the effect of recombination rate constant and conduction band movement, we consider scenario III as the base and postulate the 1st order recombination rate with respect to electron density. Figure 6.5 illustrates the effect of changes in the recombination rate constant. It can be seen that recombination affects both open circuit voltage and short circuit current.

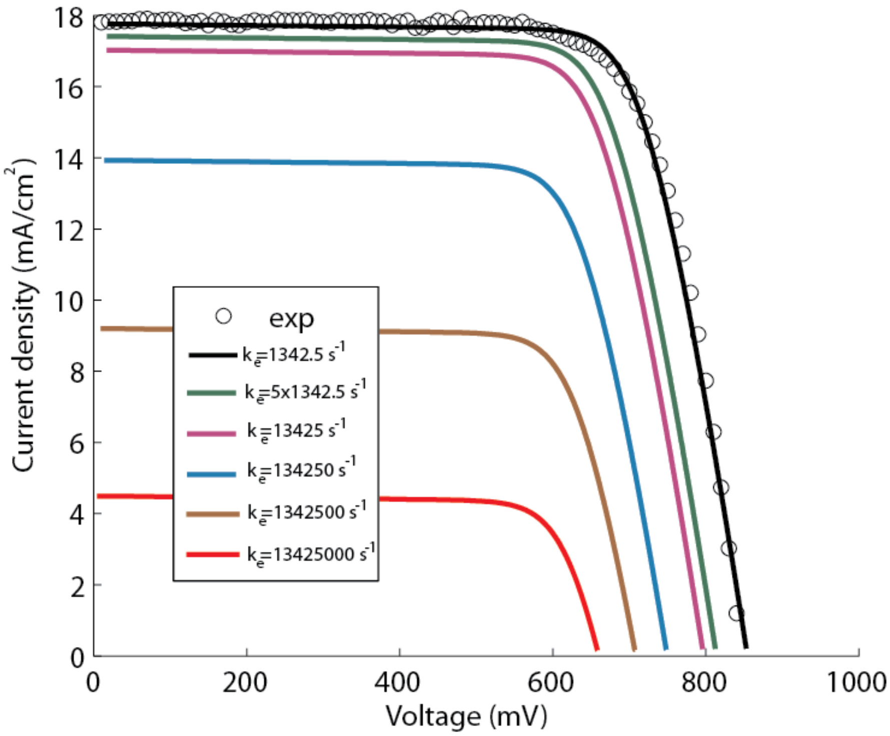

Figure 6.5. Effect of changes in recombination rate constant on the cell IV curve. The black curve shows the IV curve found by parameter estimation (basis). The colored curves show the IV curve while the recombination rate constants increase compared to the basis.

Figure 6.6 illustrates the effect of changes in the conduction band edge position. These results are similar to the experimental observations of surface treatment of the cell by 4-tert-butylpyridine (TBP)[177-178]. The addition of TBP shifts the electronic states of TiO_2 toward higher energies. This can be attributed to the fact that TBP is a weak base which renders the surface charge more negative when adsorbed on TiO_2[162].

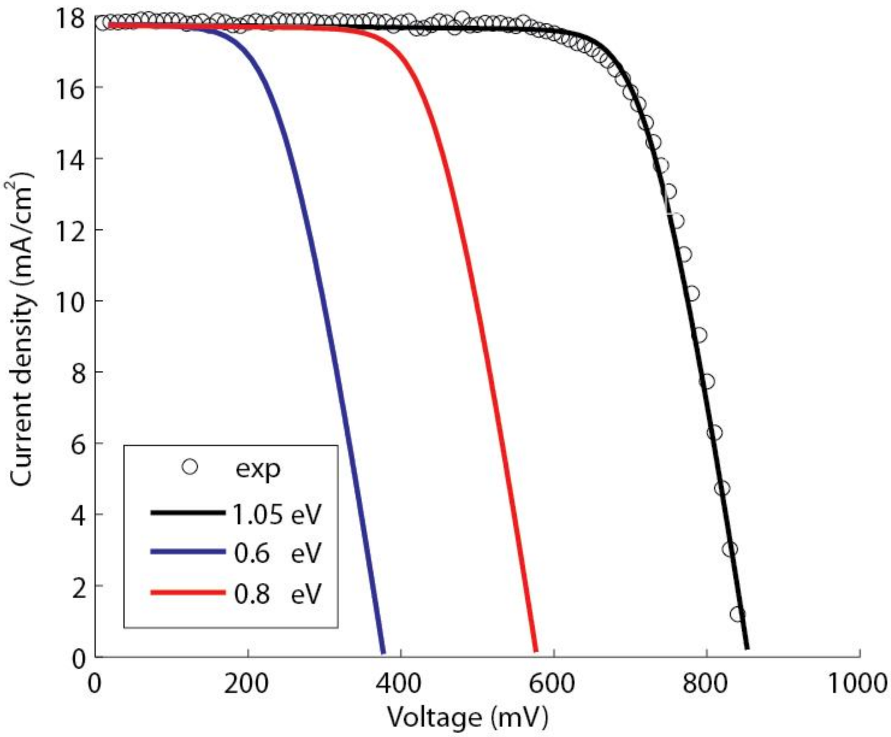

Figure 6.6. Effect of changes in the conduction band position on the cell IV curve. The black curve shows the IV curve found by parameter estimation (basis). The colored curves show the IV curve while the conduction band shifts to lower values of negative potential.

6.7 Quasi-solid State Electrolyte DSSC

The liquid electrolyte DSSC suffers from problems such as leakage of solvents in long-term operations and corrosion of metal electrodes. Thus, replacing the liquid electrolyte is critical for enhancing the operability and durability of the cells. In a recent work by Nejati and Lau[179] , the possibility of polymer integration within the mesoporous electrode is demonstrated. They used ethanolic solution of the N719 for sensitization of mesoporous electrodes spun coated on the conductive glass substrate from an aqueous paste of titanium dioxide nanoparticles with nominal particle size of 25 nm. In their work, the sample porosity was estimated to be around 50%. Followed by electrode fabrication, they integrated poly(2-hydroxylethyl methacrylate) with average MW of ~ 2400 g/mol within the mesoporous network of sensitized electrode. Further a 0.05M iodine and 0.5 M Lithium iodide in a mixture propylene carbonate and *gamma* butryrolactone with 50:50 volume ratios were introduced into their polymer/electrode assembly. They also used chemically deposited platinum from 0.05M-hexachloroplatinic acid as their counter electrode. Their fabricated cell were compared with the liquid equivalent where they had no polymer within the network and used a 25 μm Surlyn polymer gasket to separate the two electrodes . Similar to the Champion DSSC, we did the parameter estimation and the estimated parameters are listed in Table 6-7.

Table 6-7. Estimated parameters of polymer incorporated DSSC based on a first order electron recombination kinetic EQ. 6.15.

K_e (recombination rate constant)(*1/s*)	1.3e+4
D_e (electron diffusion coefficient) (m^2/s)	1.4e-08
j_0 (exchange current density) (A/m^2)	3293.6
R_P (shunt resistance) (*ohm*)	1543.09
E_{CB}-E_0 (difference of conduction band and formal redox potential) (*eV*)	0.9
α (absorption coefficient) (*1/m*)	3.9e+05
I_0(incident photon flux) ($m^{-2}s^{-1}$)	1.1e+21

Figure 6.7 shows the experimental results and theoretical predictions of the quasi solid state and liquid electrolyte DSSC. The estimation of the cell key parameters indicated that in the case of liquid electrolyte DSSC the difference of

conduction band and redox potential is about 0.66 eV. Also, it was found that the recombination rate constant increases very slightly compared to the solid state electrolyte DSSC. The obtained value was 1.6e4 (1/s). The next section explains the possible underlying reason of band edge movement.

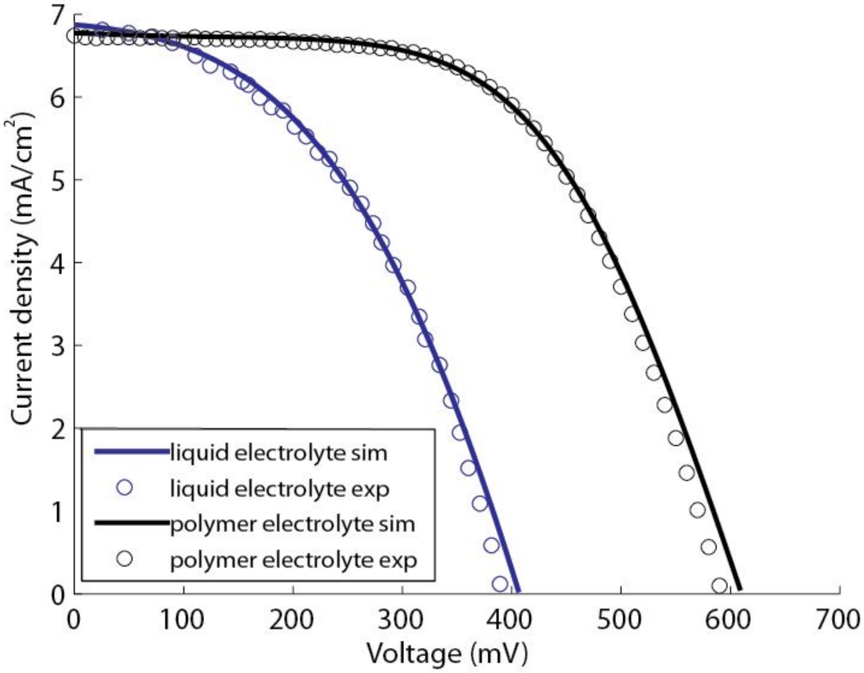

Figure 6.7. IV curve of the cell a) in the case of using liquid electrolyte (blue) b) in the case of the cell fabricated with polymer electrolyte (black).

6.7.1 **Surface Modification and Band Edge Movement**

The effect of surface treatment has been previously investigated in DSSC treated with vinylpyridine, tert-butyl pyridine and poly (vinyl pyridine). Interestingly the previous results show that the open circuit cell voltage increases while short circuit current density changes very little [163, 180-181]. This has been attributed to both the reduction of the recombination rate and band edge movement. The band edge movement justification is in line with the deporotonation of the Ti-OH species that has been previously observed with pH variation of medium for TiO_2 electrode[182]. The simulation results here suggest that reduction in recombination rate constant cannot solely be the reason for such an increase in open circuit voltage both in the case of TBP treatment and in polymer electrolyte system, and to capture the behavior of the cell, the band edge movement seems to be a more critical parameter. In case of the polymer integrated DSSC, the interaction of oxygen group on the polymer backbone with the OH group on the surface may induce the band edge movement towards a more negative value (vs. NHE).

6.8 Transient Model

Unlike Andrade et al.[173], the recombination term is not simplified to first order recombination with constant electron life time and detailed kinetic approach of Ferber et al. with the assumption of charge transfer as the rate determining step is included in the model. Under transient conditions, the governing equations are a set of partial differential equations (PDEs) with corresponding boundary and initial conditions. The PDEs are discretized spatially and then the resulting ODEs are integrated with respect to time using an ODE solver. The model is given by following equations:

$$D_e^{\,*}\frac{\partial^2 n_e^*}{\partial x^{*2}}+\psi e^{-\gamma x^*}-\varphi^2\left\{n_e^*\sqrt{\frac{n_{I_3^-}^*}{n_{I^-}^*}}-\overline{n}_e^*\sqrt{\frac{\overline{n}_{I_3^-}^*}{\overline{n}_{I^-}^{*\,3}}}n_{I^-}^*\right\}=\frac{\partial n_e^*}{\partial\theta} \tag{6.49}$$

$$D_{I_3^-}^{\,*}\frac{\partial^2 n_{I_{3^-}}^*}{\partial x^{*2}}+\frac{1}{2}\left[\psi e^{-\gamma x^*}-\varphi^2\left\{n_e^*\sqrt{\frac{n_{I_3^-}^*}{n_{I^-}^*}}-\overline{n}_e^*\sqrt{\frac{\overline{n}_{I_3^-}^*}{\overline{n}_{I^-}^{*\,3}}}n_{I^-}^*\right\}-\frac{\partial n_e^*}{\partial\theta}\right]=\frac{\partial n_{I_3^-}^*}{\partial\theta} \tag{6.50}$$

$$D_{I^-}^{*}\frac{\partial^2 n_{I^-}^{*}}{\partial x^{*2}}-\frac{3}{2}\left[\psi e^{-\gamma x^{*}}-\varphi^2\left\{n_e^{*}\sqrt{\frac{n_{I_3^-}^{*}}{n_{I^-}^{*}}}-\bar{n}_e^{*}\sqrt{\frac{\bar{n}_{I_3^-}^{*}}{\bar{n}_{I^-}^{*\,3}}}\,n_{I^-}^{*}\right\}-\frac{\partial n_e^{*}}{\partial\theta}\right]=\frac{\partial n_{I^-}^{*}}{\partial\theta} \tag{6.51}$$

The transient model has the potential to be used for EIS simulation. We have studied the transient behavior of the system from dark equilibrium to open circuit and short circuit conditions. Figure 6.8 and 6.9 show that the response of the electron transfer is faster than those of the redox species. The IV curve of the cell can be generated after the solution reached the Steady state. The IV curve generated using the transient model was identical to the one simulated by solving the BVPs.

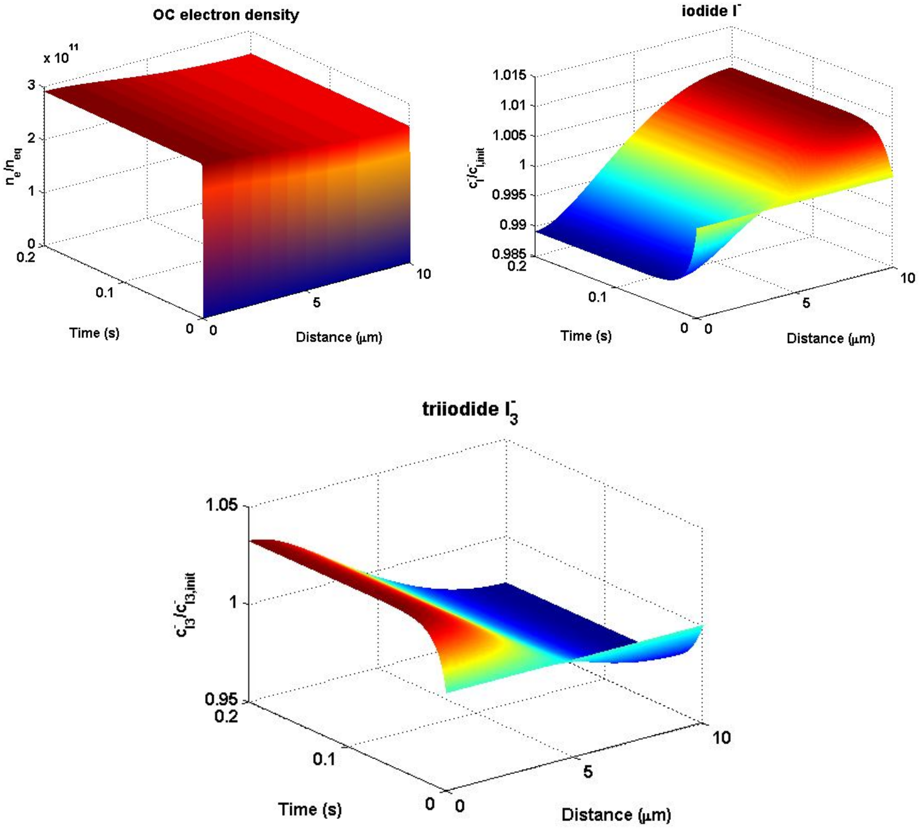

Figure 6.8. Distribution of electron density, iodide and triiodide species from dark equilibrium to open circuit condition.

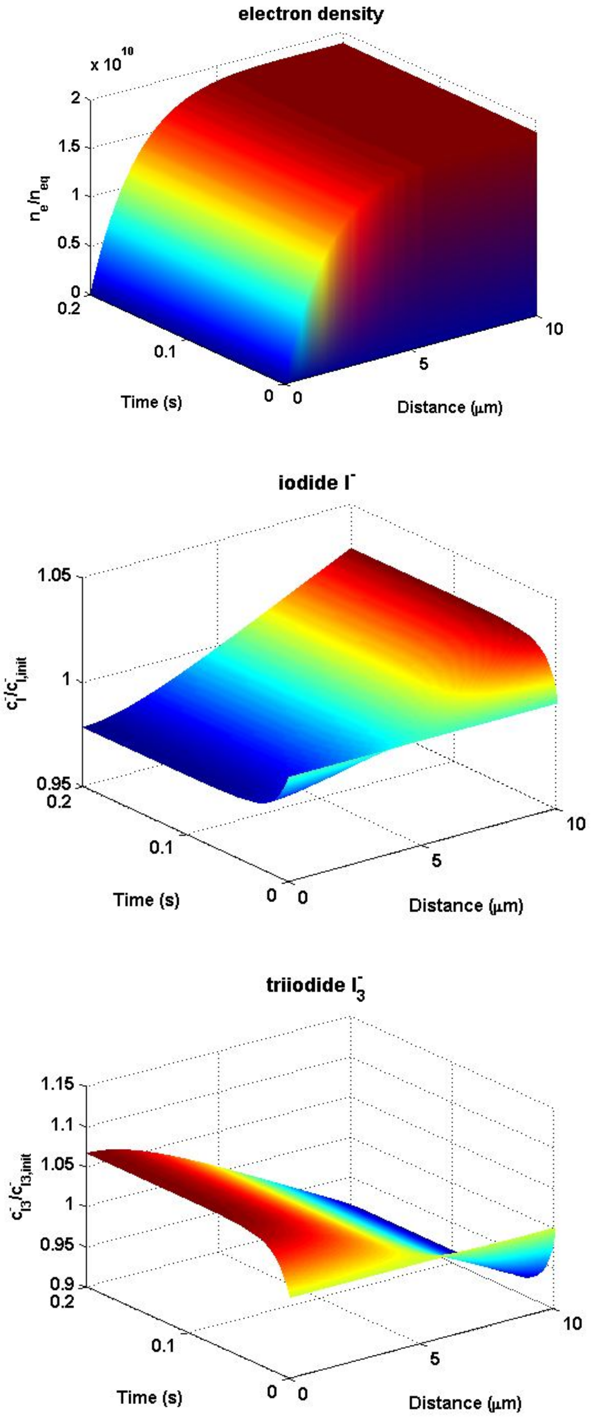

Figure 6.9. Distribution of electron density, iodide and triiodide species from dark equilibrium to short circuit condition.

6.9 Concluding Remarks

The model accounting for continuity and transport of electrons and redox species can predict the experimental results. Depending on the postulation of recombination kinetic, the estimated key parameters of the cell including effective electron diffusion coefficient, recombination rate constant, the position of conduction band, and exchange current density are different. Thus, there is a need for further experiments in conjunction with theoretical studies to identify the true mechanism. It was shown that the effect of electric field is negligible and the transport is mainly by diffusion rather than drift. The results of the simulation here suggest that the decrease in the recombination rate constant cannot solely be the reason for such an increase in open circuit voltage both in the case of TBP treatment and in polymer electrolyte system and to capture the behavior of the cell the band edge movement effect seems to be a critical parameter.

7 Chapter 7: Conclusions and Recommended Future Work

7.1 Summary and Conclusions

The presence of multiple steady states for three different types of SOFCs including oxygen-ion conducting, proton conducting and co-ionic conducting SOFCs was shown theoretically. Prior to this work, there was no study in the literature on the presence of multiple steady states in proton conducting and co ionic conducting SOFCs. It was found that the cell can have up to three steady states under potentiostatic and constant ohmic load modes of operation. Under galvanostatic mode of operation, presence of a unique steady state was identified. It was found that the inlet gas temperatures, heat convection coefficient and inlet flow rates affect the existence of multiple steady states. Also, the design of the cell, anode supported, cathode supported or electrolyte supported is another factor that affects the multiple steady state region.

Further, the ignition and extinction phenomena in the solid temperature and outlet gas concentrations were observed to coexist. Ignition and extinction behavior in the cell temperature is opposite to that of the reactant concentrations. While the concentrations of reactants and water product at the cathode side (in the case of co-ionic conducting SOFC) are under ignition, the cell temperature and the water concentration at the anode side are in the extinction branch and vice versa.

The dynamic behavior of the cell in the multiple steady state region is opposite to the typical cell behavior in which the cell voltage and current response are in the opposite direction when a step change is applied to the load resistance. This behavior can be explained as follows. When the ignition occurs, the cell current and temperature increase. As the temperature increases, the electrolyte ohmic resistance and the ohmic overpotential decrease. It should be noted when the ignition occurs, the ohmic resistance has a dominating effect, leading to a decrease in the ohmic overpotential, while when the ignition or extinction does not occur the cell current is more dominant, resulting in an increase in the ohmic overpotential.

The models of the proton conducting and co-ionic conducting SOFCs were validated under isothermal condition. They can predict the polarization curve accurately.

For DSSCs, the continuity and transport equations are the backbone of the mathematical model. Based on the reaction mechanism, the recombination rate can be first or second order with respect to electron density. Accounting for two different models a) transport by diffusion and migration b) transport by diffusion, it was found that the effect of electric field is negligible and diffusion mainly contributes to the electron and charged species transport. Parameter estimation for the key parameters of the cell including effective electron diffusion coefficient, TiO_2 conduction band energy, recombination rate constant and so was conducted. The parameters were feasible based on the reported values in the literature.

The effect of additives such as TBP was investigated using the model. It was found that both recombination rate constant and conduction band energy level are playing a role in the change of the photovoltage of the cell. The model simulations showed that reduction in recombination rate constant cannot solely be the reason for the observed increase in open circuit voltage of the polymer integrated DSSC. It can be hypothesized that the band edge movement is another factor responsible for the observed phenomena.

7.2 Recommended Future Work

The studies on SOFCs were carried out on STR fuel cells; thus new experimental and theoretical studies should focus on the effect of steady-state multiplicity in integral fuel cell systems. Also, the effect of balance of plat components such as heat exchangers in conjunction with the fuel cell model is important in analysis of the effect of nonlinear phenomena. In this dissertation, all the studies were based on considering hydrogen as a fuel. There is a need for further studies in the case of using other types of fuels such as methane in which the reforming and shift reactions should be accounted in the model when internal reforming occurs or accounting for the reformer in the case of external reforming. It is also of interest to study the presence of multiple steady states for tubular SOFCs. In the case of tubular SOFCs, the radiation heat transfer cannot be neglected and this influences the heat removal.

Further, the dynamic experimental studies are very limited in the literature and there is a need for more experimental design to capture the dynamic behavior of the cell and validate the dynamic models.

In the area of DSSCs, there is a need to reliably estimate the cell parameters. Combination of steady state and transient characterization techniques and simulation studies can be very beneficial. Most of the models for simulation of EIS and IMVS are very simple and in the case of EIS, they are mostly based on the equivalent circuit of the cell. Using transient model for simulation of EIS in combination with steady state models for simulating the IV curve of the cell is very helpful in reliable estimation of the cell key parameters. More experimental studies should be conducted to study the effect of additives such as TBP and Li^+ on the cell performance. There is a need to systematically account for these kinds of interfacial effects in the theoretical models as the junction energetic is sensitive to surface treatment. In the case of quasi solid state DSSC incorporating polymer electrolytes, it is very advantageous to study the effect of different polymer and the potential change in the TiO_2 energetics.

In most of the modeling studies accounting for the redox species continuity, the electron diffusion coefficient is considered constant and the effect of temperature and electron density has not been accounted in the model while it has been shown that diffusion coefficient can changes two orders of magnitude depending on the cell condition.

Many of studies in the area of modeling DSSCs accounted for the first order recombination and considered the mean electron life time as a constant parameter, while this changes at different working conditions. Thus, considering electron life time as a constant value is not a good approximation and it is necessary to account for the reaction mechanism which depends on the redox species in the electrolyte.

LIST OF REFERENCES

1. Yamamoto, O., Solid oxide fuel cells: fundamental aspects and prospects. *Electrochimica Acta* **2000,** 45, (15-16), 2423-2435.

2. Cheddie, D.; Munroe, N., Review and comparison of approaches to proton exchange membrane fuel cell modeling. *Journal of Power Sources* **2005,** 147, (1-2), 72-84.

3. Xue, X.; Tang, J.; Sammes, N.; Du, Y., Dynamic modeling of single tubular SOFC combining heat/mass transfer and electrochemical reaction effects. *Journal of Power Sources* **2005,** 142, (1-2), 211-222.

4. Singhal, S.; Kendall, K., *High temperature solid oxide fuel cells: fundamentals, design, and applications*. Elsevier Science Ltd: 2003.

5. Padulles, J.; Ault, G.; McDonald, J., An integrated SOFC plant dynamic model for power systems simulation. *Journal of Power Sources* **2000,** 86, (1), 495-500.

6. Hall, D. J.; Colclaser, R. G., Transient modeling and simulation of a tubular solid oxide fuel cell. *IEEE Trans. Energy Convers.* **1999,** 14, (3), 749-753.

7. Sedghisigarchi, K.; Feliachi, A., Dynamic and transient analysis of power distribution systems with fuel cells - Part I: Fuel-cell dynamic model. *IEEE Trans. Energy Convers.* **2004,** 19, (2), 423-428.

8. Lu, N.; Li, Q.; Sun, X.; Khaleel, M., The modeling of a standalone solid-oxide fuel cell auxiliary power unit. *Journal of Power Sources* **2006,** 161, (2), 938-948.

9. Gebregergis, A.; Pillay, P.; Bhattacharyya, D.; Rengaswemy, R., Solid oxide fuel cell modeling. *Industrial Electronics, IEEE Transactions on* **2009,** 56, (1), 139-148.

10. Hajimolana, S. A.; Soroush, M., Dynamics and Control of a Tubular Solid-Oxide Fuel Cell. *Ind. Eng. Chem. Res.* **2009,** 48, (13), 7.

11. Vayenas, C. G.; Debenedetti, P. G.; Yentekakis, I.; Hegedus, L. L., Cross-Flow, Solid-State Electrochemical Reactors - A Steady-State Analysis. *Industrial & Engineering Chemistry Fundamentals* **1985,** 24, (3), 316-324.

12. Ahmed, S.; McPheeters, C.; Kumar, R., Thermal-Hydraulic Model of a Monolithic Solid Oxide Fuel-Cell. *Journal of the Electrochemical Society* **1991,** 138, (9), 2712-2718.

13. Hirano, A.; Suzuki, M.; Ippommatsu, M., Evaluation of a New Solid Oxide Fuel Cell System by Non-isothermal Modeling. *Journal of the Electrochemical Society* **1992,** 139, 2744.

14. Achenbach, E. In 3-Dimensional and Time-Dependent Simulation of a Planar Solid Oxide Fuel-Cell Stack, 1994; Elsevier Science Sa Lausanne: 1994; pp 333-348.

15. Costamagna, P.; Arato, E.; Achenbach, E.; Reus, U., Fluid Dynamic Study of Fuel-Cell Devices - Simulation and Experimental Validation. *Journal of Power Sources* **1994,** 52, (2), 243-249.

16. Bessette II, N. F.; Wepfer, W. J.; Winnick, J., A mathematical model of a solid oxide fuel cell. *Journal of the Electrochemical Society* **1995,** 142, 3792.

17. Ferguson, J.; Fiard, J.; Herbin, R., Three-dimensional numerical simulation for various geometries of solid oxide fuel cells. *Journal of Power Sources* **1996,** 58, (2), 109-122.

18. Costamagna, P., The benefit of solid oxide fuel cells with integrated air pre-heater. *Journal of Power Sources* **1997,** 69, (1-2), 1-9.

19. Boersma, R. J.; Sammes, N. M., Computational analysis of the gas-flow distribution in solid oxide fuel cell stacks. *Journal of Power Sources* **1996,** 63, (2), 215-219.

20. Yakabe, H.; Hishinuma, M.; Uratani, M.; Matsuzaki, Y.; Yasuda, I., Evaluation and modeling of performance of anode-supported solid oxide fuel cell. *Journal of Power Sources* **2000,** 86, (1-2), 423-431.

21. Lehnert, W.; Meusinger, J.; Thom, F., Modelling of gas transport phenomena in SOFC anodes. *Journal of Power Sources* **2000,** 87, (1), 57-63.

22. Iwata, M.; Hikosaka, T.; Morita, M.; Iwanari, T.; Ito, K.; Onda, K.; Esaki, Y.; Sakaki, Y.; Nagata, S., Performance analysis of planar-type unit SOFC considering current and temperature distributions. *Solid State Ion.* **2000,** 132, (3-4), 297-308.

23. Yakabe, H.; Ogiwara, T.; Hishinuma, M.; Yasuda, I., 3-D model calculation for planar SOFC. *Journal of Power Sources* **2001,** 102, (1-2), 144-154.

24. Aguiar, P.; Chadwick, D.; Kershenbaum, L., Modelling of an indirect internal reforming solid oxide fuel cell. *Chemical Engineering Science* **2002,** 57, (10), 1665-1677.

25. Recknagle, K. P.; Williford, R. E.; Chick, L. A.; Rector, D. R.; Khaleel, M. A., Three-dimensional thermo-fluid electrochemical modeling of planar SOFC stacks. *Journal of Power Sources* **2003,** 113, (1), 109-114.

26. Haynes, C., Simulating process settings for unslaved SOFC response to increases in load demand. *Journal of Power Sources* **2002,** 109, (2), 365-376.

27. Beale, S. B.; Lin, Y.; Zhubrin, S. V.; Dong, W., Computer methods for performance prediction in fuel cells. *Journal of Power Sources* **2003,** 118, (1-2), 79-85.

28. Ota, T.; Koyama, M.; Wen, C. J.; Yamada, Y.; Takahashi, H. In *Object-based modeling of SOFC system: dynamic behavior of micro-tube SOFC*, 2003; Elsevier Science Bv: 2003; pp 430-439.

29. Petruzzi, L.; Cocchi, S.; Fineschi, F., A global thermo-electrochemical model for SOFC systems design and engineering. *Journal of Power Sources* **2003,** 118, (1-2), 96-107.

30. Li, P. W.; Chyu, M. K., Simulation of the chemical/electrochemical reactions and heat/mass transfer for a tubular SOFC in a stack. *Journal of Power Sources* **2003,** 124, (2), 487-498.

31. Ackmann, T.; de Haart, L. G. J.; Lehnert, W.; Stolten, D., Modeling of mass and heat transport in planar substrate type SOFCs. *Journal of the Electrochemical Society* **2003,** 150, (6), A783-A789.

32. Campanari, S.; Iora, P., Definition and sensitivity analysis of a finite volume SOFC model for a tubular cell geometry. *Journal of Power Sources* **2004,** 132, (1-2), 113-126.

33. Aguiar, P.; Adjiman, C. S.; Brandon, N. P., Anode-supported intermediate temperature direct internal reforming solid oxide fuel cell. I: model-based steady-state performance. *Journal of Power Sources* **2004,** 138, (1-2), 120-136.

34. Aguiar, P.; Adjiman, C. S.; Brandon, N. P., Anode-supported intermediate-temperature direct internal reforming solid oxide fuel cell - II. Model-based dynamic performance and control. *Journal of Power Sources* **2005,** 147, (1-2), 136-147.

35. Li, P. W.; Suzuki, K., Numerical modeling and performance study of a tubular SOFC. *Journal of the Electrochemical Society* **2004,** 151, (4), A548-A557.

36. Qi, Y. T.; Huang, B.; Chuang, K. T., Dynamic modeling of solid oxide fuel cell: The effect of diffusion and inherent impedance. *Journal of Power Sources* **2005,** 150, 32-47.

37. Iora, P.; Aguiar, P.; Adjiman, C. S.; Brandon, N. P., Comparison of two IT DIR-SOFC models: Impact of variable thermodynamic, physical, and flow properties. Steady-state and dynamic analysis. *Chemical Engineering Science* **2005,** 60, (11), 2963-2975.

38. Mueller, F.; Brouwer, J.; Jabbari, F.; Samuelsen, S., Dynamic simulation of an integrated solid oxide fuel cell system including current-based fuel flow control. *Journal of Fuel Cell Science and Technology* **2006,** 3, (2), 144-154.

39. Suwanwarangkul, R.; Croiset, E.; Entchev, E.; Charojrochkul, S.; Pritzker, M. D.; Fowler, M. W.; Douglas, P. L.; Chewathanakup, S.; Mahaudom, H., Experimental and modeling study of solid oxide fuel cell operating with syngas fuel. *Journal of Power Sources* **2006,** 161, (1), 308-322.

40. Qi, Y. T.; Huang, B.; Luo, J. L., Dynamic modeling of a finite volume of solid oxide fuel cell: The effect of transport dynamics. *Chemical Engineering Science* **2006,** 61, (18), 6057-6076.

41. Jiang, W.; Fang, R. X.; Khan, J. A.; Dougal, R. A., Parameter setting and analysis of a dynamic tubular SOFC model. *Journal of Power Sources* **2006,** 162, (1), 316-326.

42. Cheddie, D. F.; Munroe, N. D. H., A dynamic 1D model of a solid oxide fuel cell for real time simulation. *Journal of Power Sources* **2007,** 171, (2), 634-643.

43. Jia, J. X.; Abudula, A.; Wei, L. M.; Jiang, R. Q.; Shen, S. Q., A mathematical model of a tubular solid oxide fuel cell with specified combustion zone. *Journal of Power Sources* **2007,** 171, (2), 696-705.

44. Bedogni, S.; Campanari, S.; Iora, P.; Montelatici, L.; Silva, P., Experimental analysis and modeling for a circular-planar type IT-SOFC. *Journal of Power Sources* **2007,** 171, (2), 617-625.

45. Li, J.; Cao, G. Y.; Zhu, X. J.; Tu, H. Y., Two-dimensional dynamic simulation of a direct internal reforming solid oxide fuel cell. *Journal of Power Sources* **2007,** 171, (2), 585-600.

46. Bao, C.; Cai, N. S., An approximate analytical solution of transport model in electrodes for anode-supported solid oxide fuel cells. *Aiche Journal* **2007,** 53, 2968-2979.

47. Ni, M.; Leung, D. Y. C.; Leung, M. K. H., Modeling of methane fed solid oxide fuel cells: Comparison between proton conducting electrolyte and oxygen ion conducting electrolyte (vol 183, pg 133, 2008). *Journal of Power Sources* **2009,** 194, (2), 1226-1227.

48. Qi, Y. T.; Huang, B.; Luo, J. L., 1-D dynamic modeling of SOFC with analytical solution for reacting gas-flow problem. *Aiche Journal* **2008,** 54, (6), 1537-1553.

49. Jeon, D. H., A comprehensive CFD model of anode-supported solid oxide fuel cells. *Electrochimica Acta* **2009,** 54, (10), 2727-2736.

50. Goldin, G. M.; Zhu, H.; Kee, R. J.; Bierschenk, D.; Barnett, S. A., Multidimensional flow, thermal, and chemical behavior in solid-oxide fuel cell button cells. *Journal of Power Sources* **2009,** 187, (1), 123-135.

51. Bhattacharyya, D.; Rengaswamy, R.; Finnerty, C., Dynamic modeling and validation studies of a tubular solid oxide fuel cell. *Chemical Engineering Science* **2009,** 64, (9), 2158-2172.

52. Colpan, C. O.; Dincer, I.; Hamdullahpur, F., A review on macro-level modeling of planar solid oxide fuel cells. *International Journal of Energy Research* **2008,** 32, (4), 336-355.

53. Lin, Y.; Beale, S. B., Performance predictions in solid oxide fuel cells. *Applied Mathematical Modelling* **2006,** 30, (11), 1485-1496.

54. Bove, R.; Ubertini, S., *Modeling solid oxide fuel cells: methods, procedures and techniques*. Springer Verlag: 2008.

55. Debenedetti, P.; Vayenas, C., Steady-state analysis of high temperature fuel cells. *Chemical Engineering Science* **1983,** 38, (11), 1817-1829.

56. Mangold, M.; Krasnyk, M.; Sundmacher, K., Theoretical investigation of steady state multiplicities in solid oxide fuel cells*. *Journal of Applied Electrochemistry* **2006,** 36, (3), 265-275.

57. Moxley, J. F.; Tulyani, S.; Benziger, J. B., Steady-state multiplicity in the autohumidification polymer electrolyte membrane fuel cell. *Chemical Engineering Science* **2003,** 58, (20), 4705-4708.

58. Benziger, J.; Chia, E.; Moxley, J. F.; Kevrekidis, I. G., The dynamic response of PEM fuel cells to changes in load. *Chemical Engineering Science* **2005,** 60, (6), 1743-1759.

59. Hogarth, W. H. J.; Benziger, J. B., Dynamics of autohumidifed PEM fuel cell operation. *Journal of the Electrochemical Society* **2006,** 153, (11), A2139-A2146.

60. Katsaounis, A.; Balomenou, S. P.; Tsiplakides, D.; Tsampas, M.; Vayenas, C. G., The role of potential-dependent electrolyte resistance in the performance, steady-state multiplicities and oscillations of PEM fuel cells: Experimental investigation and macroscopic modelling. *Electrochimica Acta* **2005,** 50, (25-26), 5132-5143.

61. Mench, M. M.; Wang, C., An in situ method for determination of current distribution in PEM fuel cells applied to a direct methanol fuel cell. *Journal of the Electrochemical Society* **2003,** 150, A79.

62. Katsaounis, A.; Tsampas, M.; Balomenou, S. P.; Tsiplakides, D.; Vayenas, C. G. In *Potential-dependent electrolyte resistance and steady-state multiplicities of PEM fuel cells*, 2006; Elsevier Science Bv: 2006; pp 2397-2401.

63. Chia, E. S. J.; Benziger, J. B.; Kevrekidis, I. G., Water balance and multiplicity in a polymer electrolyte membrane fuel cell. *Aiche Journal* **2004,** 50, (9), 2320-2324.

64. Chia, E. S. J.; Benziger, J. B.; Kevrekidis, L. G., STR-PEM fuel cell as a reactor building block. *Aiche Journal* **2006,** 52, (11), 3902-3910.

65. Liu, J.; Eikerling, M., Model of cathode catalyst layers for polymer electrolyte fuel cells: The role of porous structure and water accumulation. *Electrochimica Acta* **2008,** 53, (13), 4435-4446.

66. Nazarov, I.; Promislow, K., Ignition waves in a stirred PEM fuel cell. *Chemical Engineering Science* **2006,** 61, (10), 3198-3209.

67. Groetsch, M.; Hanke-Rauschenbach, R.; Mangold, M., Bifurcation analysis of a two-phase PEMFC model. *Journal of Fuel Cell Science and Technology* **2008,** 5, (2).

68. Uzunoglu, M.; Onar, O. C.; Alam, M. S., Dynamic behavior of PEM FCPPs under various load conditions and voltage stability analysis for stand-alone residential applications. *Journal of Power Sources* **2007,** 168, (1), 240-250.

69. Gemmen, R.; Johnson, C., Effect of load transients on SOFC operation--current reversal on loss of load. *Journal of Power Sources* **2005,** 144, (1), 152-164.

70. Benziger, J.; Chia, E.; Karnas, E.; Moxley, J.; Teuscher, C.; Kevrekidis, I. G., The stirred tank reactor polymer electrolyte membrane fuel cell. *Aiche Journal* **2004,** 50, (8), 1889-1900.

71. Zenith, F.; Skogestad, S., Control of the mass and energy dynamics of polybenzimidazole-membrane fuel cells. *Journal of Process Control* **2009,** 19, (3), 415-432.

72. Didierjean, S.; Lottin, O.; Maranzana, G.; Geneston, T., PEM fuel cell voltage transient response to a thermal perturbation. *Electrochimica Acta* **2008,** 53, (24), 7313-7320.

73. Bhattacharyya, D.; Rengaswamy, R., A Review of Solid Oxide Fuel Cell (SOFC) Dynamic Models. *Ind. Eng. Chem. Res.* **2009,** 48, (13), 10.

74. Grotsch, M.; Mangold, M., A two-phase PEMFC model for process control purposes. *Chemical Engineering Science* **2008,** 63, (2), 434-447.

75. Noren, D.; Hoffman, M., Clarifying the Butler-Volmer equation and related approximations for calculating activation losses in solid oxide fuel cell models. *Journal of Power Sources* **2005,** 152, 175-181.

76. Zhao, F.; Virkar, A., Dependence of polarization in anode-supported solid oxide fuel cells on various cell parameters. *Journal of Power Sources* **2005,** 141, (1), 79-95.

77. Mangold, M., personal communication. **2010**.

78. Perry, R.; Green, D.; Maloney, J., *Perry's chemical engineers' handbook*. McGraw-Hill New York: 1997.

79. Costamagna, P.; Honegger, K., Modeling of solid oxide heat exchanger integrated stacks and simulation at high fuel utilization. *Journal of the Electrochemical Society* **1998,** 145, 3995.

80. Chan, S.; Khor, K.; Xia, Z., A complete polarization model of a solid oxide fuel cell and its sensitivity to the change of cell component thickness. *Journal of Power Sources* **2001,** 93, (1-2), 130-140.

81. Welty, J.; Wicks, C.; Rorrer, G.; Wilson, R., *Fundamentals of momentum, heat, and mass transfer*. Wiley-India: 2009.

82. Kakac, S.; Pramuanjaroenkij, A.; Zhou, X. Y., A review of numerical modeling of solid oxide fuel cells. *Int. J. Hydrog. Energy* **2007,** 32, (7), 761-786.

83. Oldham, K.; Myland, J., *Fundamentals of electrochemical science*. Academic Press San Diego: 1993.

84. Shampine, L.; Reichelt, M.; Kierzenka, J., Solving index-I DAEs in MATLAB and Simulink. *SIAM review* **1999,** 41, (3), 538-552.

85. Kreuer, K., Proton Conducting Oxides. *Ann. Rev. Mater. Res.* **2003,** 33, (1), 333-359.

86. Brett, D.; Atkinson, A.; Brandon, N.; Skinner, S., Intermediate temperature solid oxide fuel cells. *Chem. Soc. Rev.* **2008,** 37, (8), 1568-1578.

87. Matsumoto, H.; Furuya, Y.; Okada, S.; Tanji, T.; Ishihara, T., Nanoionics phenomenon in proton-conducting oxide: Effect of dispersion of nanosize platinum particles on electrical conduction properties. *Science and Technology of Advanced Materials* **2007,** 8, (6), 531-535.

88. Bonanos, N., Transport properties and conduction mechanism in high-temperature protonic conductors. *Solid State Ion.* **1992,** 53, 967-974.

89. Haile, S.; Pintauro, P., Proton transport for fuel cells. In Royal Society of Chemistry: 2010; Vol. 20, pp 6211-6213.

90. Yang, L.; Zuo, C.; Wang, S.; Cheng, Z.; Liu, M., A Novel Composite Cathode for Low Temperature SOFCs Based on Oxide Proton Conductors. *Advanced Materials* **2008,** 20, (17), 3280-3283.

91. Iwahara, H., High temperature proton conducting oxides and their applications to solid electrolyte fuel cells and steam electrolyzer for hydrogen production. *Solid State Ion.* **1988,** 28, 573-578.

92. Suwanwarangkul, R.; Croiset, E.; Pritzker, M. D.; Fowler, M. W.; Douglas, P. L.; Entchev, E., Modelling of a cathode-supported tubular solid oxide fuel cell operating with biomass-derived synthesis gas. *Journal of Power Sources* **2007,** 166, (2), 386-399.

93. Incropera, F. P., *Fundamentals of heat and mass transfer*. 6th ed.; John Wiley: Hoboken, NJ, 2007; p xxv, 997 p.

94. Ni, M., Modeling of a planar solid oxide fuel cell based on proton conducting electrolyte. *International Journal of Energy Research* **2009**.

95. Arpino, F.; Carotenuto, A.; Massarotti, N.; Nithiarasu, P., A robust model and numerical approach for solving solid oxide fuel cell (SOFC) problems. *International Journal of Numerical Methods for Heat & Fluid Flow* **2008,** 18, (7/8), 811-834.

96. Patcharavorachot, Y.; Brandon, N. P.; Paengjuntuek, W.; Assabumrungrat, S.; Arpornwichanop, A., Analysis of planar solid oxide fuel cells based on proton-conducting electrolyte. *Solid State Ion.* **2010**.

97. Potter, A. R.; Baker, R. T., Impedance studies on PtSrCe0.95Yb0.05O3Pt under dried and humidified air, argon and hydrogen. *Solid State Ion.* **2006,** 177, (19-25), 1917-1924.

98. Wilke, C. R., Diffusional properties of multicomponent gases. *Chem. Eng. Prog* **1950,** 46, (2), 96-104.

99. Wang, C., *Modeling and Diagnostics of Polymer Electrolyte Fuel Cells*. Springer Verlag: 2010; Vol. 49.

100. Reid, R. C.; Prausnitz, J. M.; Poling, B. E., The properties of gases and liquids. **1987**.

101. Demin, A.; Tsiakaras, P.; Gorbova, E.; Hramova, S., A SOFC based on a co-ionic electrolyte. *Journal of Power Sources* **2004,** 131, (1-2), 231-236.

102. Jiang, K.; He, Z.; Meng, J.; Ren, Y.; Su, Q., Low temperature preparation and fuel cell properties of rare earth doped barium cerate solid electrolytes. *Science in China Series B: Chemistry* **1999,** 42, (3), 298-304.

103. Gorbova, E.; Maragou, V.; Medvedev, D.; Demin, A.; Tsiakaras, P., Investigation of the protonic conduction in Sm doped BaCeO3. *Journal of Power Sources* **2008,** 181, (2), 207-213.

104. Glöckner, R.; Islam, M.; Norby, T., Protons and other defects in BaCeO3: a computational study. *Solid State Ion.* **1999,** 122, (1-4), 145-156.

105. Iwahara, H.; Hibino, T.; Okada, T. In *proton and oxide-ion mixed conduction in perovskite-type oxide ceramics based on cerates*, Proceedings of the Second International Symposium on Ionic and Mixed Conducting Ceramics, Ramanarayanan, T. A.; Mogensen, M.; Yokokawa, H., Eds.

106. Iwahara, H.; Yajima, T.; Hibino, T.; Ushida, H., Performance of Solid Oxide Fuel Cell Using Proton and Oxide Ion Mixed Conductors Based on BaCeSmO. *Journal of the Electrochemical Society* **1993,** 140, 1687.

107. Riess, I., Current-voltage relation and charge distribution in mixed ionic electronic solid conductors. *Journal of Physics and Chemistry of Solids* **1986,** 47, (2), 129-138.

108. Ross Jr, P.; Benjamin, T., Thermal efficiency of solid electrolyte fuel cells with mixed conduction. *Journal of Power Sources* **1977,** 1, (3), 311-321.

109. Yuan, S.; Pal, U., Analytic Solution for Charge Transport and Chemical Potential Variation in Single Layer and Multilayer Devices of Different Mixed Conducting Oxides. *Journal of the Electrochemical Society* **1996,** 143, 3214.

110. Riess, I., Mixed ionic-electronic conductors--material properties and applications. *Solid State Ion.* **2003,** 157, (1-4), 1-17.

111. Huang, J.; Yuan, J.; Mao, Z.; Sunden, B., Analysis and Modeling of Novel Low-Temperature SOFC With a Co-Ionic Conducting Ceria-Based Composite Electrolyte. *Journal of Fuel Cell Science and Technology* **2010,** 7, (1), 011012-7.

112. Bard, A. J.; Faulkner, L. R., *Electrochemical methods : fundamentals and applications*. 2nd ed.; John Wiley: New York, 2001; p xxi, 833 p.

113. Iwahara, H.; Uchida, H.; Morimoto, K., High Temperature Solid Electrolyte Fuel Cells Using Perovskite Type Oxide Based on BaCeO. *Journal of the Electrochemical Society* **1990,** 137, 462.

114. Hirschfelder, J. O.; Curtiss, C. F.; Bird, R. B.; Laboratory, U. o. W. T. C., *Molecular theory of gases and liquids*. Wiley New York: 1954; Vol. 26.

115. Suzuki, M.; Shikazono, N.; Fukagata, K.; Kasagi, N., Numerical analysis of coupled transport and reaction phenomena in an anode-supported flat-tube solid oxide fuel cell. *Journal of Power Sources* **2008,** 180, (1), 29-40.

116. Bavarian, M.; soroush, M., Steady-State Multiplicity in a Solid Oxide Fuel Cell: Practical Considerations. *Chemical Engineering Science* **2011**.

117. O'Regan, B.; Gratzel, M., A low-cost, high-efficiency solar cell based on dye-sensitized colloidal TiO2 films. *Nature* **1991,** 353, (6346), 737-740.

118. Yella, A.; Lee, H.-W.; Tsao, H. N.; Yi, C.; Chandiran, A. K.; Nazeeruddin, M. K.; Diau, E. W.-G.; Yeh, C.-Y.; Zakeeruddin, S. M.; Grätzel, M., Porphyrin-Sensitized Solar Cells with Cobalt (II/III)–Based Redox Electrolyte Exceed 12 Percent Efficiency. *Science* **2011,** 334, (6056), 629-634.

119. Baxter, J. B., Commercialization of dye sensitized solar cells: Present status and future research needs to improve efficiency, stability, and manufacturing. *Journal of Vacuum Science & Technology A: Vacuum, Surfaces, and Films* **2012,** 30, (2), 020801-19.

120. Hardin, B. E.; Snaith, H. J.; McGehee, M. D., The renaissance of dye-sensitized solar cells. *Nature Photonics* **2012,** 6, (3), 162-169.

121. Snaith, H. J., Estimating the Maximum Attainable Efficiency in Dye-Sensitized Solar Cells. *Advanced Functional Materials* **2010,** 20, (1), 13-19.

122. Grätzel, M., Dye-sensitized solar cells. *Journal of Photochemistry and Photobiology C: Photochemistry Reviews* **2003,** 4, (2), 145-153.

123. Liu, H.; Avrutin, V.; Izyumskaya, N.; Özgür, Ü.; Morkoç, H., Transparent conducting oxides for electrode applications in light emitting and absorbing devices. *Superlattices and Microstructures* **2010,** 48, (5), 458-484.

124. Gratzel, M., Photoelectrochemical cells. *Nature* **2001,** 414, (6861), 338-344.

125. Barbé, C. J.; Arendse, F.; Comte, P.; Jirousek, M.; Lenzmann, F.; Shklover, V.; Grätzel, M., Nanocrystalline Titanium Oxide Electrodes for Photovoltaic Applications. *Journal of the American Ceramic Society* **1997,** 80, (12), 3157-3171.

126. Hagfeldt, A.; Boschloo, G.; Sun, L.; Kloo, L.; Pettersson, H., Dye-Sensitized Solar Cells. *Chemical Reviews* **2010,** 110, (11), 6595-6663.

127. Altobello, S.; Argazzi, R.; Caramori, S.; Contado, C.; Da Fré, S.; Rubino, P.; Choné, C.; Larramona, G.; Bignozzi, C. A., Sensitization of Nanocrystalline TiO2 with Black Absorbers Based on Os and Ru Polypyridine Complexes. *Journal of the American Chemical Society* **2005,** 127, (44), 15342-15343.

128. Asbury, J. B.; Anderson, N. A.; Hao, E.; Ai, X.; Lian, T., Parameters Affecting Electron Injection Dynamics from Ruthenium Dyes to Titanium Dioxide Nanocrystalline Thin Film†. *The Journal of Physical Chemistry B* **2003,** 107, (30), 7376-7386.

129. Koops, S. E.; O'Regan, B. C.; Barnes, P. R. F.; Durrant, J. R., Parameters Influencing the Efficiency of Electron Injection in Dye-Sensitized Solar Cells. *Journal of the American Chemical Society* **2009,** 131, (13), 4808-4818.

130. Ferber, J.; Luther, J., Computer simulations of light scattering and absorption in dye-sensitized solar cells. *Solar Energy Materials and Solar Cells* **1998,** 54, (1–4), 265-275.

131. Nelson, J.; Eppler, A. M.; Ballard, I. M., Photoconductivity and charge trapping in porous nanocrystalline titanium dioxide. *Journal of Photochemistry and Photobiology A: Chemistry* **2002,** 148, (1–3), 25-31.

132. van de Lagemaat, J.; Park, N. G.; Frank, A. J., Influence of Electrical Potential Distribution, Charge Transport, and Recombination on the Photopotential and Photocurrent Conversion Efficiency of Dye-Sensitized Nanocrystalline TiO2 Solar Cells: A Study by Electrical Impedance and Optical Modulation Techniques. *The Journal of Physical Chemistry B* **2000,** 104, (9), 2044-2052.

133. Hagfeldt, A.; Grätzel, M., Molecular Photovoltaics. *Accounts of Chemical Research* **2000,** 33, (5), 269-277.

134. Eppler, A. M.; Ballard, I. M.; Nelson, J., Charge transport in porous nanocrystalline titanium dioxide. *Physica E: Low-dimensional Systems and Nanostructures* **2002,** 14, (1–2), 197-202.

135. Bisquert, J., Chemical Diffusion Coefficient of Electrons in Nanostructured Semiconductor Electrodes and Dye-Sensitized Solar Cells. *The Journal of Physical Chemistry B* **2004,** 108, (7), 2323-2332.

136. Bisquert, J.; Zaban, A.; Greenshtein, M.; Mora-Seró, I., Determination of Rate Constants for Charge Transfer and the Distribution of Semiconductor and Electrolyte Electronic Energy Levels in Dye-Sensitized Solar Cells by Open-Circuit Photovoltage Decay Method. *Journal of the American Chemical Society* **2004,** 126, (41), 13550-13559.

137. Fisher, A. C.; Peter, L. M.; Ponomarev, E. A.; Walker, A. B.; Wijayantha, K. G. U., Intensity Dependence of the Back Reaction and Transport of Electrons in Dye-Sensitized Nanocrystalline TiO2 Solar Cells. *The Journal of Physical Chemistry B* **2000,** 104, (5), 949-958.

138. Salvador, P.; Hidalgo, M. G.; Zaban, A.; Bisquert, J., Illumination Intensity Dependence of the Photovoltage in Nanostructured TiO2 Dye-Sensitized Solar Cells. *The Journal of Physical Chemistry B* **2005,** 109, (33), 15915-15926.

139. Abayev, I.; Zaban, A.; Fabregat-Santiago, F.; Bisquert, J., Electronic conductivity in nanostructured TiO2 films permeated with electrolyte. *physica status solidi (a)* **2003,** 196, (1), R4-R6.

140. Hamann, T. W.; Jensen, R. A.; Martinson, A. B. F.; Van Ryswyk, H.; Hupp, J. T., Advancing beyond current generation dye-sensitized solar cells. *Energy & Environmental Science* **2008,** 1, (1), 66-78.

141. Green, A. N. M.; Chandler, R. E.; Haque, S. A.; Nelson, J.; Durrant, J. R., Transient Absorption Studies and Numerical Modeling of Iodine Photoreduction by Nanocrystalline TiO2 Films. *The Journal of Physical Chemistry B* **2004,** 109, (1), 142-150.

142. Ardo, S.; Meyer, G. J., Photodriven heterogeneous charge transfer with transition-metal compounds anchored to TiO2 semiconductor surfaces. *Chemical Society Reviews* **2009,** 38, (1), 115-164.

143. Wolfbauer, G.; Bond, A. M.; Eklund, J. C.; MacFarlane, D. R., A channel flow cell system specifically designed to test the efficiency of redox shuttles in dye sensitized solar cells. *Solar Energy Materials and Solar Cells* **2001,** 70, (1), 85-101.

144. Cameron, P. J.; Peter, L. M.; Zakeeruddin, S. M.; Grätzel, M., Electrochemical studies of the Co(III)/Co(II)(dbbip)2 redox couple as a mediator for dye-sensitized nanocrystalline solar cells. *Coordination Chemistry Reviews* **2004,** 248, (13–14), 1447-1453.

145. Wang, M.; Chamberland, N.; Breau, L.; Moser, J.-E.; Humphry-Baker, R.; Marsan, B.; Zakeeruddin, S. M.; Grätzel, M., An organic redox electrolyte to rival triiodide/iodide in dye-sensitized solar cells. *Nat Chem* **2010,** 2, (5), 385-389.

146. Barsoukov, E.; Macdonald, J. R., *Impedance spectroscopy : theory, experiment, and applications*. 2nd ed.; Wiley-Interscience: Hoboken, N.J., 2005; p xvii, 595 p.

147. Grätzel, M., Solar energy conversion by dye-sensitized photovoltaic cells. *Inorganic Chemistry* **2005,** 44, (20), 6841-6851.

148. Halme, J.; Vahermaa, P.; Miettunen, K.; Lund, P., Device Physics of Dye Solar Cells. *Advanced Materials* **2010,** 22, (35), E210-E234.

149. Kalyanasundaram, K., *Dye-sensitized solar cells*. CRC Press: Boca Raton, Fla., 2010; p xviii, 604 p.

150. *Electrochemical Impedance Spectroscopy Primer*; Gamry.

151. Archer, M. D.; Nozik, A. J., *Nanostructured and photoelectrochemical systems for solar photon conversion*. Imperial College Press: London, 2008; p xx, 760 p.

152. Rhee, S. W.; Kwon, W., Key technological elements in dye-sensitized solar cells (DSC). *Korean Journal of Chemical Engineering* **2011**, 1-14.

153. Bisquert, J., Dilemmas of Dye-Sensitized Solar Cells. *ChemPhysChem* **2011,** 12, (9), 1633-1636.

154. Miyasaka, T., Toward Printable Sensitized Mesoscopic Solar Cells: Light-Harvesting Management with Thin TiO2 Films. *The Journal of Physical Chemistry Letters* **2011,** 2, (3), 262-269.

155. Smith, J.; Reiter, L., An in-depth review of photovoltaic system performance models. *American Society of Mechanical Engineers* **1984,** 1.

156. Liu, S.; Dougal, R. A., Dynamic multiphysics model for solar array. *Energy Conversion, IEEE Transactions on* **2002,** 17, (2), 285-294.

157. Alam, M. S.; Alouani, A. T., Dynamic modeling of photovoltaic module for real-time maximum power tracking. *Journal of Renewable and Sustainable Energy* **2010,** 2, 043102.

158. Grätzel, M., Recent advances in sensitized mesoscopic solar cells. *Accounts of chemical research* **2009,** 42, (11), 1788-1798.

159. Hwang, I.; McNeill, C. R.; Greenham, N. C., Drift-diffusion modeling of photocurrent transients in bulk heterojunction solar cells. *Journal of Applied Physics* **2009,** 106, (9), 094506-10.

160. Anta, J. A.; Casanueva, F.; Oskam, G., A numerical model for charge transport and recombination in dye-sensitized solar cells. *The Journal of Physical Chemistry B* **2006,** 110, (11), 5372-5378.

161. Ferber, J.; Luther, J., Modeling of photovoltage and photocurrent in dye-sensitized titanium dioxide solar cells. *The Journal of Physical Chemistry B* **2001,** 105, (21), 4895-4903.

162. Ferber, J.; Stangl, R.; Luther, J., An electrical model of the dye-sensitized solar cell. *Solar Energy Materials and Solar Cells* **1998,** 53, (1-2), 29-54.

163. Kern, R.; Sastrawan, R.; Ferber, J.; Stangl, R.; Luther, J., Modeling and interpretation of electrical impedance spectra of dye solar cells operated under open-circuit conditions. *Electrochimica Acta* **2002,** 47, (26), 4213-4225.

164. Brunton, S. L.; Rowley, C. W.; Kulkarni, S. R.; Clarkson, C. In *Maximum power point tracking for photovoltaic optimization using extremum seeking*, 2009; IEEE: 2009; pp 000013-000016.

165. Pelanchon, F.; Mialhe, P., Optimization of solar cell performance. *Solid-state electronics* **1990,** 33, (1), 47-51.

166. Girardini, K.; Jacobsen, S., Optimization and numerical models of silicon solar cells. *Solid-state electronics* **1991,** 34, (1), 69-77.

167. Huang, J.; Moroz, V. In *Mono-Crystalline Silicon Solar Cell Optimization and Modeling*, 2011; ECS: 2011.

168. Soedergren, S.; Hagfeldt, A.; Olsson, J.; Lindquist, S.-E., Theoretical Models for the Action Spectrum and the Current-Voltage Characteristics of Microporous Semiconductor Films in Photoelectrochemical Cells. *The Journal of Physical Chemistry* **1994,** 98, (21), 5552-5556.

169. Oda, T.; Tanaka, S.; Hayase, S., Differences in characteristics of dye-sensitized solar cells containing acetonitrile and ionic liquid-based electrolytes studied using a novel model. *Solar Energy Materials and Solar Cells* **2006,** 90, (16), 2696-2709.

170. Topič, M.; Čampa, A.; Filipič, M.; Berginc, M.; Krašovec, U. O.; Smole, F., Optical and electrical modelling and characterization of dye-sensitized solar cells. *Current Applied Physics* **2010,** 10, (3, Supplement), S425-S430.

171. Hagfeldt, A.; Graetzel, M., Light-Induced Redox Reactions in Nanocrystalline Systems. *Chemical Reviews* **1995,** 95, (1), 49-68.

172. Barnes, P. R. F.; Anderson, A. Y.; Durrant, J. R.; O'Regan, B. C., Simulation and measurement of complete dye sensitised solar cells: including the influence of trapping, electrolyte, oxidised dyes and light intensity on steady state and transient device behaviour. *Physical Chemistry Chemical Physics* **2011,** 13, (13), 5798-5816.

173. Andrade, L.; Sousa, J.; Aguilar Ribeiro, H.; Mendes, A., Phenomenological modeling of dye-sensitized solar cells under transient conditions. *Solar Energy* **2011,** 85, (5), 781-793.

174. Smestad, G. P., *Optoelectronics of solar cells*. SPIE Press: Bellingham, Wash., 2002; p xv, 99 p.

175. J. Frank, A.; Kopidakis, N.; Lagemaat, J. v. d., Electrons in nanostructured TiO2 solar cells: transport, recombination and photovoltaic properties. *Coordination Chemistry Reviews* **2004,** 248, (13–14), 1165-1179.

176. Peter, L. M., Dye-sensitized nanocrystalline solar cells. *Physical Chemistry Chemical Physics* **2007,** 9, (21), 2630-2642.

177. Nazeeruddin, M. K.; De Angelis, F.; Fantacci, S.; Selloni, A.; Viscardi, G.; Liska, P.; Ito, S.; Takeru, B.; Grätzel, M., Combined experimental and DFT-TDDFT computational study of photoelectrochemical cell ruthenium sensitizers. *Journal of the American Chemical Society* **2005,** 127, (48), 16835-16847.

178. Nazeeruddin, M. K.; Kay, A.; Rodicio, I.; Humphry-Baker, R.; Mueller, E.; Liska, P.; Vlachopoulos, N.; Graetzel, M., Conversion of light to electricity by cis-X2bis(2,2'-bipyridyl-4,4'-dicarboxylate)ruthenium(II) charge-transfer sensitizers (X = Cl-, Br-, I-, CN-, and SCN-) on nanocrystalline titanium dioxide electrodes. *Journal of the American Chemical Society* **1993,** 115, (14), 6382-6390.

179. Nejati, S.; Lau, K. K. S., Pore filling of nanostructured electrodes in dye sensitized solar cells by initiated chemical vapor deposition. *Nano Letters* **2011**.

180. Huang, S.; Schlichthörl, G.; Nozik, A.; Grätzel, M.; Frank, A., Charge recombination in dye-sensitized nanocrystalline TiO2 solar cells. *The Journal of Physical Chemistry B* **1997,** 101, (14), 2576-2582.

181. Schlichthörl, G.; Huang, S.; Sprague, J.; Frank, A., Band edge movement and recombination kinetics in dye-sensitized nanocrystalline TiO2 solar cells: a study by intensity modulated photovoltage spectroscopy. *The Journal of Physical Chemistry B* **1997,** 101, (41), 8141-8155.

182. Lyon, L. A.; Hupp, J. T., Energetics of the Nanocrystalline Titanium Dioxide/Aqueous Solution Interface: Approximate Conduction Band Edge Variations between H0=-10 and H-=+ 26. *The Journal of Physical Chemistry B* **1999,** 103, (22), 4623-4628.

VITA

Name: Mona Bavarian

Education:

- Ph.D., Chemical Engineering, Drexel University, 2012.
- B.S., Chemical Engineering, Sharif University of Technology, 2006.

Selected Publications:

- Bavarian, M.; Soroush, M., Mathematical Modeling and Steady-State Analysis of a Proton-Conducting Solid Oxide Fuel Cell. *Journal of Process Control* **2012**.
- Bavarian, M.; Soroush, M., Steady-state multiplicity in a solid oxide fuel cell: Practical considerations. *Chemical Engineering Science* **2012,** *67* (1), 2-14.
- Bavarian, M.; Soroush, M.; Kevrekidis, I. G.; Benziger, J. B., Mathematical Modeling, Steady-State and Dynamic Behavior, and Control of Fuel Cells: A Review†. *Ind. Eng. Chem. Res.* **2010,** *49* (17), 7922-7950.
- Bavarian, M., Soroush, M., Steady-State Multiplicity in a Solid Oxide Fuel Cell: Impact of Practical Considerations, *Proceedings of American Control Conference, San Francisco, CA (2010).*